Graduate School ETD Form 9
(Revised 12/07)

PURDUE UNIVERSITY
GRADUATE SCHOOL
Thesis/Dissertation Acceptance

This is to certify that the thesis/dissertation prepared

By Kevin Lorenz

Entitled
Registration and Segmentation Based Analysis of Microscopy Images

For the degree of Doctor of Philosophy

Is approved by the final examining committee:

EDWARD J. DELP, Co-Chair
Chair

THOMAS M. TALAVAGE

PAUL SALAMA, Co-Chair

MARY L. COMER

KENNETH W. DUNN

To the best of my knowledge and as understood by the student in the *Research Integrity and Copyright Disclaimer (Graduate School Form 20)*, this thesis/dissertation adheres to the provisions of Purdue University's "Policy on Integrity in Research" and the use of copyrighted material.

Approved by Major Professor(s): EDWARD J. DELP, Co-Chair

Approved by: M. R. Melloch 07/24/2012
Head of the Graduate Program Date

Graduate School Form 20
(Revised 9/10)

PURDUE UNIVERSITY
GRADUATE SCHOOL

Research Integrity and Copyright Disclaimer

Title of Thesis/Dissertation:
Registration and Segmentation Based Analysis of Microscopy Images

For the degree of Doctor of Philosophy

I certify that in the preparation of this thesis, I have observed the provisions of *Purdue University Executive Memorandum No. C-22,* September 6, 1991, *Policy on Integrity in Research.**

Further, I certify that this work is free of plagiarism and all materials appearing in this thesis/dissertation have been properly quoted and attributed.

I certify that all copyrighted material incorporated into this thesis/dissertation is in compliance with the United States' copyright law and that I have received written permission from the copyright owners for my use of their work, which is beyond the scope of the law. I agree to indemnify and save harmless Purdue University from any and all claims that may be asserted or that may arise from any copyright violation.

Kevin Lorenz
Printed Name and Signature of Candidate

06-22-2012
Date (month/day/year)

*Located at http://www.purdue.edu/policies/pages/teach_res_outreach/c_22.html

REGISTRATION AND SEGMENTATION BASED ANALYSIS OF MICROSCOPY IMAGES

A Dissertation

Submitted to the Faculty

of

Purdue University

by

Kevin S. Lorenz

In Partial Fulfillment of the

Requirements for the Degree

of

Doctor of Philosophy

August 2012

Purdue University

West Lafayette, Indiana

To my family and friends, who have given their neverending support.

ACKNOWLEDGMENTS

Upon the completion of this dissertation, I acknowledge that my gratitude towards those who have inspired, encouraged, and motivated me through my years at Purdue cannot be expressed in mere words. Yet, this is a feeble attempt to accomplish this.

I wish to thank my major adviser, Prof. Edward J. Delp, for taking me under his guidance. He has given me the opportunity and privilege of becoming a member of the Video and Image Processing Laboratory (VIPER). I am grateful for his support during difficult times, his candid supervisory style, and his confidence in me. Moreover, I have enjoyed many nonacademic-related conversations with him, from which I appreciate his broad and diverse knowledge of a wide variety of topics.

I express my gratitude toward my co-adviser, Prof. Paul Salama. I appreciate his active role and engagement with all of the small details of my research project. He has contributed countless hours in the form of impromptu and scheduled weekly meetings where we discussed results, formulated steps to take for improvement, and performed numerous paper revisions. His support and high level of involvement has been invaluable.

I wish to thank Prof. Kenneth W. Dunn for his time and effort spent discussing the interdisciplinary aspect of my research project. His contributions from a medical and biological perspective are highly appreciated and made this work truly valuable. I also wish to thank my other committee members, Prof. Mary L. Comer and Prof. Thomas M. Talavage, for their advice, guidance, encouragement, and criticism. I have enjoyed my learning experience with them, both inside and outside of classroom discussions on various topics. I am grateful for their patience and insightful suggestions.

I have had the distinct pleasure of being surrounded by my wonderful current and former colleagues, who have all given their academic and social support: Dr. Golnaz Abdollahian, Ziad Ahmad, Dr. Marc Bosch Ruiz, Dr. Ying Chen Lou, Neeraj

Gadgil, Andrew W. Haddad, Ye He, Dr. Nitin Khanna, Deen King-Smith, Dr. Aravind K. Mikkilineni, Dr. Ka Ki Ng, Albert Parra Pozo, Dr. Satyam Srivastava, Chang Xu, Dr. Meilin Yang, Bin Zhao, and Dr. Fengqing Zhu. Special thanks are due to Aravind for being a partner in solving lab IT troubles. I appreciate the support and friendship of all these individuals. Without their presence, I would not have had such a friendly and supportive work environment.

I wish to thank the U.S. Department of Education for financially supporting beginning graduate students in science, technology, engineering, and mathematics. Through these actions, they relieved my beginning years at Purdue from financial burden. I also wish to thank the National Institutes of Health for their sponsorship of the research in this dissertation, and for funding my ending years at Purdue. Their generous support has made this dissertation possible.

I also wish to thank all my professors at Michigan State University in East Lansing, Michigan. They have had a great impact in inspiring and encouraging me to continue and expand my studies at the graduate level.

I thank all my friends, decades-long and recent, for their belief in me. They gave me the strength and motivation to overcome many difficult times. Finally, I wish to thank the support and encouragement that I have received from my family. Without their unconditional love, affection, support, and trust, I would never have been able to follow my ambitions and achieve my goals as a student hundreds of miles from home. I am grateful to my family for their unwavering and perpetual support of my academic and career aspirations.

This work was supported by a George M. O'Brien Award from the National Institutes of Health NIH/NIDDK P50 DK 61594.

TABLE OF CONTENTS

Page

Page

LIST OF TABLES

LIST OF FIGURES

ABSTRACT

Lorenz, Kevin S. Ph.D., Purdue University, August 2012. Registration and Segmentation Based Analysis of Microscopy Images. Major Professors: Edward J. Delp and Paul Salama.

Optical microscopy exhibits many challenges for digital image analysis. In general, microscopy volumes are inherently anisotropic, suffer from decreasing contrast with tissue depth, lack object edge detail, and characteristically have low signal levels. Image analysis is motivated by the desire to quantify biological characteristics such as cell count and tissue volume. This thesis describes methods for an integrated approach to segmentation and registration of intravital microscopy image sets. Image data are acquired using one of two distinct techniques. One data set type consists of a series of images corresponding to focal planes looking deeper in the tissue (three dimensional data), and a second type consists of a series of images corresponding to a sequence of time instances imaging a single focal plane (time-series data). Analysis is performed via a combination of segmentation and registration techniques, but is complicated by factors such as live specimen motion during image acquisition. In particular, we describe a method that utilizes image enhancement, spatial filtering, rigid and non-rigid registration, and temporal filtering. Experimental results indicate our methods are promising based on the analysis of several sets of liver, kidney, lung, and salivary gland images. By lacking ground truth data to evaluate accuracy of results, analysis consistency is evaluated using flipped image volumes and reverse image acquisition. Registration validation is performed using motion vector analysis, a non-traditional application of a technique borrowed from motion estimation.

1. INTRODUCTION

1.1 Background in Optical Microscopy in Biological Research

Optical microscopy has become one of the most powerful techniques in biomedical research, particularly when combined with digital image analysis. Since an optical microscope uses visible light and a system of lenses to magnify images, as opposed to electrons and electromagnets present in electron microscopes, the size of the smallest samples an optical microscope is able to resolve is directly proportional to the wavelength of visible light. Among all types of optical microscopes, one variety is a fluorescence microscope, which uses fluorescence instead of reflection and absorption as a source of image contrast. With fluorescence microscopy, a specimen is first injected with fluorophores (fluorescent molecules) which then attach to or tag proteins or other molecules within the specimen. The specimen is then illuminated with light of a specific wavelength, which is absorbed by and excites the fluorophores. As a result, the fluorophores emit light, which usually has a longer wavelength (lower energy) than the absorbed light. Fluorescence occurs when a single excitation photon is absorbed by a fluorophore, causing a transition of the molecule into a more energetic and excited state. The molecule then relaxes back to its natural ground state by emitting a single photon of a less energetic, longer wavelength than the excitation wavelength [1].

A fluorescence microscope contains a filter or a series of filters that accomplish two primary tasks. One task is to ensure the illumination light is at the correct wavelength and contains no other wavelengths. A second task is to ensure that only the fluoresced light and none of the illumination/excitation light reaches the microscope detector. For both of these tasks to be accomplished, the wavelength of illumination light, the

choice of fluorescence injected into the specimen, and the light filters must all be appropriately paired and matched.

Illumination light with short wavelengths (consisting of high energy) is often necessary to excite fluorophores, which may damage living tissue. This is overcome through the use of multiphoton fluorescence microscopy. With a multiphoton microscope, two or more photons from light with a long wavelength arrive simultaneously at a fluorophore. The fluorophore absorbs this combined energy, resulting in the same effect as traditional fluorescence microscopy. This combined energy from multiple low-energy photons excites an electron into a higher energy state that emits a higher energy photon as it decays. The distinct difference of multiphoton microscopy is that with the combination of the energy from multiple photons simultaneously, the illumination/excitation wavelength is longer (lower energy) than the emission wavelength. The energy of a photon is inversely proportional to its wavelength. Therefore, if two-photon excitation is used, the two photons should be about twice the wavelength required for single-photon excitation. For example, a fluorophore that normally becomes excited by one photon at 350 nm can also be excited by two photons at 700 nm if they reach the fluorophore simultaneously (within about $10^{-18} - 10^{-16}$ seconds) [2]. Two photons of approximately equal energy interact with a molecule, producing an excitation equivalent to the absorption of a single photon possessing twice the energy. With the use of lower energy (longer wavelength) light, multiphoton microscopes will cause much less damage to living tissue which enables the imaging of live cells. As a result, living tissue and cells may be observed for longer durations and with less recovery time while experiencing fewer toxic effects. Furthermore, with multiphoton microscopy, the fluorescence intensity has a squared dependence on the laser light intensity, rather than the linear dependence of conventional fluorescence microscopy. For example, doubling the excitation intensity produces four times the fluorescence [3].

The titanium-sapphire laser typically used to excite two-photon fluorescence emits infrared light from approximately 700 to 1000 nm, while typical fluorophores have excitation spectra at shorter wavelengths. The probability of the near-simultaneous

absorption of two photons is extremely low. Therefore, to obtain a significant number of two-photon absorption events where both photons interact with the fluorophore simultaneously, the photon density must be approximately one million times greater than what is required to generate the same number of one-photon absorptions [2]. This requires a much higher rate of low-energy excitation photons (both spatially and temporally) than with single-photon microscopy. As a result, extremely high-powered lasers are required to generate a sufficient amount of two-photon-excited fluorescence. This is accomplished by using pulsed lasers, where the peak power during the pulse is high enough to generate significant two-photon excitation, but the average laser power is fairly low so as not to damage the specimen. The pulse duty cycle (the duration of the pulse divided by the time between pulses) is approximately 10^{-5}, which limits the average power to less than 10 mW. The pulse durations are typically from 100 femtoseconds to 1 picosecond ($10^{-13} - 10^{-12}$ s). However, from the perspective of the fluorophore, where the absorption event occurs within 10^{-18} s, the laser pulses appear to be quite long in duration.

When a fluorophore absorbs two low-energy (infrared) photons simultaneously, it will absorb enough energy to be raised into the excited state. The fluorophore will then emit a single photon with a wavelength that depends on the type of fluorophore used, which is typically in the visible spectrum. The only place at which the photons are crowded enough to generate a significant amount of two-photon excitation is at the focal point of the laser. The primary benefit of this arrangement is that light emissions are not required to be directly imaged. With localized excitation, all of the fluorescence emanating from the sample may be collected and mapped to this single particular laser focal point in three dimensional space. A two or three dimensional image is then constructed by scanning the laser focal point through the sample, collecting all of the light from each focal point, and mapping the emitted light to the corresponding positions in the image space. Other types of microscopy have to either image the sample (which is blurry due to all of the out-of-focus excitation and scattered emissions) or use confocal microscopy (which rejects all of the

scattered emissions). With multiphoton microscopy, no excitation occurs outside the focal plane. Therefore, there is no background fluorescence to degrade image contrast. Further benefits of this arrangement include the reduced risk of photobleaching (destruction of the fluorophore) or photodamage (damage to the specimen) outside of the focal region [4]. In some cases, a specimen may be imaged continuously for multiple hours without any noticeable damage [5]. However, the risk of photobleaching and photodamage within the focal region is not entirely eliminated. Multiphoton microscopy studies should still take precautions to optimize and reduce the excitation intensity by understanding the effects and limits of the specific biological system under investigation, as well as by reviewing procedural considerations such as blanking the laser when image data are not being collected.

As an additional benefit of multiphoton microscopy, given that there is no out-of-focus absorption, more of the excitation light penetrates through the specimen to the focal plane, leading to greatly increased sample penetration compared to other forms of microscopy [6]. However, the maximum imaging depth depends on the properties of the tissue sample, the efficiency of the fluorophore, and the properties of the microscope optics. Furthermore, the simplified optical configuration of multiphoton microscopes coupled with the ability to excite multiple types of fluorophores with a single excitation wavelength enables scientists to construct color (multi-channel) images just as easily as grayscale (single-channel) images. As the name implies, single-channel data sets contain only one channel of data acquired from a single probe injected into the specimen. On the other hand, multi-channel data sets contain multiple channels of data, corresponding to the fluorescence of multiple probes introduced into the specimen, collected simultaneously by many photomultiplier detectors.

1.2 Current Challenges

Quantitative microscopy requires the ability to quantify signals in defined structures, necessitating the use of image segmentation. Image segmentation refers to the

process of partitioning an image into two or more regions. More precisely, image segmentation is the process of assigning a label to every pixel in an image such that pixels with the same label have similar visual characteristics. Visual characteristics used with image segmentation may include color, intensity, texture, or some other computed value. All of the pixels in a particular region are similar with respect to one or multiple visual characteristics, while pixels belonging to adjacent regions are significantly different with respect to the same characteristics.

Image segmentation is typically used to locate objects and boundaries in images, usually defined by edges. Its goal is to produce a new image representative of the original image that is easier to analyze and understand. Image segmentation has a variety of applications to solve a wide range of problems. For example, medical imaging uses image segmentation to better understand characteristics of biological tissues. Tasks such as locating tumors, computing tissue volumes, and determining anatomical structure have all previously taken advantage of image segmentation techniques.

Automated methods for quantitative microscopy are still highly underdeveloped. This primarily reflects the lack of image analysis tools suited to the unique properties of microscopic image sets. The image data sets presented in this work contain many unique characteristics that make analysis challenging. Microscopy volumes are inherently anisotropic, with aberrations and distortions that vary in different axes. Additionally, with three dimensional data sets, image contrast decreases with depth in biological tissues. This contrast decrease aggravates a general problem of fluorescence, which characteristically has low signal levels [7], consisting of as little as a single photon.

Images with severely low contrast are typically difficult to segment. The intensity and contrast of all fluorescence microscopy images are limited by the number of photons that can be stimulated from the sample. Methods to increase contrast during image acquisition and before offline image analysis have drawbacks and caveats. For example, the number of captured photons can be increased by extending integration

time. However, this limits temporal resolution. Secondly, image contrast can be improved by limiting magnification so that emissions from a larger area are captured by the detector element. This comes at the expense of limited spatial resolution. Thirdly, increasing illumination levels improves image contrast, but has limited benefits and incurs sample damage and fluorophore photobleaching. Lastly, increasing detector gain improves image contrast, which consequently also increases electronic sources of noise.

Adding to the difficulty of segmentation, objects desired to be segmented from microscopy image sets typically have poorly defined edges. Object boundaries are not composed of rigid continuous edges; instead noise, low image resolution, and the dynamic nature of biological tissues contribute to creating sparse edges along with irregular and inconsistent patterns within objects as tissue is not homogeneous. Additionally, image resolution is considered poor compared to non-biological applications of image processing. During image acquisition, spatial resolution can be increased at the expense of image capture speed (temporal resolution). However, high image capture rates are necessary to image dynamic biological structures. Therefore, a compromise must be reached in the trade-off between spatial and temporal resolution. All of these characteristics contribute in making segmentation and rendering results very sensitive to small changes in parameters. This causes inconsistent and unpredictable results, leading to the failure of typical image analysis methods [8].

As previously described, both single- and multi-channel data may be acquired using multiphoton microscopy. When viewing multi-channel data sets, the colors displayed are not due to the biological structures truly being the color shown, but are an approximation. More precisely, each channel is captured via band-pass filters that aggregate a range of wavelengths into one of the three image color channels. For example, emissions from 500–550 nm may be captured via a band-pass filter and depicted as the green channel in the composed image. Unfortunately, channel isolation is imperfect and crosstalk often occurs among the channels [9]. For instance, biological structures that appear in one particular channel may appear in the re-

maining two channels with reduced intensity. This channel crosstalk effect reflects the fact that the emission spectra of all fluorophores extend into a long tail across long wavelengths (in the red area of the spectrum). Each type of fluorophore has an associated wavelength emission profile for the fluorescence it gives off. However, the fluorescence from multiple fluorophores may have overlapping wavelengths such that the band-pass filters are unable to isolate the fluorescence perfectly. More specifically, a fraction of the emission of a "blue" fluorescing fluorophore will be collected in the green channel, and a fraction of the emission of a "green" fluorescing fluorophore will be collected in the red channel. This effect is exacerbated when a particular channel becomes saturated. For example, if the fluorescence in the green channel reaches its saturation limit, the red channel will appear to have an increased crosstalk effect.

As previously mentioned, multiphoton microscopy more easily allows the imaging of living animals. This exciting form of microscopy is known as intravital microscopy. Intravital microscopy is unique because it is able to image dynamic processes such as intracellular transport, cell migration and motility, and other cellular interactions and metabolic activities, which all advances knowledge about clinical diagnosis and treatments [5]. Combined with multiphoton microscopy, intravital microscopy is a technique that facilitates imaging hundreds of microns into biological tissues at sub-cellular resolution [10].

Intravital multiphoton microscopy is used to collect not just single images, but a series of images, both in time-series and in three dimensions. With the imaging of living specimens, motion artifacts are introduced into the scene as a result of factors such as respiration and heartbeat. This introduces distortions such as translations and warping into the images, degrading image quality. Amounts of sample motion that are acceptable for lower-resolution techniques are intolerable in multiphoton microscopy, whose sub-micron resolution is completely ruined with even the slightest motion in the tissue. These factors further contribute to the difficulty of automated quantification of intravital microscopy images.

To acquire an image or volume, a laser is focused and raster scanned across the sample. However, to gather enough detail in a three dimensional volume, data collection may often require 10 or more minutes. This lengthy data acquisition duration, coupled with the raster scanning property of the microscope to create the image data, gives rise to the presence of motion artifacts. Since the respiratory rate of a mouse is approximately 160 breaths per minute and its heart rate is approximately 600 beats per minute, intrascene distortions will inevitably be experienced with a frame rate of only approximately 1 frame per second. This relatively slow frame rate, combined with the secondary effect of raster scanning, all but guarantees the presence of motion artifacts.

Correcting these distortions will require a combination of rigid and non-rigid image registration techniques. Image registration involves matching two or more images acquired at different times, from different sensors with different resolutions or dimensions, or from different viewpoints/perspectives [11]. Image registration refers to the process of transforming and aligning all the images in the data set into a shared coordinate system, a condition aiding in future image analysis. The process is often described as finding an explicit function that performs a backward mapping of a target image onto a source image [12]. This is necessary so that all images in the data set can be compared against a common set of measurements or specifications.

Motion artifacts occur in the imaging of cultured cells, but manifest themselves only as orthogonal translations, which are easily corrected with rigid registration techniques. Intravital microscopy has the additional issue of intrascene motion, requiring the use of non-rigid registration. For stable tissues such as the brain, motion artifacts may not be an issue in imaging. For less stable tissue, motion artifacts can be minimized to some extent by immobilizing the organ. In many cases, these approaches are sufficiently effective to facilitate high-resolution multiphoton fluorescence microscopy of the kidney [9, 13, 14], the liver [15, 16], and even the lung [17]. However, these methods are by no means foolproof, so that imaging studies are frequently plagued with residual motion artifacts.

1.3 Current Methods for Analysis of Microscopy Images

Although traditionally used as an observational tool, intravital microscopy has developed into a powerful new method in biomedical research. It has led to more robust and comprehensive quantitative methods with the development of innovative digital imaging and image analysis techniques. For example, various light microscopy imaging techniques have been developed in nephrology. A review of many of these techniques is presented in [18] where their advantages, imaging properties, and limitations are discussed. When combined with digital image analysis, intravital microscopy is capable of quantifying physiology and structure at a cellular and subcellular level. For example, intravital multiphoton microscopy has been used to obtain unique insights into the *in vivo* cell biology of the brain [19,20], the immune system [21–23], and cancer [24–26]. Intravital microscopy also has a long history of productive application to visceral organs, such as the liver [27, 28] and the kidney [29, 30].

Physical and optical properties of fluorescence microscopes distort image data to varying degrees. The majority of the distortion can be modeled in the point-spread function (PSF) of the microscope. This PSF is the three dimensional convolution of a point source object by the microscope objective. The PSF is defined by how a microscope system images a point source and how the lens spreads the signal along all three axes. The PSF in a well-corrected system typically resembles an hourglass shape elongated along the z-axis. A non-ideal PSF results in decreased image contrast, edge detail, and signal-to-noise ratio. Authors in [31] describe multiple deconvolution methods for three dimensional fluorescence microscopy images to reverse the effects of the PSF and restore the original image data. With knowledge of the PSF, deconvolution may be accomplished using information from neighboring or all focal planes in the volume. However, this task is often ill-posed as little or no information about the PSF or the imaging system is available. So-called blind deconvolution techniques estimate the PSF during the deconvolution process, usually through an iterative pro-

cedure. However, others [32] have pointed out that deconvolution is not necessarily helpful in improving image quality, depending on the goals of the study.

Following image pre-processing techniques such as deconvolution, several methods have been proposed in attempts to perform automated segmentation of cellular structures in microscopy images. Methods proposed in [33] introduce how to extract useful feature information from vast amounts of microscopic image data. Alternative methods take into account and rely on *a priori* information, such as the shape of the objects to segment. For example, methods proposed in [34] segment cell nuclei in confocal microscopy images with a circular structure based on *a priori* knowledge. Along with *a priori* shape information, the authors combine techniques such as dynamic programming and polar coordinate representation of objects. Methods in [7] use active contours and *a priori* information to segment and track cells by constraining cell volume to remain approximately constant (by minimizing a piece-wise constant energy function that includes terms that penalize the variance of the intensity inside and outside the boundary as well as a regularization term that penalizes total boundary length). Similarly, authors of [35] borrow the concept of active contours, but migrate from the notion of a contour to one of a mask to segment clusters of nuclei in microscopy images. In [36] and [37], a combination of thresholding and watershed segmentation is used to segment nuclei in time-lapse fluorescence microscopy images. This was followed by a scheme to refine the segmentation to merge nuclei that were perhaps misidentified as separate nuclei, and to also split nuclei that were perhaps misidentified as a single nucleus. After segmentation, cells were classified either using a K-nearest-neighbor (KNN) classifier or a continuous Markov model for cell phase identification. Thus, this method utilized a wide breadth of techniques for segmentation and classification.

The work in [8] describes chromosome feature extraction by using a Kohonen self-organizing feature map and a neural network. This was motivated by the desire to represent confocal microscopy images of chromosomes using a set of robust features, and to classify these images based on similar features. Methods proposed in [38] seg-

ment confocal microscopy images of neurons and dendrites by identifying edges via a multi-scale wavelet edge detection technique [39]. The method aims to overcome challenges such as large variability in object size, large variations in image contrast, and unequal fluorescence. The work in [40] uses a Bayesian framework and Gaussian Markov random fields to segment confocal microscopy images and identify nuclei in cancerous tissues. Their goal is to quantify nuclei size and nuclei-to-cytoplasm ratios for cancer studies. Methods proposed in [41] attempt to perform completely automated segmentation of confocal microscopy images by using fluorescence distribution patterns and statistics on pixel intensity. The authors point out that this method has the advantage of not requiring prior knowledge about the shape, size, or quantity of objects desired to be segmented. Instead, only prior information regarding the statistics of the data and pixel intensities being collected are necessary.

Overcoming the challenge of properly segmenting densely clustered cell nuclei is an ongoing issue. Several techniques have been developed to address cell splitting or separation, particularly for overlapping nuclei. For example, in [42], the authors developed a cell-tracking method for use with fluorescence microscopy. Level-sets are used to create an initial segmentation. In dense populations where cells are touching or overlapping, cell boundaries are approximated by a straight line that has the minimum average intensity. Alternatively, in [43], the authors developed a method for automatic segmentation of cell nuclei in histopathology images. An initial segmentation is obtained through the use of graph-cuts and a Laplacian-of-Gaussian (LoG) filter. Cell clusters are divided using a watershed transform along with minimizing an energy functional consisting of image gradient terms. Additionally, methods proposed in [36] identify and segment overlapping cells using a watershed technique with a post-processing merging step to overcome over-segmentation. Likewise, methods proposed in [44] also utilize watershed techniques to segment cell nuclei, but use specialized and controlled marker/seed selection. Meanwhile, using the assumption that the centers of nuclei are brighter or darker than nearby regions, authors in [45] segment touching and connected nuclei in three dimensional microscopy volumes. They accomplish this

using gradient flow tracking combined with an elastic deformation and local adaptive thresholding. Recently, authors in [46] have used the spikes of the outer medial axis of cells to detect and split touching cells. The work is based on the assumption that a cell is generally a convex object with an elliptical shape. In contrast, cells that are touching each other form boundary locations between the cells that are concave.

As previously described, since intravital microscopy image sets are obtained from living specimens, motion artifacts are introduced into the scene as a result of factors such as respiration and heartbeat. It has been demonstrated that using registration schemes can aid with segmentation, especially with volumetric data [47]. Therefore, using image registration as an intermediate or prerequisite step in image quantification and segmentation has been shown to be a very powerful approach in analyzing medical images.

Registration is often used in clinical settings with a wide variety of applications. For example, it is useful for reducing motion artifacts from patient motion, aligning patient data to an atlas (a standardized anatomical reference image whose intention is to be applicable for most patients), assisting with disease diagnosis and monitoring disease progression (such as cancer), and measuring anatomical variants between patients or among a population [48]. Additionally, information gathered from multiple imaging modalities is often complementary [49]. For instance, magnetic resonance imaging (MRI) is able to provide imaging of internal organs and soft tissue using non-invasive procedures and without exposure to ionizing radiation. At the same time, computed tomography (CT), positron emission tomography (PET), single photon emission tomography (SPECT), and MRI all provide separate but related and useful data.

Innovations are continuously being made in all aspects of registration. Some authors are proposing unique similarity metrics [50]. The work proposed in [51] uses a transformation model in the frequency domain, rather than the spatial domain, for use with three dimensional electron microscopy images of particles. The combination of both segmentation (using active contours) and registration (to remove jitter) has

been shown to be successful with tracking leukocytes *in vivo* in intravital microscopy videos [52]. Recently, work proposed in [53] uses non-rigid registration to decouple two types of motion relating to nuclei imaged using time-lapse microscopy: motion of the entire cell, and motion of the subcellular particles. Lastly, some are concerned about and making progress toward reducing computational complexity [54].

There exists much controversy over image analysis methods regarding multiphoton microscopy. Some argue [55] that user interaction is best suited since no automated procedure can truly reproduce the accuracy of a human in correctly identifying individual cellular objects. The authors of this work utilize dynamic programming and user-selected starting points to segment fluorescence images of whole cells and cell nuclei for the purpose of quantifying cell morphology, distribution, and organization. While the entire technique is not completely manual, it requires at least a manual input of an initial seed value or starting point. Additionally, several authors have based their image registration schemes on manually selecting landmarks [56–58]. Landmarks anchor and influence the transformation/deformation at specific locations within the images. Landmarks may be either hard landmarks where the registration will match at the landmark points exactly, or soft landmarks where their location is included in the computation along with other similarity and regularization terms such that they may not have an exact match after registration. Finding an optimal relation between images given specified landmarks is described as NP-hard, and therefore heuristics are often used to make the matching process practical [59]. Other authors have created semi-automatic methods by mixing the use of landmarks combined with contributions from image intensities [60]. However, this quickly becomes impractical as the number of images in a stack approaches hundreds of images. Therefore, others [40] argue that a completely automated process is necessary to obtain quantitative, objective, and repeatable results. User interaction causes varying results for identical input data sets which may be unacceptable in certain applications. Identifying landmarks in medical images requires expertise, which may be unavailable or impractical given the amount of data to undergo registration. Therefore, automatic image segmentation and regis-

tration is absolutely necessary for the quantification of multiphoton microscopy image sets, whose size and complexity make manual image analysis impractical [61].

Not only is the actual procedure of image registration challenging, but so is the evaluation of registration results. In a clinical setting, ground truth data (knowledge of the true registration parameters) are often unknown. The work proposed in [62] instead generates gold-standard data, where the true misalignment of the objects being imaged is fully known by using manual deformation. Authors in [63] develop a protocol to evaluate various similarity metrics based on accuracy, robustness, capture range, and risk of local minima/maxima. They test their protocol using both clinical data and phantom data where gold-standard registration parameters are known. Meanwhile, authors in [64] validate the effectiveness of non-rigid registration using both *in vivo* and simulated brain MRI data, measured by both maximum and average difference of deformation fields. Alternatively, some [65] have validated a registration method by comparing it to the results from previous registration methods. Validation may also be accomplished through the use of extrinsic markers (markers attached to or implanted in the object/specimen) or intrinsic markers (landmarks associated with natural anatomical features).

1.4 The Problem Formulation

This work describes a method to analyze multiphoton fluorescence microscopy images via a combination of segmentation and registration methods. Motivation for the development of this work is provided by the desire to address a set of mensuration problems in multiphoton fluorescence microscopy images. Intravital microscopy is a powerful technique for studying physiological processes in the most relevant context—in the living animal. However, developing assays of physiological function will require developing novel methods of digital image analysis that will support quantitative analysis. For example, biologists are interested in quantifying the number and size of cells and their progression, especially for cancerous tissues. Knowledge of the shape,

size, and motion of biological structures may aid in understanding and developing solutions for human and non-human diseases. Gaining this knowledge often requires the analysis of microscopy image sets and using segmentation methods to identify and separate relevant biological structures. Insofar as accurate image segmentation is prerequisite to quantitative analysis of time-series and volumetric image data, the development of effective methods of image registration is fundamentally important to realizing the potential of intravital microscopy as a tool for understanding and treating human diseases. While image segmentation and registration share many common interests, they are often treated as completely separate fields [66]. Instead, this work integrates the two fields into a method that complements each another.

While there are many different kinds of multiphoton fluorescence microscopy images, this work focuses on the analysis of two distinct types of data whose segmentation and quantification are affected by motion artifacts. With the development of optical sectioning techniques, it is now possible to collect image volumes in biological tissues and thus characterize biological structures in three dimensions. Therefore, one data set type consists of a progression of images corresponding to focal planes looking deeper in the tissue. This data set type is commonly referred to as "z-series" data, as the z-axis typically corresponds with depth. The other data set type consists of a progression of images corresponding to a series of time instances of a single focal plane. This data set type is commonly referred to as "time-series" data.

The general goal of this work is to segment and register a sequence or "stack" of multiphoton fluorescence microscopy images. Regarding z-series or three dimensional data sets (images consisting of progressive tissue depths), the images are acquired sequentially at various (known) depths across a three dimensional sample of tissue. Regarding time-series data sets, the images are acquired sequentially at evenly spaced time intervals across a single focal plane. Despite the distinct difference between these two modes of image acquisition, the two data set types share a set of common analysis goals and challenges [67].

Furthermore, since the image sets may be collected from living specimens, movement between images may be significant due to specimen motion during acquisition. Therefore, registration will be necessary to correct these movements between images. Registration is expected to improve segmentation performance and improve future quantification. However, any image registration methods we develop will need to be used judiciously when used with either three dimensional or time-series data. With regard to time-series data, motion will arise from one of two sources—motion arising from intrinsic cellular and subcellular processes where structures may truly have exhibited motion relative to other structures, and motion arising solely from extrinsic factors such as respiration and heartbeat. Both types of motion will manifest themselves as differences in each image collected in the time-series. The caveat is that we wish to eliminate the motion from respiration and heartbeat while simultaneously preserving the intrinsic differences and motion from cellular and subcellular processes. This decoupling of the two sources of motion is obviously non-trivial. With regard to three dimensional data, there will be expected differences between consecutive slices within the image set as different tissue depths are being imaged and structures change along the z-axis. Therefore, similar to time-series image sets, image registration must be used judiciously to correct extrinsic image differences arising from respiration and heartbeat while preserving intrinsic image differences due to imaging different tissue depths.

1.5 Contributions of This Thesis

In this thesis, we developed segmentation and registration methods to address the unique properties and characteristics of multiphoton microscopy images. The main contributions regarding these segmentation and registration methods are as follows:

- We combined well-established image analysis techniques in a novel and unique fashion to create integrated segmentation and registration methods for microscopy images. In particular, we utilize a Bayesian estimation technique

for denoising, low-pass filtering to provide blurring, adaptive thresholding to produce binary images, and morphological filtering for post-processing.

- We extend registration methods to handle challenges imposed by multiphoton microscopy. Microscopy images are often collected as entire data sets of images. While typical image registration methods may operate with just a single pair of images, we extend the methods and utilize registration with an entire data set often consisting of hundreds of images. Furthermore, these data sets often contain multi-channel color images. Traditional registration often assumes grayscale images. Therefore, we develop a metric for color images so that registration may be performed on these data sets.

- We borrow techniques from video compression, specifically motion estimation and compensation, and use this as a validation tool for our registration methods. Due to the lack of ground truth data, an effective validation method is necessary to quantitatively evaluate our registration results.

- We modify a three dimensional active surface segmentation method to better handle the characteristics of microscopy volumes. In particular, we reduce and simplify terms contained within the cost function and utilize pre- and post-processing techniques to reduce the interference caused by image noise.

1.6 Publications Resulting from This Work

Journal Publications

- **K. S. Lorenz**, P. Salama, K. W. Dunn, E. J. Delp, "Digital Correction of Motion Artefacts in Microscopy Image Sequences Collected from Living Animals Using Rigid and Non-Rigid Registration," *Journal of Microscopy*, vol. 245, no. 2, pp. 148-160, February 2012.

- R. G. Presson Jr., M. B. Brown, A. J. Fisher, R. M. Sandoval, K. W. Dunn, **K. S. Lorenz**, E. J. Delp, P. Salama, B. A. Molitoris, I. Petrache, "Two-Photon

Imaging within the Murine Thorax without Respiratory and Cardiac Motion Artifact," *The American Journal of Pathology*, vol. 179, no. 1, pp. 75-82, July 2011.

Conference Publications

- **K. S. Lorenz**, P. Salama, K. W. Dunn, E. J. Delp, "A Multi-Resolution Approach to Non-Rigid Registration of Microscopy Images," *Proceedings of the IEEE International Symposium on Biomedical Imaging*, Barcelona, Spain, 2-5 May 2012.

- **K. S. Lorenz**, P. Salama, K. W. Dunn, E. J. Delp, "Non-rigid registration of multiphoton microscopy images using B-splines," *Proceedings of SPIE Medical Imaging 2011: Image Processing*, Lake Buena Vista, FL, 12-17 February 2011.

- **K. S. Lorenz**, F. Serrano, P. Salama, E. J. Delp, "Segmentation and Registration Based Analysis of Microscopy Images," *Proceedings of the IEEE International Conference on Image Processing*, Cairo, Egypt, 7-11 November 2009.

- **K. S. Lorenz**, F. Serrano, P. Salama, E. J. Delp, "Analysis of Multiphoton Renal and Liver Microscopy Images: Preliminary Approaches to Segmentation and Registration," *Proceedings of the Workshop on Microscopic Image Analysis with Applications in Biology*, Bethesda, MD, 3-4 September 2009.

2. INTEGRATED SEGMENTATION AND REGISTRATION

The motion of particular cellular objects may be exaggerated by specimen respiration and heartbeat. By introducing an approach combining registration along with segmentation, motion artifacts within the scene may be reduced. As a result of the analysis described in this chapter, changes in shape, size, and motion of cellular structures may then be better visualized.

The proposed analysis system is shown in Figure 2.1 [68]. First, each image in the image stack is denoised via a Bayesian estimation technique [69]. Each image is then low-pass filtered to provide some local blurring and is subsequently spatially registered. One dimensional smoothing along the vertical (depth/time) axis after the images have been aligned is then performed. This is followed by adaptive thresholding to produce a binary image. Finally, the segmentation mask is filtered using morphological techniques. This new mask is then used to segment each image.

2.1 Maximum a Posteriori Filtering

The first step in this approach is a denoising filter. Specifically, this filter is a maximum *a posteriori* (MAP) filter [69] which takes advantage of the known characteristics of the noise. Due to the photon-counting nature of the image acquisition process, photon noise is known to predominantly have a Poisson distribution [70]. By utilizing this additional information about the characteristics of photon noise, cellular objects become more well-defined, enhancing the performance of the segmentation process to follow. Figure 2.2 shows the effects of the filter on an example image consisting of kidney nuclei.

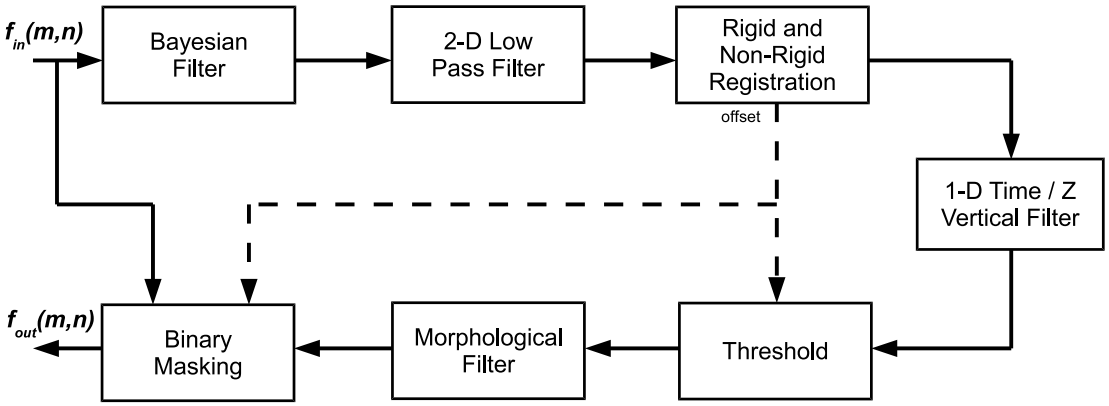

Fig. 2.1.: Block diagram of our proposed analysis system

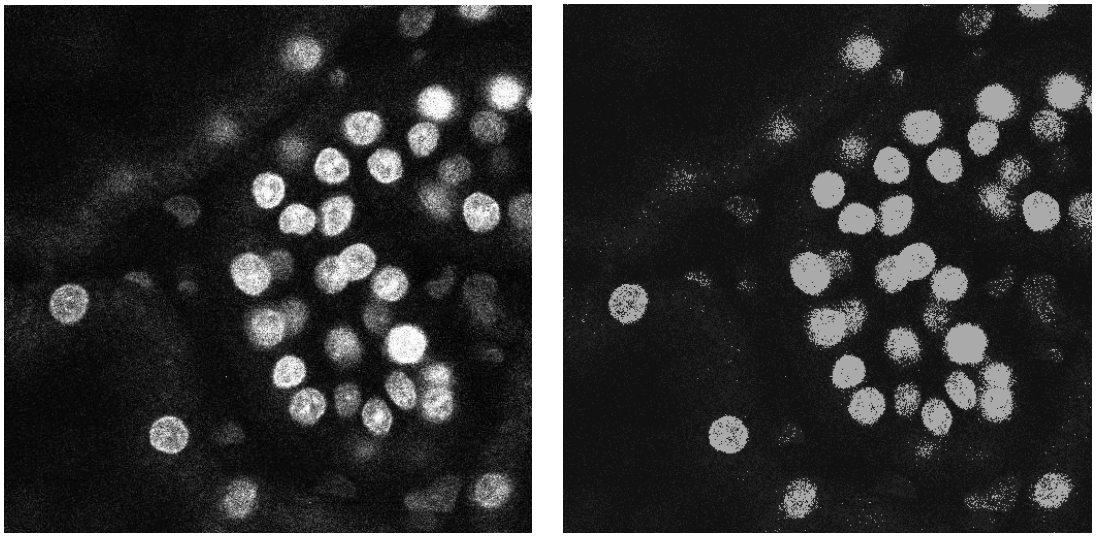

(a) Original image (b) MAP filtered image

Fig. 2.2.: Maximum *a posteriori* filtering of example image

2.2 2-D Spatial Low-Pass Filtering

After denoising, each image is then low-pass filtered to provide local blurring using a 3×3 low-pass filter with impulse response:

$$h(m,n) = \begin{cases} 0.2 & \text{if } (m,n) = (0,0) \\ 0.1 & \text{if } |m| \text{ or } |n| = 1 \\ 0 & \text{else} \end{cases} \tag{2.1}$$

Our experiments have shown that this blurs the image so that segmentation is more robust. The blurring process mitigates noise remaining in the image after the Bayesian denoising filter is used. A similar approach was adopted in [32]. It is believed that blurring traditionally reduces segmentation performance, as object boundaries become less well-defined. However, object boundaries in our images are poorly defined in the sense that they are not composed of rigid continuous edges. In this case, blurring the objects improves the segmentation by creating more well-defined continuous boundaries in contrast to ill-defined sparse boundaries. The coefficients of this filter were selected empirically.

2.3 Registration

Optical microscopy image sets may be obtained from live specimens via a technique known as intravital microscopy. These studies frequently involve collecting a series of images, either for characterizing three dimensional volumes of the specimen or for studying biological processes in time-series. These image volumes are compromised to varying degrees by motion artifacts resulting from factors such as respiration and heartbeat. These factors change the position and shape of the sample volume such that sequential images are not registered with one another. These motion-induced artifacts can be addressed through the use of image registration, which aligns the images (spatially and/or temporally) so that they all share a common coordinate system, a condition aiding in future image analysis.

Since registration is an in-depth topic itself, registration is described in detail in Chapter 3. The following sections in this chapter finish the image analysis following the registration described in Chapter 3.

2.4 1-D Low-Pass Filtering

Up to this point in our processing methods, any information about the current image that is contained in previous and/or future images has not been utilized. If a particular object was segmented in the previous image, it is highly likely that this same object should also appear and be segmented in the current image. We observed in our images, particularly for z-series data sets, that the intensity of a specific pixel related to an object of interest, as a function of depth (image number), starts out low, increases as the dye concentration in the object of interest increases in the current focal plane, peaks, and then decreases as the object fades away. However, noise interferes with this expected behavior, as seen in Figure 2.3(a), which displays an example of the pixel intensity as a function of image number. For example, within the large distinct peak, there exists a momentary sharp decrease in pixel intensity below the noise floor, such that using a simple static thresholding technique to address this issue would not suffice. With the noise inducing sharp discontinuities in pixel intensity, objects segmented in the current image may disappear in the next image, then reappear in the following image. Therefore, to address this effect and restore the expected behavior of a pixel's intensity as a function of image number, a 1-D low-pass filter is used across the images. The filter is given by:

$$T_n = \frac{1}{4}I_n + \frac{1}{2}I_{n-1} + \frac{1}{4}I_{n-2} \tag{2.2}$$

where T_n denotes the n-th filtered image corresponding to the n-th input image I_n and its two preceding images I_{n-1} and I_{n-2} respectively. Only three images have non-zero coefficients because including more than three images in the filter is illogical due to the physical dimensions of the images. Particularly for z-series data sets, the resolution for the z-axis is approximately three to five times less than the resolution for the x- and y-axes [71,72]. This is a characteristic of the image acquisition system that cannot be modified. Therefore, including more than three images in the filter may include data beyond the boundaries of objects in the current image. The coefficients

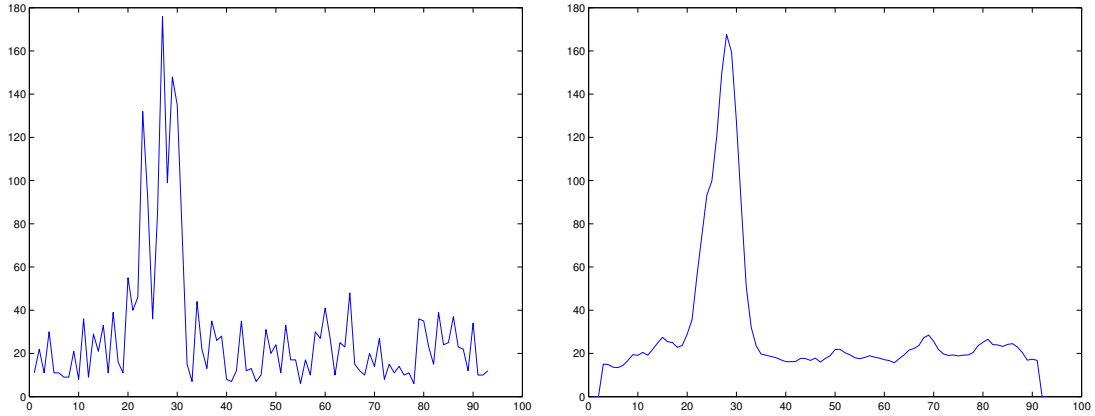

(a) Pixel values before 1-D filtering (b) Pixel values after 1-D filtering

Fig. 2.3.: Pixel intensity vs. tissue depth

of this filter were selected empirically. The filter is chosen so that the system remains causal to aid in consideration of future low-latency real-time implementations. The largest coefficient is chosen to correspond with the first previous image. Therefore, the system will have a time delay of one image. For images at the beginning of the sequence, where not all of the two previous images are available, the n-th filtered image is obtained by:

$$\begin{aligned} T_n &= \frac{1}{2} I_n + \frac{1}{2} I_{n-1} \\ T_n &= I_n \end{aligned} \tag{2.3}$$

The filtered intensity profile corresponding to Figure 2.3(a) is shown in Figure 2.3(b). We observed that if consecutive images have significant movement or displacement, then any analysis following the 1-D filtering fails. This is because the relationship between image number and pixel intensity shown in Figure 2.3 is no longer valid. Therefore, this motion must be corrected using registration before the 1-D filter.

2.5 K-Means Threshold

After filtering and registration followed by additional filtering, a thresholding approach is implemented to detect whether an object should or should not be segmented. Using a static threshold obtained subjectively may work for a given specific data set, but would not be adaptive to other data sets. Therefore, K-means is used to adaptively determine a threshold to generate binary images to serve as segmentation masks [73]. The algorithm was executed with $K = 2$ for two groups, producing a binary image. The objective here is to generate image-dependent thresholds, whereby binary segmentation masks can be constructed. The obtained threshold clusters each pixel from every image into one of two classes, segmented and unsegmented objects.

K-means is an iterative method that performs thresholding based on the image histogram. In each iteration, the average of the foreground and background class means were used. These are defined as:

$$\begin{aligned} m_b(T_n) &= \sum_{g=0}^{T_n} gp(g) \\ m_f(T_n) &= \sum_{g=T_n+1}^{G} gp(g) \end{aligned} \tag{2.4}$$

where m_f and m_b are the computed means for the foreground and background respectively, T_n is the value of the threshold (initialized to 256/2), $p(g)$ is the value of the histogram for the intensity g, and G is the maximum intensity possible (generally 255 for 8-bit images). After the means are estimated, a new threshold is obtained as:

$$T_{n+1} = \frac{m_f(T_n) + m_b(T_n)}{2} \tag{2.5}$$

Finally, the K-means iterations stop once $|T_n - T_{n-1}| < \alpha$ (with $\alpha = 1$ chosen to obtain close convergence). All images in every data set analyzed required less than ten iterations.

Each binary mask was initially obtained by setting all pixels whose values fall below the image's corresponding threshold to zero, and those whose values are greater than or equal to the threshold to 255. We observed that the threshold does not change drastically between consecutive images. Therefore, K-means does not have to be used for every image, rather only when there is significant motion or signal attenuation with increasing depth.

2.6 Morphological Filtering

Upon examining the resulting binary segmentation masks, we observed that they often contained small black holes inside objects and small white objects in the background. To remove these isolated objects, several morphological filters were used [74]. First, a binary morphological opening with a flat, square 7×7 structuring element was used to remove small objects. Next, a morphological closing with a flat, square 4×4 structuring element was used to remove small holes. The sizes of these structuring elements were selected empirically. This resulted in the final binary masks used to segment the original images.

2.7 Binary Masking

After the morphological filtering, from these binary images, the final output images are created. For black pixels in the binary image, the corresponding pixels in the output image remain black. For white pixels in the binary image, the corresponding pixels in the output image are restored to the corresponding pixels in the original image. The binary image acts as a segmentation mask for the original image:

$$F(m,n) = B(m,n)O(m,n) \tag{2.6}$$

where O is the original image, B is the corresponding binary mask, and F is the final segmented image.

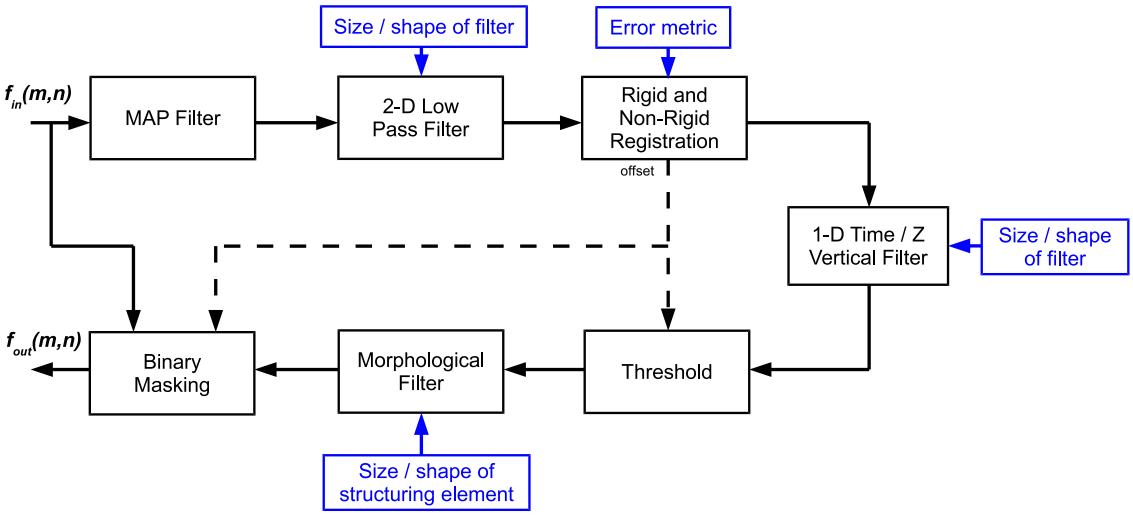

Fig. 2.4.: User adjustable parameters in block diagram

2.8 User Adjustable Parameters in Proposed Approach

The proposed approach has completely automated the image analysis of all data sets. However, user interaction may be introduced to modify certain parameters of the analysis. Specifically, in the proposed approach, the following five components of the block diagram shown in Figure 2.1 may be modified by the user: 2-D spatial low-pass filter, registration, 1-D low-pass filter, thresholding technique, and morphological filter. These parameters may be adjusted depending on specific input data sets to produce more desired results. A diagram depicting these user adjustable parameters is shown in Figure 2.4.

2.8.1 2-D Spatial Low-Pass Filtering

The simplicity of the 2-D low-pass blurring filter lends itself well to this application. Other filters such as Gaussian smoothing [75] have a high computation cost without necessarily producing improved results. One may perceive that an edge-

preserving smoothing filter would improve results. However, due to the characteristics of image noise, the edge-preserving filter will perform poorly, as edges of objects are not well defined in the original image data.

Additionally, the form of the 2-D spatial low-pass filter introduced previously was selected experimentally. The coefficients and dimension of the filter may be modified to produce slightly different blurring effects. A filter with impulse response:

$$h = \begin{bmatrix} 0.03 & 0.03 & 0.03 & 0.03 & 0.03 \\ 0.03 & 0.05 & 0.05 & 0.05 & 0.03 \\ 0.03 & 0.05 & 0.12 & 0.05 & 0.03 \\ 0.03 & 0.05 & 0.05 & 0.05 & 0.03 \\ 0.03 & 0.03 & 0.03 & 0.03 & 0.03 \end{bmatrix} \tag{2.7}$$

with $h(0,0) = 0.12$ being the center element of the filter, has also shown to produce acceptable results. If desired, the user may be allowed to completely specify and adjust the form of the filter.

2.8.2 1-D Low-Pass Filtering

To avoid delays in the system, the 1-D vertical low-pass filter can be made non-causal. This is possible if the entire series of images in a data set is fully available before analysis is performed. The filter can now be given by:

$$T_n = \frac{1}{4}I_{n-1} + \frac{1}{2}I_n + \frac{1}{4}I_{n+1} \tag{2.8}$$

where T_n denotes the n-th filtered image corresponding to the n-th input image I_n and its preceding and succeeding images I_{n-1} and I_{n+1}, respectively. Implementing this filter requires analyzing all input images twice, once for the spatial low-pass filter, and a second time for the 1-D low-pass filter. For images at the beginning and end of the sequence, where the preceding or succeeding images are not available, the n-th filtered image is obtained by:

$$T_n = \frac{1}{2} I_{n-1} + \frac{1}{2} I_n$$
$$T_n = \frac{1}{2} I_n + \frac{1}{2} I_{n+1} \tag{2.9}$$

Additionally, similar to the 2-D spatial low-pass filter, the form of the 1-D low-pass filter introduced previously was also selected experimentally. The coefficients and length of the filter, for both the causal and non-causal cases, may be modified to produce slightly different smoothing effects.

However, the resolution of the capture device across the z-axis (tissue depth) is approximately four times worse than the horizontal or vertical resolution contained within a single image. As a result, voxels are not square, but instead are rectangular. Therefore, a progression of images corresponds to a relatively large change in depth. As a result, it may be undesirable for the 1-D low-pass filter to consider data from slices more than one image away from the current image.

2.8.3 K-Means Threshold

Alternative thresholding techniques in addition to K-means may be considered. A very popular binary thresholding technique is Otsu's method [76]. To obtain a threshold value, this method minimizes the weighted sum of intra-class variances of foreground and background pixels:

$$\sigma_w^2(k) = \omega_0(k)\sigma_0^2(k) + \omega_1(k)\sigma_1^2(k) \tag{2.10}$$

where k is the current threshold, ω_i are the weights or probabilities of the two classes, and σ_i are the variances of the two classes. Minimizing the intra-class variance is equivalent to maximizing the inter-class variance:

$$\sigma_b^2(k) = \omega_0(k)\omega_1(k)[\mu_0(k) + \mu_1(k)]^2 \tag{2.11}$$

where μ_i are the means of the two classes. The final threshold k^* is the value that maximizes $\sigma_b^2(k)$. The straightforwardness and effectiveness of the Otsu thresholding method makes it still one of the most popular thresholding techniques to date [77]. By replacing the K-means method with Otsu's method, segmentation results remained consistent while computational complexity was significantly reduced. Therefore, Otsu's method may be considered as a permanent substitution for K-means.

2.8.4 Morphological Filtering

The size and shape of the structuring elements used in the morphological filter were also selected experimentally. By altering the size and shape of the structuring elements for the opening and closing operations, the user can remove smaller or larger objects, and remove smaller or larger holes, respectively, from the binary mask.

2.9 Summary of Experimental Results

We will demonstrate our integrated segmentation and registration method in the beginning sections of Chapter 6. More specifically, we will show rigid registration results followed by segmentation results in Section 6.1. These results will demonstrate the effectiveness of our segmentation method for multiphoton microscopy image series on a slice-by-slice basis. For particular data sets exhibiting channel crosstalk and lack of channel isolation, we will describe a pre-processing method in Section 6.2 to mitigate these factors. Lastly, to give readers insight into how each step in the block diagram shown in Figure 2.1 affects the analysis of each image slice, figures showing the intermediate results following each step will be shown in Section 6.3.

3. IMAGE REGISTRATION AND MOTION ARTIFACT CORRECTION

Image registration is the task of finding a function that maps coordinates from a moving test image to corresponding coordinates in a reference image [12]. Medical image registration often involves finding a mapping from a single image in one modality to a single image in another modality. This is known as multi-modality image registration. For example, it is commonly useful to register an image acquired using PET (positron emission tomography) with an image acquired using MRI (magnetic resonance imaging). Images from PET scans provide functional information such as bodily fluid flow but generally have low resolution. In contrast, images from MRI scans provide structural information and generally have higher resolution. Therefore, it is often desirable to transform information obtained from multiple images into a single common coordinate system, encompassing the knowledge available from all the various source images [78]. Medical image registration is also commonly used to register two images from a single modality, also known as mono-modality image registration. For example, it is useful to register two MRI images acquired at different times to possibly determine how body structures have evolved or shifted over time. Mono-modality registration methods generally assume that pixels representing the same homologous points on an object have the same intensity in both the reference and test images [79]. However, both mono- and multi-modal current registration methods generally consider registering only a single pair of reference and moving images. Using medical image registration on stacks containing hundreds of images is still an ongoing field of research.

Image registration techniques can be classified in one of two groups: feature-based or intensity-based [80]. Feature-based methods match contours or landmarks in the

test image with the same features and points in the reference image. Features and landmarks may be identified either manually, automatically, or semi-automatically. Errors in automatic feature detection may cause catastrophic failure of feature-based registration. In contrast, intensity-based methods use intensity values directly, assuming that intensity values contain all information necessary for registration. Feature-based methods are commonly associated with multi-modal image registration as corresponding points in the test and reference images are assumed to have different intensities. Likewise, intensity-based methods are commonly associated with mono-modal image registration as corresponding points in the test and reference images are assumed to have the same intensity. Since manually selecting landmarks in a data set consisting of hundreds of images is overburdening, and automatically selecting precise landmarks in noisy, low-resolution images is difficult, we prefer to explore intensity-based methods over feature-based methods, as was similarly argued in [81]. With intensity-based methods, all image pixels are used in the registration computation, effectively using all available information given in the image data.

A registration method consists of four primary components: a transformation model, a similarity metric, an optimization procedure, and an interpolation method [82]. The transformation model or mapping should be matched with the underlying cause of the misalignment. The similarity metric should be one that is least sensitive to image noise and best models image alignment. The optimization or search strategy may depend on the image characteristics, such as whether gradient information or edge detail is readily available or not. The choice of an interpolation method may depend on computational complexity limitations of the system.

Here, we describe an image processing method that effectively corrects for motion artifacts in sequences of intravital microscopy images collected in time-series or in three dimensional volumes, based upon a combined rigid and non-rigid registration technique. This image registration method will aid in future segmentation and other image analysis techniques. In particular, the proposed image registration method consists of two distinct components: a rigid registration component that corrects

global translations, and a non-rigid registration component to correct localized, non-linear motion artifacts [83]:

$$\mathbf{T}(x, y) = \mathbf{T}_{non-rigid}\left(\mathbf{T}_{rigid}(x, y)\right) \tag{3.1}$$

We will demonstrate that this registration technique is effective for correcting motion artifacts in image sequences collected in time-series or in three dimensions.

3.1 Rigid Registration

Rigid registration preserves the distances between all pairs of points in both images [84]. This technique is first performed to correct global translations throughout the image sequence before non-rigid registration so that the non-rigid process focuses solely on localized motion rather than both local and global motion. The registration technique we used was initially obtained from ITK[1]. A complete guide of this image processing toolkit is presented in [85]. Registration within ITK requires several parameters to be specified. An extended description of these parameters along with an overview of all components of the registration process can be found in [86]. All user adjustable parameters and their corresponding options for registration are presented in Table 3.1, with the selected options used in this approach shown in bold. The particular registration parameters selected for this approach include a Neumann boundary condition, where pixel values outside of the image boundary are given the values of the nearest pixel within the image boundary. Additionally, registration is performed using nearest-neighbor interpolation. Furthermore, an exhaustive search is not performed to compute the optimal registration solution. Instead, several optimization methods have been studied [87, 88]. Our registration implementation employs the well-known quasi-Newton BFGS (Broyden-Fletcher-Goldfarb-Shanno) optimizer. This optimization method greatly reduces computational complexity by estimating the Hessian

[1]National Library of Medicine Insight Segmentation and Registration Toolkit (http://www.itk.org)

Table 3.1: ITK registration parameters

Parameter	*Options Available* ***Option Selected***
Boundary condition	**Neumann** Constant padding Circular
Error metric	**Mean squared error** Normalized correlation Mean reciprocal squared difference Mutual information Kullback Liebler distance metric Normalized mutual information Mean squares histogram Correlation coefficient histogram Cardinality match Kappa statistics Gradient difference
Optimizer	Amoeba Conjugate gradient Gradient descent Quaternion rigid transform gradient descent Limited memory minimization Bounded limited memory minimization One plus one evolutionary **Regular step gradient descent** Powell Simultaneous perturbation stochastic approximation Versor transform Versor rigid 3D transform
Interpolator	**Nearest neighbor** Bilinear B-Spline Windowed sinc

matrix rather than computing it directly. As a result, the error metric is evaluated for only a small subset of all possible registered offset locations [86].

The registration metric used was mean squared error:

$$(u, v) = \underset{(u,v)}{\operatorname{argmin}} \left\{ \sum_{m=0}^{M-1} \sum_{n=0}^{N-1} (x_{i-1}(m, n) - x_i(m - u, n - v))^2 \right\} \tag{3.2}$$

where i denotes the current image number, $x_{i-1}(m, n)$ and $x_i(m, n)$ denote the pixels at location (m, n) within the reference image x_{i-1} and moving image x_i respectively, and (u, v) denotes the obtained registration offset distances. A comprehensive comparison of metrics used in medical image registration is given in [89]. The mean squared error metric is a common metric with a large capture radius [11]. In order to register an entire stack of images, the moving test image was chosen to be the current image, and the reference image was chosen to be the previous (unregistered) image. If the registration of the current image in reference to the previous image is denoted as $\mathbf{r}(x_i, x_{i-1}) = x_i \circ x_{i-1}$, the output of the registration process in terms of the first image can be represented as a concatenation of all previous registrations:

$$\mathbf{r}(x_i, x_1) = \mathbf{r}(x_i, x_{i-1}) \circ \mathbf{r}(x_{i-1}, x_{i-2}) \circ \cdots \circ \mathbf{r}(x_2, x_1) \tag{3.3}$$

as was similarly performed in [90]. This was found to greatly improve registration performance instead of using the first image in the stack as the reference image, as well as reduce the computational complexity and consequently the time required to analyze the entire series. In fact, the current image may contain few of the same structures also visible in the first image if the sequence has already significantly progressed into the stack of images. This result was especially true for three-dimensional/volumetric data, or image sequences corresponding with increasing tissue depth. Using a pre-selected image in the stack as the reference image has undergone experimentation using time-series data, or image sequences corresponding with increasing time instances, as the same cellular objects are expected to be in view for every image in the sequence. However, no noticeable improvement was observed.

If the system is not required to be real-time when the entire stack of images is available, the system can be implemented using non-causal methods. In our rigid-

registration approach, the output image size is unknown unless the maximum total displacement due to registration is known. However, this information is not available until the entire data set has been analyzed. For the system to be causal, an assumption about the output image size must be made, and the placement of the first image in the output image must be chosen. However, with a non-causal approach, the system has the advantage of being able to analyze the entire data set before producing any output images. After all images have been analyzed, the maximum displacement across all images can be determined to set the output image size so that no source images are truncated. For the sake of simplicity, we will assume the system is not utilized in a real-time scenario, and is implemented using non-causal methods.

3.1.1 Color to Grayscale Conversion

Additionally, this registration method assumes grayscale single channel images, not multi-channel images. Therefore, for multi-channel data sets, a particular channel must be selected to perform registration on. Simply using one of the multiple channels directly may be enticing due to its simplicity. However, using only one of the channels and discarding the remaining channels omits much information which may cause improper image registration in these discarded channels. There are many regions in each image where a particular channel exhibits/contributes very little signal. As a result, these regions are registered improperly. Therefore, perhaps contrary to logical assumption, we have obtained results with higher registration accuracy using a composite gray channel, I_{gray}, that is similar to the luminance component of each image. This new gray image used with our registration method is given as:

$$I_{gray} = \frac{r}{r+g+b} I_{red} + \frac{g}{r+g+b} I_{green} + \frac{b}{r+g+b} I_{blue} \tag{3.4}$$

where

$$r = \sum_{m=0}^{M-1} \sum_{n=0}^{N-1} I_{red}(m,n)$$
$$g = \sum_{m=0}^{M-1} \sum_{n=0}^{N-1} I_{green}(m,n) \tag{3.5}$$
$$b = \sum_{m=0}^{M-1} \sum_{n=0}^{N-1} I_{blue}(m,n)$$

and where I_{red}, I_{green}, and I_{blue} denote the red, green, and blue components of the input image x, respectively. Even though a linear combination of the three channels has no biological significance, using gray composite images for registration has corrected significantly more motion artifacts than using any individual channel for the images that we have evaluated thus far, as the composite gray image contains and uses information from the entire image. However, one can easily imagine situations in which a particular channel might provide better registration results, as these results will depend upon the particular data being analyzed. For each image, a final registration result based on the gray image is obtained. This registration result is then used to transform all channels of the image.

When experimenting with a fixed linear combination, such as constructing this gray level image by computing the luminance component of the image:

$$I_{gray} = 0.2989 * I_{red} + 0.5870 * I_{green} + 0.1140 * I_{blue} \tag{3.6}$$

this showed to be not as effective, as channels with large contributions to the overall image were not weighted to impact the registration proportionally.

3.1.2 Alternative Metrics

In addition to the mean squared error metric used, the following metrics have been evaluated:

$$\begin{aligned}(u,v) &= \underset{(u,v)}{\operatorname{argmax}} \left\{ \sum_{m=0}^{M-1} \sum_{n=0}^{N-1} x_{i-1}(m,n) x_i(m-u,n-v) \right\} \\ (u,v) &= \underset{(u,v)}{\operatorname{argmin}} \left\{ \sum_{m=0}^{M-1} \sum_{n=0}^{N-1} |x_{i-1}(m,n) - x_i(m-u,n-v)| \right\}\end{aligned} \tag{3.7}$$

where $x_{i-1}(m,n)$ and $x_i(m,n)$ denote the pixels at location (m,n) within the reference image and moving image, respectively. Registration was performed using both metrics, and the results were observed to be visually identical to those using the mean squared error metric. If the reference images are binary, computation will be greatly reduced using the first metric, where a logical `AND` operation is significantly faster than a subtraction operation.

Furthermore, the use of mutual information as a metric has been evaluated [91]. This consisted of maximizing the following:

$$(u,v) = \underset{(u,v)}{\operatorname{argmax}} \{MI(x_{i-1}(m,n), x_i(m-u,n-v))\} \tag{3.8}$$

where

$$\begin{aligned}MI(x(m,n), y(m-u,n-v)) = H(x(m,n)) + H(y(m-u,n-v)) \\ - H(x(m,n), y(m-u,n-v))\end{aligned} \tag{3.9}$$

is the mutual information between $x(m,n)$ and $y(m-u,n-v)$, and H denotes Shannon entropy [92]. The mutual information implementation from Mattes et al. [93] has been used here. Results from the use of these metrics will be discussed in Section 6.1.

3.2 Non-Rigid Registration

Thus far, this thesis has only introduced image registration that attempts to correct global translations. We will now attempt to address the motion artifacts and non-linear distortions caused by respiration and heartbeat using non-rigid registration. In contrast to rigid registration, non-rigid registration maps straight lines to curves [84].

Common image registration approaches are based upon a rigid frame translation, but because of the slow frame rate of laser point scanning microscope systems, images collected from living animals typically have complex intrascene distortions that are not corrected with rigid translations. In a scanning multiphoton fluorescence microscope, a two-dimensional image is assembled by sequentially scanning a series of horizontal lines across a sample. Because of the method of scanning, adjacent pixels are collected only microseconds apart in the horizontal direction, but are collected milliseconds apart in the vertical direction. For this reason, motion artifacts frequently appear in horizontal banding patterns. In fact, motion artifacts will be apparent at any frame rate, differing only in their relative manifestation as distortions between or within frames. Correcting these artifacts is significantly more challenging.

Previously developed and well-established registration methods may be used to process stacks consisting of multiple images [94]. However, these methods implement an affine registration. Affine registrations account for transformations including translation, rotation, scaling, and shearing. However, these transformations alone are insufficient to register image sequences collected *in vivo*. The dynamic motion from living animals introduced from respiration and heartbeat cannot be described with an affine transformation.

Non-rigid image registration is considered slower, less robust, and less reliable than rigid registration. Non-rigid registration is also often described as an ill-posed problem. One may even argue that it is inherently impossible to register two images, as the difference between the two images may contain the relevant and useful infor-

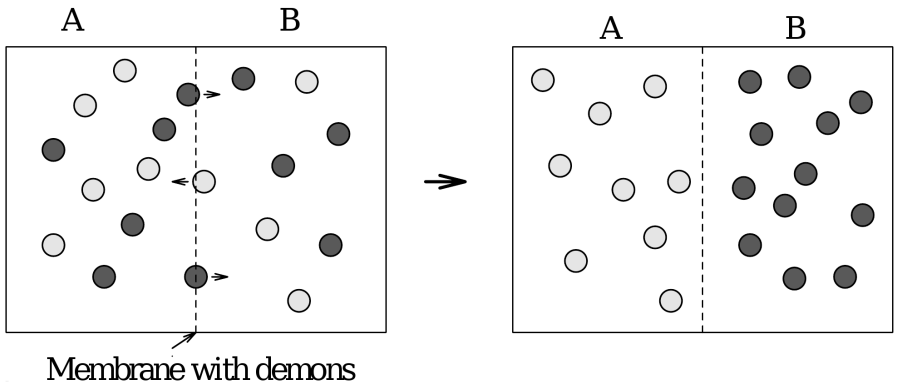

Fig. 3.1.: Demons registration algorithm

mation [95]. Therefore, "over-registration" may be an issue. However, the gains in image analysis from non-rigid registration far outweigh many of its pitfalls.

3.2.1 Demons Algorithm

Here, we will investigate an application of Thirion's "demons" algorithm [96], an iterative non-rigid registration method. The concept of demons is a thought experiment originally introduced by Maxwell to demonstrate a thermodynamics paradox. Assume a container is divided into two sections, A and B. A gas composed of two types of particles, a and b, fill both sections of the container. Imaginary demons guard the barrier between the two sections and are able to distinguish between the two types of particles. The demons allow particles of type a to enter section A but never come back to section B. Likewise, the demons also allow particles of type b to enter section B but never come back to section A. Eventually, all particles of type a will be in section A and all particles of type b will be in section B. Figure 3.1 illustrates this process [97]. This separation of particle types corresponds with a decrease in entropy, paradoxically violating the second law of thermodynamics. However, the paradox is solved because the demons must increase the entropy of the system to correctly identify particles.

In contrast to other more conventional non-rigid registration deformations, the demons algorithm is a diffusion model rather than an attraction model. Attraction models rely on the notion of distance, while diffusing models rely on the notion of polarity of being inside or outside a boundary. In an attraction-based model, a point P in the test image experiences a force or attraction by all points P' in the reference image according to pre-defined similarity and distance metrics. A larger attraction or force is typically the result of a larger similarity and smaller distance. However, attraction-based models are known to have large computational complexity, as for each iteration and for each point P, a large number of attraction points P' must be considered. In contrast, the demons algorithm borrows concepts from optical flow, whereby the intensity of a moving object is constant with time [97]:

$$\vec{v} \cdot \vec{\nabla} s = m - s \tag{3.10}$$

where s is the intensity of point P in the static or reference image S, m is the intensity of point P in the moving or test image M, and v is the displacement or optical flow between the images of point P to P'. However, this constraint is not sufficient to define the velocity $\vec{v}$. By including adjustments for regularization and normalization, the optical flow equation becomes:

$$\vec{v} = \frac{(m-s)\vec{\nabla} s}{|\vec{\nabla} s|^2 + (m-s)^2} \tag{3.11}$$

The gradient of the static image, $\vec{\nabla} s$, is an "internal" force representing the relationship among the neighboring points within the image. The $m - s$ difference term is an "external" force representing the differential force of the interaction between the static and moving images [98].

The concept of Maxwell's demons is migrated to image processing by creating a set of demons for the moving (or test) image, selected as either all of the pixels in the image (one demon per pixel) or a subset of the pixels (contour points extracted by edge detection or from prior segmentation). For simplicity and to utilize the

information contained in the entire image, we assign a demon to every pixel in the image. The method proceeds as follows: The deformation field is initialized as the identity transformation. For each iteration, an instantaneous force for each demon vertex in the grid is computed according to the optical flow equation previously described. This will produce an irregular deformation field, which is then regularized by a Gaussian filter with a variance of σ^2. These two steps of finding the force or displacement for every vertex or demon, and then regularizing the deformation field, is repeated until convergence. The regularization is necessary because each pixel in the image is free to move independently. It is possible that all pixels with one particular intensity in M map to a single pixel having this same intensity in S, and the resulting deformation field will be unrealistic [99]. This is one of the primary reasons why non-rigid image registration is considered difficult, as an appropriate balance and compromise must be reached between allowing large amounts of independent movement and ensuring smoothness of the transformation.

3.2.2 Non-Rigid Registration Using B-Splines

The non-rigid registration technique described in the previous section produced inconsistent results, which will be highlighted in Section 6.5.1. This is most likely due to the image data containing noise with a Poisson distribution, as the demons algorithm has been demonstrated to perform poorly with noisy images [100]. Therefore, we now turn to an alternative non-rigid registration method to identify, address, and correct localized motion artifacts caused by respiration heartbeat in sequences of intravital microscopy images. Here, we investigate a non-rigid registration technique using B-splines, a method that allows for easy visualization of the distortion and also leads to realistically registered images. B-splines hold many attractive and mathematically optimal properties [101]. For example, regarding interpolation, B-splines provide the best performance while simultaneously providing the least complexity [102].

This method, which is an extension of the work proposed in [103], deforms an image by first establishing an underlying mesh of control points. The control points are then optimized such that they maintain a smooth and continuous transformation. To begin, a grid of control points, $\phi_{i,j}$, is initially constructed with equal spacings δ_x and δ_y between points, in the horizontal and vertical directions, respectively. The non-rigid transformation $\mathbf{T}$ of a point (x, y) in the image being registered to the corresponding point (x', y') in the reference image is given by the mapping $\mathbf{T}(x, y) \rightarrow (x', y')$ [104]:

$$\mathbf{T}(x, y) = \sum_{l=0}^{3} \sum_{m=0}^{3} B_l(u) B_m(v) \phi_{i+l, j+m} \tag{3.12}$$

where $i = \lfloor x/\delta_x \rfloor - 1$ and $j = \lfloor y/\delta_y \rfloor - 1$ are the indices of the nearest control point $\phi_{i,j}$ above and to the left of (x, y), and $u = x/\delta_x - \lfloor x/\delta_x \rfloor$ and $v = y/\delta_y - \lfloor y/\delta_y \rfloor$ are such that (u, v) is the relative position of (x, y) relative to $\phi_{i,j}$. Additionally, B_l represents the l-th basis function of the B-spline [105]:

$$\begin{aligned} B_0(t) &= (1-t)^3/6 \\ B_1(t) &= (3t^3 - 6t^2 + 4)/6 \\ B_2(t) &= (-3t^3 + 3t^2 + 3t + 1)/6 \\ B_3(t) &= t^3/6 \end{aligned} \tag{3.13}$$

In contrast to many other non-rigid registration schemes, the registration of a point in an image when using B-splines is only determined by the area immediately surrounding the nearest control points, resulting in very localized deformations [104].

The optimal deformation of the grid of control points is found by optimizing a cost function. This cost function includes two terms with two competing goals. The first goal is to maximize the similarity and alignment between the reference image and the image being deformed. The second goal is to smooth and regularize the deformation to create a realistic transformation. The similarity metric, $C_{similarity}$, may be defined

as one of numerous possibilities, including sum of squared differences, sum of absolute differences, or normalized mutual information, whichever may fit the particular image set best. We use sum of log of absolute differences:

$$C_{similarity}(I_1, I_2) = \frac{1}{XY} \sum_{x=0}^{X-1} \sum_{y=0}^{Y-1} log(|I_1(x,y) - I_2(x,y)|+1) \tag{3.14}$$

where X and Y are the horizontal and vertical dimensions of the image in pixels, respectively. While being an uncommon metric, our experiments have shown that this similarity metric significantly outperformed any other metrics for our microscopy image sets, both from a qualitative viewpoint (from visual inspection) and from a quantitative viewpoint (using sum of squared differences to evaluate registration accuracy).

As previously stated, in addition to the non-rigid deformation maximizing the similarity between the registered image and the reference image, the deformation must also be realistic and smooth. To constrain the deformation field to be smooth, a penalty term that regularizes the transformation is introduced into the cost function as [106]:

$$C_{smooth}(\mathbf{T}) = \frac{1}{XY} \int_0^X \int_0^Y \left[\left(\frac{\partial^2 \mathbf{T}}{\partial x^2} \right)^2 + \left(\frac{\partial^2 \mathbf{T}}{\partial y^2} \right)^2 + 2 \left(\frac{\partial^2 \mathbf{T}}{\partial x \partial y} \right)^2 \right] dx\, dy \tag{3.15}$$

This regularization is necessary because each pixel in the image is free to move independently. In an extreme case, it is possible that all pixels with one particular intensity in the moving image may map to a single pixel having this same intensity in the reference image, causing the resulting deformation field to be unrealistic [99]. This is one of the primary reasons why non-rigid image registration is considered difficult, as an appropriate balance and compromise must be reached between allowing large amounts of independent movement and ensuring smoothness of the transformation. Also note that this smoothness constraint term is zero for any affine transformations, and therefore only penalizes non-affine deformations [107].

Combining these two metrics, the total cost function is given as:

$$C_{total} = C_{similarity}\left(I'_{n-1}(x,y), I_n(\mathbf{T}(x,y))\right) + \lambda C_{smooth}(\mathbf{T}) \tag{3.16}$$

where n denotes the current image number, I' denotes the registered image, and λ is a weighting coefficient which defines the trade-off between the two competing cost terms. To maximize image similarity after registration, and to minimize sharp warping elements in the transformation $\mathbf{T}$, we desire to minimize C_{total}. In our work, we have defined $C_{similarity}$ to have decreasing value for increasingly similar images (i.e. two identical images have $C_{similarity} = 0$). This, coupled with the desire to minimize sharp warping elements in the transformation $\mathbf{T}$ defined in C_{smooth}, we desire to minimize C_{total} as well.

Similar to the rigid registration method, the non-rigid B-spline registration method also assumes grayscale, single channel images, not multi-channel (multiple component) images. Therefore, we use the same composite gray channel constructed previously to use with this registration method. More specifically, the resulting grayscale image from the rigid registration method is used as the input image to the non-rigid registration method. Then, for each image, a final deformation field based on the gray image is obtained. This deformation field is then used to transform all channels of the image. The combined rigid translation and non-rigid deformation obtained for this grayscale image is used to transform all channels of the multi-channel image.

The choice of λ is not critical for low resolutions of the control point grid, however this term becomes more important for higher resolutions of the control point grid [103]. This is because the B-spline model increases its ability to model more localized deformations with increasing control point density, leading to the need for more regularization.

However, the degree of deformation allowed is not only affected by the choice of λ, but also by the choice of δ_x, δ_y. The resolution of the grid of control points affects how readily $C_{similarity}$ may be minimized. A large, sparse spacing of control points corresponds with a more global non-rigid deformation, which may not allow

$C_{similarity}$ to reach values near zero. Alternatively, a small, dense spacing of control points corresponds with highly local non-rigid deformations and more readily allows $C_{similarity}$ to reach values near zero, but may also encourage more unrealistic deformations [107]. In other words, a coarse control point grid will not be able to model the deformation accurately. At the same time, a control point grid that is too dense will overcompensate for true image differences and noise [108]. Therefore, the choice of both λ and the grid spacing should be dependent on the image noise level, which is associated with the confidence we have in the intensity relationship assumed by our image similarity measure [109]. In our work, we have experimented with various grid spacings, and have found that spacings that work well are highly dependent on image size, the content of these images, and the degree of motion artifacts present throughout the stack of images. As a result, grid spacing values are currently chosen empirically.

Since intravital microscopy data sets consist of entire stacks of images, non-rigid registration is performed on an image-by-image basis. In this case, for the current image (or moving image), the reference image is not simply the prior image in the stack. Instead, the reference image used is the registered or warped prior image. This ensures that each image is warped only once so that images do not undergo additional interpolation from multiple warpings. This is in contrast to the rigid registration method previously described which corrected for translations. In the rigid registration method, the moving or test image was the current image and the static or reference image was the original previous image. A cumulative sum of the incremental translations obtained from rigid registration is then used to register the current image. Using this approach with the non-rigid registration method was shown to produce very poor results. The cumulative sum of incremental deformation fields created unrealistic final deformation fields. This is because the deformation field is not necessarily twice continuously differentiable after the summation operation (the deformation field is not regularized). Therefore, the current image, after it has experienced rigid registration, is registered against the previous image that has

already undergone both rigid followed by non-rigid registration, ensuring that the resulting deformation field is smooth, continuous, and realistic (properly regularized).

3.2.3 Multi-Resolution Approach to Non-Rigid Registration

We further extend our non-rigid registration technique using B-splines to use multiple stages in a multi-resolution fashion to further enhance image registration performance [110]. It has been observed that some regions of the images being registered may benefit from a coarse grid spacing, while other regions may benefit from a fine grid spacing. Therefore, rather than using a single grid spacing for our control points, we use a multi-resolution/multi-level approach in a coarse-to-fine strategy. Non-rigid registration is first performed using a control lattice with a coarse grid spacing to account for slowly changing deformations. Next, a control lattice with a finer grid spacing is used to account for more localized and quickly changing deformations. The registered images resulting from a coarse grid spacing are registered again using a fine grid spacing. Additional non-rigid registration iterations using a control lattice with increasingly finer grid spacings may be performed until the user achieves no further improvement in image registration. We will show in Section 6.5.3 that this multi-resolution approach is able to achieve more accurate matching between a registered image and its reference image.

3.2.4 Correction for Three Dimensional Volumetric Data

Our procedure of registering a series of images on an image-by-image basis follows the premise behind data sets collected in time-series. However, it does not necessarily fully follow the premise behind data sets collected in three dimensions. In particular, our method assumes that the same structures will be in the field of view for the entire series of images. This assumption is correct for time-series data sets, but is incorrect for three dimensional data sets as the focal plane changes throughout the series of images. For this reason, one particular issue is that nuclei, which are

naturally spherical in shape, become cylindrical after non-rigid registration. Here, we modify and improve our non-rigid registration method using B-splines specifically for use with volumetric data.

True three dimensional registration is not feasible in this situation. An entire three dimensional volume is not being registered against a reference three dimensional volume. Instead, the registration occurs on a slice-by-slice basis. Therefore, a particular slice undergoing registration will not have information regarding the entire three dimensional registration available. More specifically, for the registration of each slice, the deformation grids for all slices ahead of the current slice have yet to be computed. At the same time, the deformation grids for all slices behind the current slice have already been computed. Therefore, we modify the smoothness constraint in our registration method:

$$C_{smooth}(\mathbf{T}) = \frac{1}{XYZ'} \int_0^X \int_0^Y \int_0^{Z'} \left[\left(\frac{\partial^2 \mathbf{T}}{\partial x^2} \right)^2 + \left(\frac{\partial^2 \mathbf{T}}{\partial y^2} \right)^2 + \left(\frac{\partial^2 \mathbf{T}}{\partial z^2} \right)^2 + 2 \left(\frac{\partial^2 \mathbf{T}}{\partial x \partial y} \right)^2 + 2 \left(\frac{\partial^2 \mathbf{T}}{\partial x \partial z} \right)^2 + 2 \left(\frac{\partial^2 \mathbf{T}}{\partial y \partial z} \right)^2 \right] dx\, dy \tag{3.17}$$

where Z' is the current depth of the volume that has undergone registration thus far, and will increase by one for each successive slice analyzed. For example, $Z' = 1$ for the first slice in the volume analyzed, and $Z' = Z$ for the last slice in the volume analyzed. For each slice, no deformation grids behind the current slice are modified, yet they are included in the computation of the deformation grid for the current slice. Combining this new smoothness constraint into the overall cost function previously introduced, the new cost function becomes:

$$C_{total} = C_{similarity} \left(I'_{n-1}(x, y), I_n \left(\mathbf{T}(x, y, Z') \right) \right) + \lambda C_{smooth}(\mathbf{T}(x, y, z)) \tag{3.18}$$

This new smoothness constraint ensures that the deformation field is smooth in all three dimensions despite registration being performed on a slice-by-slice basis. Even though the transformation $\mathbf{T}$ is now three dimensional, all three dimensions are in-

cluded only in the computation of the smoothness constraint, while only the two dimensional slice of $\mathbf{T}$ is used in the computation of the similarity measure. We will demonstrate in Section 6.5.4 that this modification to the smoothness constraint for volumes acquired in three dimensions will help retain the true three dimensional structure of cellular objects.

3.3 Summary of Experimental Results

We will demonstrate all aspects of our rigid and non-rigid registration schemes throughout Section 6.4 and Section 6.5. More specifically, we will demonstrate that rigid registration as described in Section 3.1 is able to successfully correct a subset of motion artifacts (ones consisting of global translational motion), and will be shown in Section 6.4 and the beginning of Section 6.5.2. When attempting to correct more complicated motion artifacts, we will demonstrate that the demons algorithm as described in Section 3.2.1 is insufficient and may exacerbate the issue, and will be shown in Section 6.5.1. Instead, we will show that non-rigid registration using B-splines as described in Section 3.2.2 significantly reduces motion artifacts. Results demonstrating the effectiveness, robustness, and versatility of combined rigid and non-rigid registration using B-splines will be shown in Section 6.5.2. For image data sets where motion artifacts are noticeably intensified, we will demonstrate that our multi-resolution approach to non-rigid registration using B-splines as described in Section 3.2.3 successfully mitigates these intense motion artifacts, as shown in Section 6.5.3. Lastly, we improve upon our non-rigid registration method using B-splines particularly for three dimensional volumetric data as described in Section 3.2.4. We will demonstrate in Section 6.5.4 that this improvement, despite further constraining the deformation, is able to sustain a high registration accuracy while also better maintaining the original size and shape of three dimensional cellular structures.

4. 3-D ACTIVE SURFACES

Here, we embark in a new direction and explore native three dimensional image segmentation for use with volumetric data. Active contours and active surfaces are segmentation methods with ongoing development and research. Their application to medical image segmentation and microscopy has been no exception. We will be using an active surface model to effectively identify cellular objects in sequences of microscopy images.

4.1 Introduction to Active Contours and Active Surfaces

Two-dimensional active contour models, also known as snakes, are an image segmentation method that iteratively evolves a curve toward object boundaries by minimizing an energy functional derived from the image being segmented, subject to some constraints. In the classical active contour models, let $C(s) = [x(s), y(s)]^T$, $s \in [0, 1]$ be a parameterized curve in $\mathbb{R}^2$. The energy functional being minimized is [111]:

$$E(C) = \alpha \int_0^1 |C'(s)|^2 \, ds + \beta \int_0^1 |C''(s)|^2 \, ds - \lambda \int_0^1 |\nabla I(C(s))|^2 \, ds \tag{4.1}$$

where α, β, and λ are positive coefficients. The first two terms affect the smoothness of the curve, and are known as the "internal energy." For example, setting $\beta = 0$ will allow the curve to become second-order differentially discontinuous and develop a sharp corner [112]. Meanwhile, the third term attracts the contour toward object edges, and is known as the "external energy." The external energy is defined such that its value decreases near features of interest (in this case, object edges). The problem now becomes finding a curve C that minimizes the energy $E(C)$. By minimizing the

total energy, $E(C)$, the curve is drawn to the maxima of $|\nabla I|$, essentially acting as an edge-detector, while simultaneously maintaining the curve's smoothness.

This framework may be generalized by realizing an edge-detector can be modeled as a positive and strictly decreasing function, g. For example:

$$g\left(|\nabla I(x,y)|\right) = \frac{1}{1+|\nabla G_\sigma(x,y) * I(x,y)|^p},\ p \geq 1 \tag{4.2}$$

where

$$G_\sigma(x,y) = \sigma^{-1/2} e^{-\frac{\left|x^2+y^2\right|}{4\sigma}} \tag{4.3}$$

is the Gaussian function, and $G_\sigma * I(x,y)$ is a smoothed version of the image I via convolution. Therefore, the term $|\nabla I(C(s))|$ may be replaced with $g\left(|\nabla I(C(s)|\right)$.

However, there are some noteworthy pitfalls of this framework. For instance, when multiple objects are desired to be segmented yet the initial contour is a single contour surrounding all of the objects, the objects will not be individually segmented [113]. Instead, the likely result is for the curve to evolve to the convex hull of all of the objects. However, with the implicit representation of the curve using level-sets, automatic topology changes may occur, partially alleviating the precision necessary for an accurate initialization curve.

An additional pitfall of this framework is the dependence on the image gradient to properly detect object edges. As discussed in Section 1.2, object edges in our image data are poorly defined. Therefore, using the image gradient to stop curve evolution will likely give poor segmentation results. Instead, we will be using the framework proposed in [114] for our active surface model.

4.2 Our Active Surface Model

Before we employ our active surfaces method, we first pre-process our image volume to mitigate the lack of edge detail. As previously mentioned, the z-axis is sampled approximately four times more coarsely than the sampling along the x-axis and y-axis.

This is due to the current limitations of optical microscopy image acquisition systems. Therefore, to be able to render the volume with accurate proportions, we first use cubic interpolation on the volume across the z-axis using a factor of four. This causes our new voxels to be cubic rather than rectangular. Next, we use three dimensional morphological filtering on the volume to increase edge detail and increase texture homogeneity within cellular objects. Specifically, we use a morphological opening followed by a morphological closing [74], both using a spherical flat structuring element with radius r. The combined morphological opening and closing operations suppress noise and will allow the active surface to converge to the appropriate edges of nuclei where image intensity is the greatest.

The principals of our active surface method are founded in the work proposed in [114]. Extended to three dimensions, the energy functional, or "fitting term," is most commonly defined for a surface S as:

$$\begin{aligned} E(S) = \lambda_{in} \int_{inside(S)} |V(x,y,z) - \mu_{in}|^2 \, dx\, dy\, dz \\ + \lambda_{out} \int_{outside(S)} |V(x,y,z) - \mu_{out}|^2 \, dx\, dy\, dz + \alpha \, \text{Length}(S) \end{aligned} \tag{4.4}$$

where V is the image volume being segmented, μ_{in} is the sample mean intensity of V enclosed by S, μ_{out} is the sample mean intensity of V outside S, and λ_{in}, λ_{out}, and α are weighting coefficients all greater than zero. Placing the surface S on object boundaries will minimize the first two terms of $E(S)$. The third term of $E(S)$ is a regularizing term. Combining the sum of these terms, we desire to minimize this total energy functional, $E(S)$. For implementation purposes, this energy functional can be formulated implicitly using level-set curves. By replacing the unknown variable S with the unknown variable ϕ, and by introducing the Heaviside function:

$$H(\phi) = \begin{cases} 1 & \text{if } \phi \geq 0 \\ 0 & \text{if } \phi < 0 \end{cases} \tag{4.5}$$

the energy functional can be rewritten as:

$$\begin{aligned} E(S) = \lambda_{in} \int_{\Omega} |V(x,y,z) - \mu_{in}|^2 H(\phi(x,y,z))\, dx\, dy\, dz \\ + \lambda_{out} \int_{\Omega} |V(x,y,z) - \mu_{out}|^2 (1 - H(\phi(x,y,z)))\, dx\, dy\, dz \\ + \alpha \int_{\Omega} \delta(\phi(x,y,z)) |\nabla \phi(x,y,z))|\, dx\, dy\, dz \end{aligned} \tag{4.6}$$

where Ω is the domain of the image volume (a subset of $\mathbb{R}^3$), and $\delta(\phi)$ is the Dirac delta function defined as the derivative of the Heaviside function. The former surface S is now represented as the zero level-set surface of ϕ. Also note that $\phi > 0$ for regions inside of or enclosed by the surface S, and $\phi < 0$ for regions outside of or exterior to the surface S. Further, the sample means μ_{in} and μ_{out} can be expressed as a function of ϕ:

$$\begin{aligned} \mu_{in}(\phi) &= \frac{\int_{\Omega} V(x,y,z) H(\phi(x,y,z))\, dx\, dy\, dz}{\int_{\Omega} H(\phi(x,y,z))\, dx\, dy\, dz} \\ \mu_{out}(\phi) &= \frac{\int_{\Omega} V(x,y,z)(1 - H(\phi(x,y,z)))\, dx\, dy\, dz}{\int_{\Omega} (1 - H(\phi(x,y,z)))\, dx\, dy\, dz} \end{aligned} \tag{4.7}$$

Alternatively, and perhaps more intuitively, μ_{in} and μ_{out} are simply:

$$\begin{aligned} \mu_{in}(\phi) &= \text{mean}(V) \text{ in } \phi \geq 0 \\ \mu_{out}(\phi) &= \text{mean}(V) \text{ in } \phi < 0 \end{aligned} \tag{4.8}$$

By parameterizing by an artificial time $t \geq 0$, the associated partial differential equation (Euler-Lagrange equation) for ϕ is:

$$\frac{\partial \phi}{\partial t} = \delta(\phi) \left[\lambda_{out}(V - \mu_{out})^2 - \lambda_{in}(V - \mu_{in})^2 + \alpha \,\text{div}\left(\frac{\nabla \phi}{|\nabla \phi|} \right) \right] \tag{4.9}$$

By using a numerical approximation, this partial differential equation may be solved iteratively using [115]:

$$\phi^{n+1} = \phi^n + \Delta t \left[\lambda_{out}(V - \mu_{out}(\phi^n))^2 - \lambda_{in}(V - \mu_{in}(\phi^n))^2 + \alpha \,\text{div}\left(\frac{\nabla \phi}{|\nabla \phi|} \right) \right] \tag{4.10}$$

where n is the iteration number and Δt is an artificial time step. Choosing α to be large compared to λ is necessary to filter high frequency noise. Likewise, choosing λ to be large compared to α is necessary to detect objects with finer detail [116].

Computation of the curvature $\kappa = \text{div}\left(\frac{\nabla\phi}{|\nabla\phi|}\right)$ is straight-forward in two dimensions. However, in three dimensions, several definitions of curvature exist. Here, we use mean curvature [117]:

$$\kappa = \frac{\left\{\begin{array}{r} \phi_x^2(\phi_{yy}+\phi_{zz}) + \phi_y^2(\phi_{xx}+\phi_{zz}) + \phi_z^2(\phi_{xx}+\phi_{yy}) \\ -2\left(\phi_x\phi_y\phi_{xy} + \phi_x\phi_z\phi_{xz} + \phi_y\phi_z\phi_{yz}\right) \end{array}\right\}}{\left(\phi_x^2+\phi_y^2+\phi_z^2\right)^{3/2}} \tag{4.11}$$

This implicit representation of the active surface using level-sets allows the surface to split and merge, permitting the segmentation of an arbitrary number of disjoint objects from an arbitrary initialization [7]. Otherwise, if the active surface was defined explicitly using a parametric representation, the number of objects to be segmented in the volume would be required to be known in the initialization.

The active surface is deformed iteratively until convergence. After each iteration, as a regularization step, ϕ is reinitialized to the signed distance function to the zero-level surface (the level-set where $\phi = 0$). After the active surface has reached a stable solution, a final post-processing step is executed. Since nuclei are desired to be segmented as solid objects without any holes (i.e. nuclei are not hollow), we use a morphological fill operation on our final surface. This will eliminate any holes contained within segmented nuclei.

Active contours have previously been extended to three dimensions, using both traditional models [7] and improved or modified models [118, 119] incorporating new external forces or initialization procedures. However, the simplicity of our three dimensional model suits our data set well. Readers may also note that our energy functional lacks a term incorporating the area/volume enclosed by the curve/surface. However, we do not want to favor large nor small nuclei based on the volume enclosed

by each of the surfaces. Objects in the image volume may have a wide variety of sizes, and one particular size should not be penalized or favored over another.

Many alternative energy functionals have been developed and explored [120–122]. However, these methods are much more sensitive to initialization. Energy functionals based on global statistics will be much more robust to curve/surface initialization [123]. We do not have the luxury of advanced topology information regarding our image data. Additionally, extensions to active contours for use with multi-channel or multi-color images [116] is not necessarily beneficial, as we generally do not want to segment all objects in the volume but perhaps just a specific type of object (such as only nuclei and not vasculature). Likewise, a multi-phase extension to active contours [124] to segment more than two regions is not necessarily beneficial, as all objects desired to be segmented within the volume will have the same characteristics (such as all nuclei having the same intensity statistics). As a result, we use a simplistic initialization approach, as the number and size of each cellular object to be segmented is unknown. Therefore, our simplified energy functional suits the data well.

In summary, the fundamental steps of our three dimensional active surface segmentation method are [114]:

1. Interpolate the image volume along the z-axis so that voxels have the same dimension along all three axes.

2. Use morphological filtering to suppress noise and enhance edge detail as preprocessing.

3. Initialize ϕ^0. Set $n = 0$.

4. Compute $\mu_{in}(\phi^n)$ and $\mu_{out}(\phi^n)$ using (4.7) or (4.8).

5. Compute κ using (4.11).

6. Compute ϕ^{n+1} using (4.10).

7. Reinitialize ϕ^{n+1} to the signed distance function to the curve/surface (the level-set where $\phi = 0$).

8. Check whether the curve/surface has converged to a stable solution. If not, set $n \leftarrow n + 1$ and go to Step 4.

9. Use morphological fill operation as post-processing.

4.3 Summary of Experimental Results

Before the use of this three dimensional segmentation method, it is assumed that the data are already aligned or has been aligned/stabilized via the use of image registration techniques as described in the previous chapter [125], particularly Section 3.2.4 pertaining to volumetric data.

We will demonstrate this three dimensional active surface segmentation method in Section 6.6. Results are best rendered in three dimensions using visualization software such as Voxx [126]. However, snapshots of a three dimensional video rendering does not provide an accurate and proportional two dimensional projection. Therefore, instead we show example slices from the xy, yz, and xz planes.

We will see in all three orthogonal planes that nuclei are segmented generally with a circular shape, indicating that the active surfaces method has successfully segmented nuclei in three dimensions. We will also compare these results from this native three dimensional segmentation method with our proposed segmentation method performing analysis slice-by-slice as described in Chapter 2. This method was a pseudo-three dimensional segmentation method tasked with the same objective. When the series of segmentation results from this method is concatenated along the z-axis to form a three dimensional volume, we will see that results are not necessarily realistic and that a true native three dimensional segmentation method is necessary for volumetric data.

5. VALIDATION AND GROUND TRUTH DATA

Objective evaluation of our segmentation and registration results proves to be difficult due to the lack of ground truth data, for which the true shape and position of each object in each image is known. In fact, ground truth is impossible to obtain in intravital microscopy, since both the shape and position of an object are fluid in living animals, and are inevitably altered in the process of isolating and fixing tissues. Thus, to the degree that the concept of a single "true" structure is meaningful, it is unknown and unknowable. However, we can make the assumption that shapes of structures remain relatively constant over time, and seek to reduce changes.

As a substitute for ground truth data, results from an automated segmentation or registration method are often compared to results obtained from a human expert examiner. Although results obtained from an expert clinician may be considered to be gold-standard data, one notable issue with this method is the inherent inter- and intra-operator variability [100]. The same task will be performed differently upon multiple trials by the same examiner, causing intra-operator variability. In addition, the same task will be performed differently by different examiners, causing inter-operator variability.

5.1 Segmentation Validation

An approach to aid in the validation of our segmentation results is as follows: A new data set for a particular specimen was acquired. After this data set was collected, the specimen was physically flipped over, and the data acquisition was performed again. Ideally, the second data acquisition should be identical to the first acquisition with the exception of being mirrored and in reverse order. However, image contrast decreases with increasing tissue depth. Therefore, low contrast images

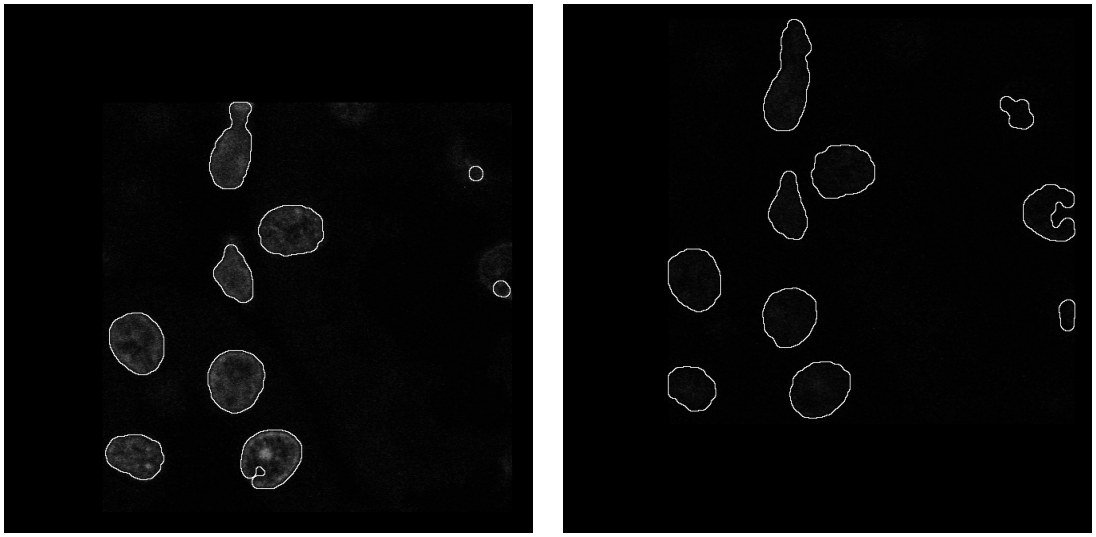

(a) Segmentation from forward acquisition (b) Segmentation from reverse acquisition

Fig. 5.1.: Example segmentation validation results

corresponding to large tissue depth from the first acquisition can now be compared against equivalent high contrast images corresponding to small tissue depth from the second acquisition. Segmentation performance of low contrast images can now be compared with and validated against equivalent high contrast images. This process of flipping the specimen and reverse acquisition is only performed for validation and not performed in the collection of all data sets.

Example results using this segmentation validation technique are shown in Figure 5.1. One output image corresponds to the processing of an input image with high contrast, where segmentation is considered to be not as difficult. The other output image corresponds to the processing of an input image with low contrast, where segmentation is considered to be more difficult. With segmentation boundaries clearly outlined, it is shown that both output images have similar segmentation results. Therefore, the effectiveness of our proposed method is promising for data sets containing a wide range of image contrast. However, this validation process is not a substitute for ground truth data, as determining which of the two segmentation results is considered more desirable is still subjective.

5.2 Registration Validation

As already described, evaluating the accuracy of registration results proves challenging with the lack of ground truth data. A common approach to evaluate registration performance is to manually identify landmarks independently of the registration and to measure how well they are aligned after registration [127]. However, this may be insufficient as errors in image regions located far away from selected landmarks will not be measured. Another common approach is to perform registration validation using simulated image data (phantom data), whereby the deformation is user-specified. However, this is not necessarily appropriate, especially if the deformation model is the same for the simulated image data as it is for the registration method [128]. This validation procedure would only validate the optimization method, and would demonstrate the invertibility of the deformation [100]. Furthermore, a simulated deformation may not necessarily emulate a physically plausible and biologically realistic deformation in a living animal [129]. Alternatively, if the registration is a component of an integrated image analysis system that includes other image processing techniques such as segmentation, registration performance can be indirectly measured using segmentation performance [130]. Other authors exert a bold opinion whereby finding or creating a perfect measure of registration accuracy is paradoxical [66]. If such measures existed, then they would be used in registration methods, and such methods would outperform all other registration methods. Therefore, registration error cannot be quantified with absolute certainty.

We will be employing the use of both visual (or qualitative) assessments and quantitative measurements to evaluate registration accuracy. Qualitative assessments and subjective evaluations of our registration results will be presented in the form of overlay images, maximum projection images, and line scan projection images. Here, we will also describe a means based on block motion estimation by which a more objective and quantitative evaluation and validation of our registration results is performed.

Although block motion estimation does not lend itself well to image registration directly, we will use this method in an attempt to objectively gauge the performance of our non-rigid B-spline registration method [131]. Block motion estimation is an integral component of video coding and compression, and has the strong ability to identify localized motion patterns from one image to the next, and also readily enables the visualization of this localized motion. However, even though this method is able to identify and visualize these highly local motion patterns, a consequence of dividing the image into equally sized blocks is that it does not provide an easy and obvious way to correct these motions and produce a viable and realistically registered image. Traditionally, following block motion estimation, a motion compensated image is created by displacing each block in the image by its associated motion vector. This may increase the similarity between the motion compensated image and the original image according to some defined cost metric. However, the motion compensated image has obvious block artifacts, creating an unrealistic image. However, since block motion estimation allows for easy visualization, we can objectively compare the quantity and angle of motion vectors before and after non-rigid registration.

Block motion estimation has been used with video coding for decades. The overall idea is that block motion estimation provides localized information about direction and magnitude of motion throughout each image in a data set. The method for block motion estimation is well-known [132] and proceeds as follows: The current image is divided into a matrix of equally sized blocks of pixels. Each block is then compared with its corresponding equally sized block and its adjacent neighbors in the previous image. The block in the previous image that is most similar to the block in the current image creates a motion vector that predicts the movement of this block from one location in the previous image to its new location in the current image. A motion vector is computed for each block in the matrix for the entire image. The search area of adjacent neighboring blocks in the previous image is constrained to p pixels in all four directions, and will create a $(2p+1) \times (2p+1)$ search window. A larger value p

is necessary to correctly predict larger motion, but at the same time, also increases computational complexity.

Here, we specify $p = 15$ to create a 31×31 search window, and a $N \times N$ block size. Searching for the maximum similarity between two blocks is determined by minimizing a cost function. Here, we specify mean squared error (MSE) as our cost function:

$$MSE = \frac{1}{N^2} \sum_{i=0}^{N-1} \sum_{j=0}^{N-1} (C(i,j) - R(i,j))^2 \tag{5.1}$$

where N is our chosen block size, and $C(i,j)$ and $R(i,j)$ are the pixels being compared in the current and reference blocks, respectively. Several methods have been developed to reduce the computational complexity of this motion estimation process. However, we are currently more concerned with accuracy and correctness of our results rather than computational complexity. Therefore, we only utilize the exhaustive search, or full search, method. This method computes the cost function for every block in the search window, requiring $(2p+1)^2$ comparisons with blocks having N^2 pixels. Thus, it also finds the best possible match.

6. EXPERIMENTAL RESULTS

6.1 Integrated Segmentation and Registration

We demonstrate our proposed technique as described in Chapter 2 using two data sets, one consisting of a three dimensional volume of nuclei from kidney tissue and a second consisting of a time-series of vasculature from the kidney of a living rat. In the data set consisting of nuclei from kidney tissue, given any particular image, some nuclei appear with significantly increased intensity. This is expected, as cells that are currently in the middle of the focal plane will appear with more intensity, while cells that are on the edge of the focal plane will appear with less intensity. This effect is caused by the dye concentrating within the middle of the nuclei creating a non-homogeneous distribution. Naturally, selecting which cells are relevant in any given image is subjective. Since there does not appear to be significant motion between images in this data set, registration techniques may not need to be utilized. Regarding the data set consisting of vasculature from the kidney of a living rat, movement between images is much more significant due to specimen motion during acquisition. Therefore, registration is needed to correct these movements between images.

Registration results for this second data set are shown in Figure 6.1. The horizontal and vertical displacements appear with few large spikes. This suggests that the majority of the offsets are concentrated in just a few images. In fact, the mean squared error metric shows a very distinct peak in the middle of the image sequence that indicates a significant motion artifact. This can be used as an indicator to possibly evaluate and analyze the corresponding images in the data set manually.

As previously described, we also evaluated the effectiveness of using mutual information as a registration metric. However, results were poorer than those obtained using the mean squared error metric. Figure 6.2 shows these registration results and

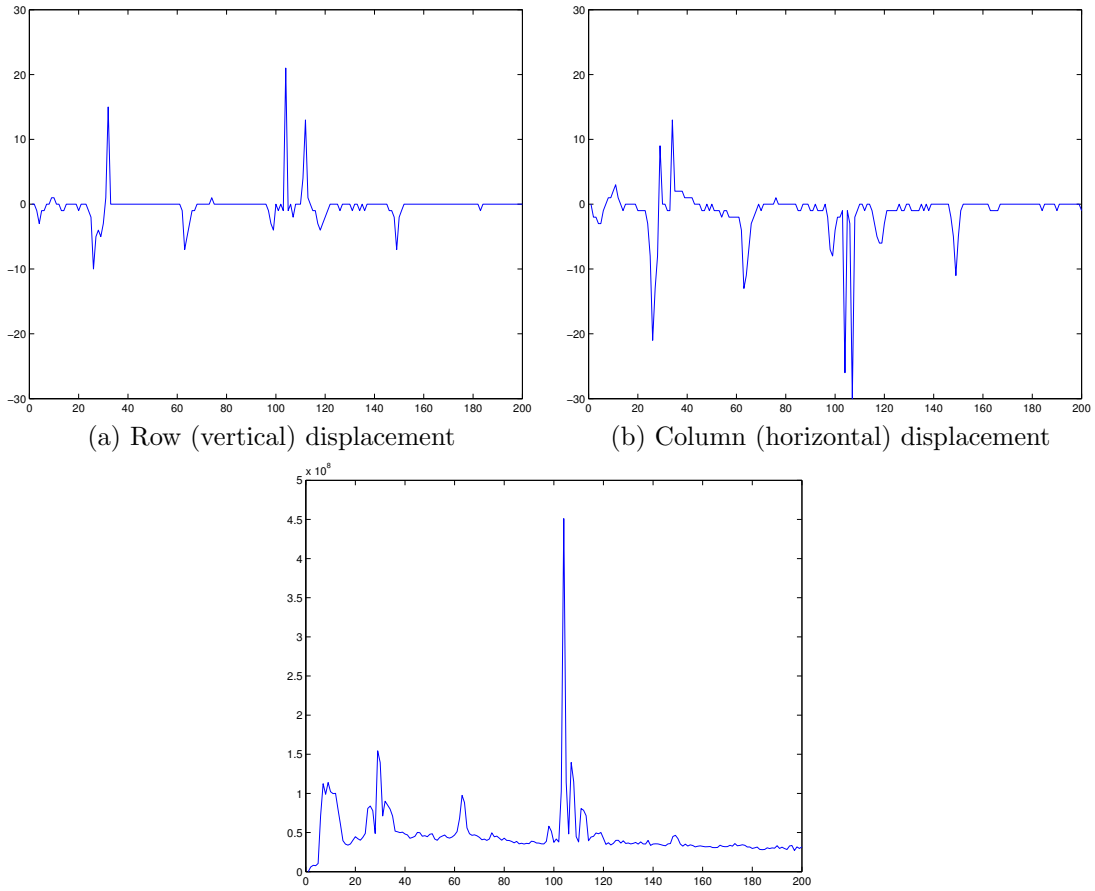

(a) Row (vertical) displacement

(b) Column (horizontal) displacement

(c) Mean squared error metric

Fig. 6.1.: Registration results from rat kidney vasculature data set using mean squared error metric

can be compared against the results from Figure 6.1. Unlike the mean squared error metric, when there is significant motion between images, the mutual information metric does not produce large peaks in the metric value. Additionally, the mutual information metric values contain more variation than the mean squared error metric values.

Authors in [133] have further explored the mutual information metric. It has been extensively shown that metrics based on the evaluation of mutual information are well suited for overcoming the difficulties of multi-modality registration, where images to be registered have been acquired using different imaging techniques such that pixel intensities for the same objects are not correlated across images [134, 135]. Since our

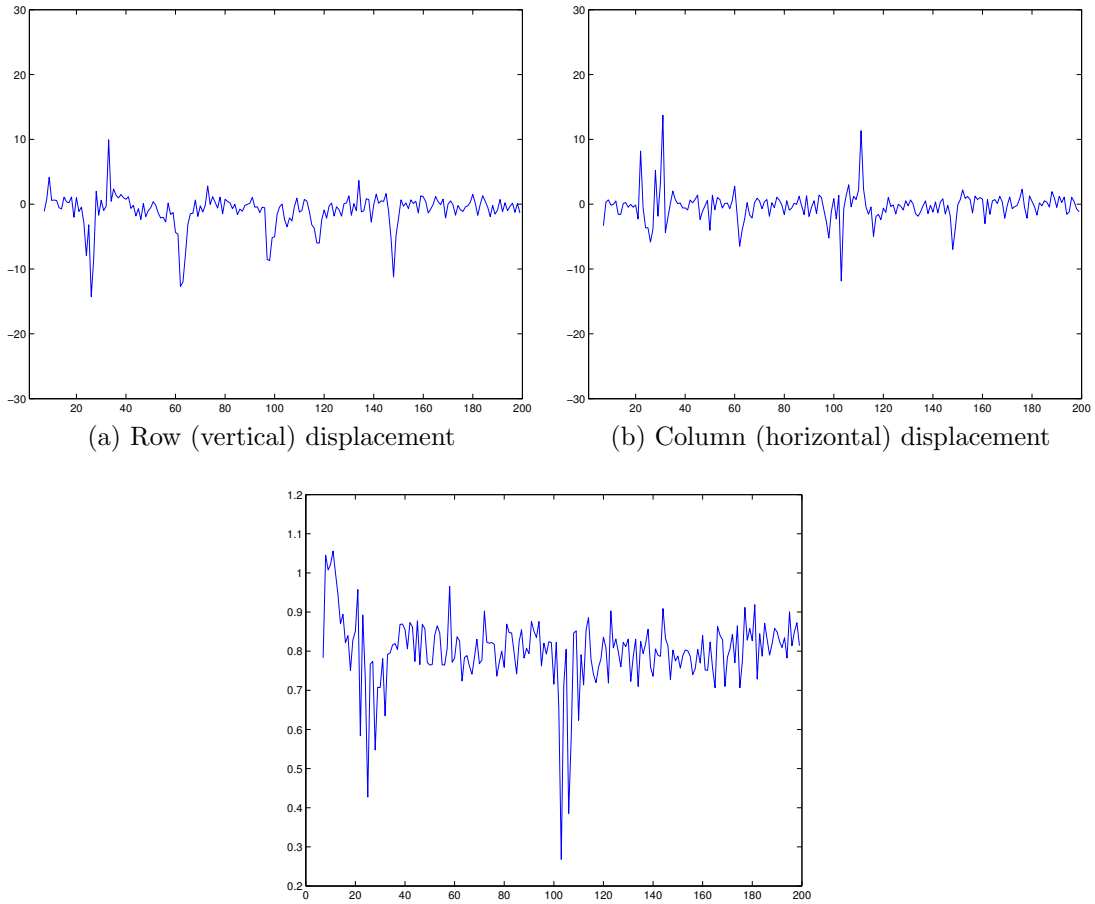

(a) Row (vertical) displacement

(b) Column (horizontal) displacement

(c) Mutual information metric

Fig. 6.2.: Registration results from rat kidney vasculature data set using mutual information metric

data sets are all single modality, having mutual information perform poorly is not surprising.

After each data set was denoised, filtered, and registered, it was thresholded via K-means. As shown in Figure 6.3 for the rat kidney vasculature data set, the threshold changes drastically only once, when there is significant motion approximately halfway through the image sequence. In contrast, for the rat kidney nuclei data set, images near the beginning and end of the sequence are too dark for the K-means procedure to segment into two groups. This is shown by the threshold attaining extreme values.

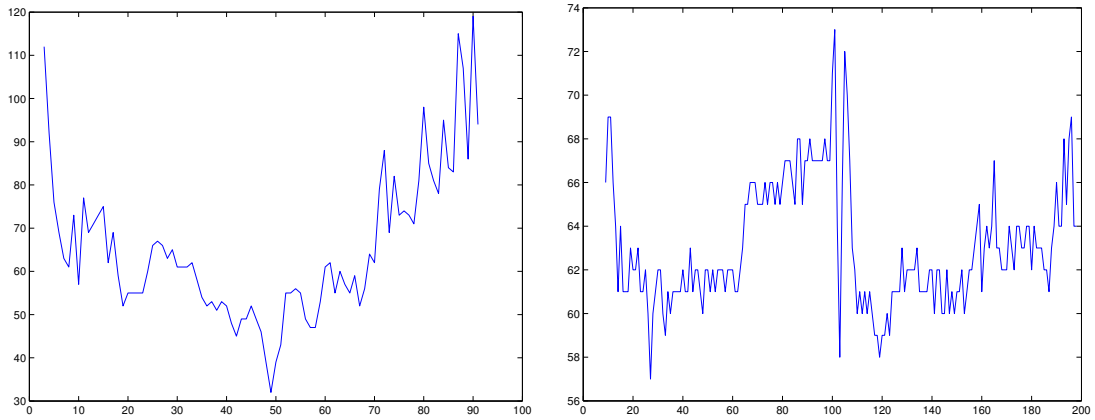

(a) Rat kidney nuclei data set (b) Rat kidney vasculature data set

Fig. 6.3.: K-means threshold vs. image number

A confidence metric may be developed so that the user may be warned for cases where K-means has difficulty identifying two distinct groups of objects in a given image.

Representative images showing the performance of our entire system for the nuclei and vasculature data sets are given in Figure 6.4. As can be seen in the results for the first data set, nuclei with the greatest intensity are retained, while those with the lowest intensity are eliminated in the output. Similarly, in the results for the second data set, structures with the greatest intensity are retained while those with the lowest intensity are eliminated in the output.

However, when used for the analysis of particular multi-channel data sets, our proposed approach encounters some difficulty. Ideally, the desired structures to be segmented will be predominately contained within one of the three primary color channels. For example, vasculature is often desired to be segmented and is labeled using red. Then, this respective color component is extracted and only this color component is analyzed using the proposed approach, just as the single channel or grayscale data sets were analyzed. However, structures to be segmented are not necessarily fully contained within one of the primary color channels. An example image from a multi-channel data set consisting of a volume of kidney tissue from a living rat is shown in Figure 6.5. In this data set, the vasculature is shown in

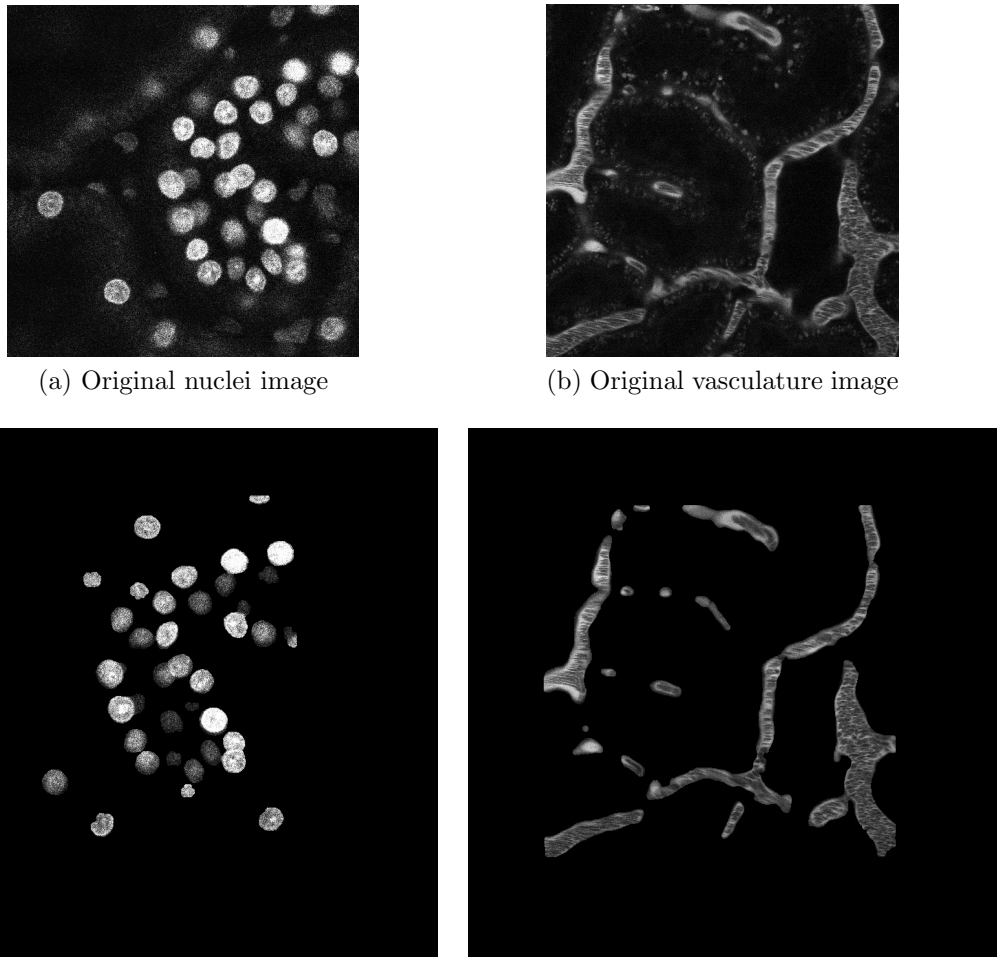

(a) Original nuclei image

(b) Original vasculature image

(c) Final segmented nuclei result

(d) Final segmented vasculature result

Fig. 6.4.: Example results for rat kidney nuclei and vasculature data sets

red, while at the same time, many other unwanted structures are shown in yellow which also contains a large red component. Therefore, this data set must undergo additional pre-processing due to the image set characteristics and desired objects to be segmented. This pre-processing is called *green component clamping*, and is described in the following section [136].

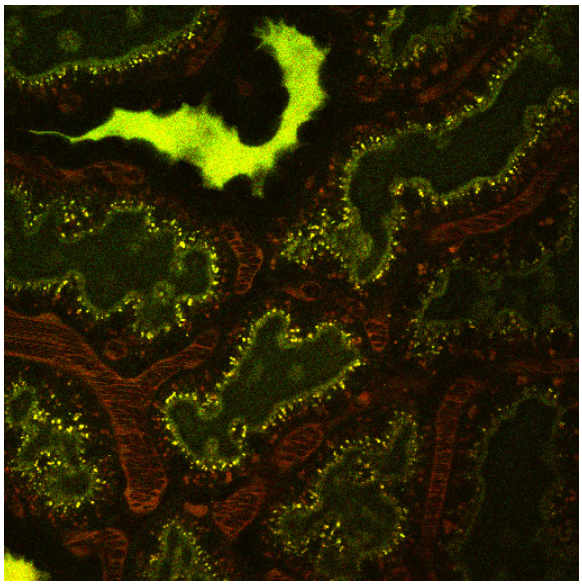

Fig. 6.5.: Example image of multi-channel data set requiring pre-processing

6.2 Green Component Clamping

The images in the aforementioned data set contain many yellow structures, which we do not want to segment. Endosomes and tubular lumen have a large red component. The yellow appearance is not due to the cellular objects truly being yellow, but is a result of the color palette used in assigning color to each of the three channels of the multiphoton microscope. As described in Section 1.2, channel isolation is imperfect, as channel saturation and bleeding often occurs. This creates an undesired side-effect causing these yellow structures to contain a large red component. Therefore, simply using the red component of these images will result in the segmentation of unwanted objects in addition to the vasculature. Therefore, to reduce the visibility of yellow structures, a new image is constructed by the following:

$$\tilde{I}_r(m,n) = \begin{cases} 0 & \text{if } \dfrac{I_r(m,n)}{I_g(m,n)} < \dfrac{1}{\alpha} \\ I_r(m,n) & \text{else} \end{cases} \tag{6.1}$$

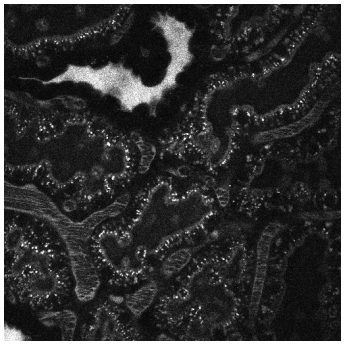

(a) Red component

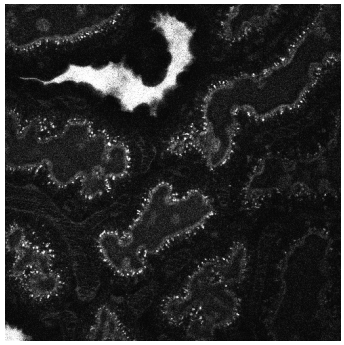

(b) Green component

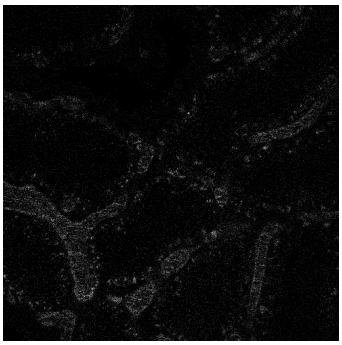

(c) New green-clamped image

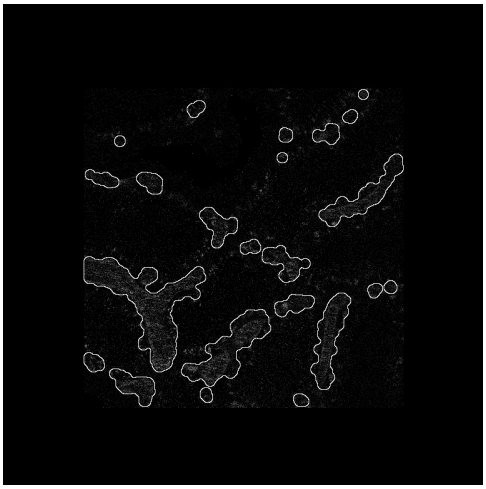

(d) Output image

Fig. 6.6.: Example analysis from multi-channel data set after *green component clamping*

where I_r and I_g are the red and green components, respectively, of the current image in the stack being analyzed, and α is a constant greater than one. Selecting $\alpha = 3$ has experimentally shown to produce acceptable results. Then, $\tilde{I}_r$ is analyzed using the proposed approach. The effects and results of this pre-processing can be seen in Figure 6.6.

6.3 Segmentation Results without Non-Rigid Registration

With well-behaved data sets, the proposed method effectively segments the desired structures from the series of images. To demonstrate intermediate results from every block in Figure 2.1, the output from each block from the analysis of an example image from a volumetric data set collected from the liver of a living rat is shown in Figure 6.7. However, many motion artifacts due to respiration and heartbeat remain. Therefore, results utilizing both rigid and non-rigid registration will be described in depth and in vigorous detail in the following sections.

6.4 Rigid Registration

As previously described, motion artifacts can be considered to consist of two components: a rigid component in which sequential images exhibit a translational offset from one another, and a non-rigid component which features non-linear distortions within each image. Many software applications have been developed for addressing global linear and orthogonal registration of microscopy images (e.g. Metamorph and various plug-ins for ImageJ), since this has been an ongoing problem in microscopy of living cells in culture. We first show an example of a data set in which motion artifacts consist primarily of rigid translations.

Figure 6.8(a) shows one of a series of images collected over time from the kidney of a living rat, following intravenous injection with fluorescent dextran. This is one of the two data sets previously used for demonstration of our proposed segmentation method. The motion of the sample is apparent in Figure 6.8(b), which shows a maximum projection of the entire time-series, in which the motion results in a smearing in the images of the renal capillaries. The significant reduction of motion artifacts is shown in the projection of this time-series after rigid registration, shown in Figure 6.8(c). The effective elimination of specimen translation by the registration technique is also shown in Figure 6.8(d)-(e), which shows sequences of single lines from the images before and after registration, respectively. In these images, the

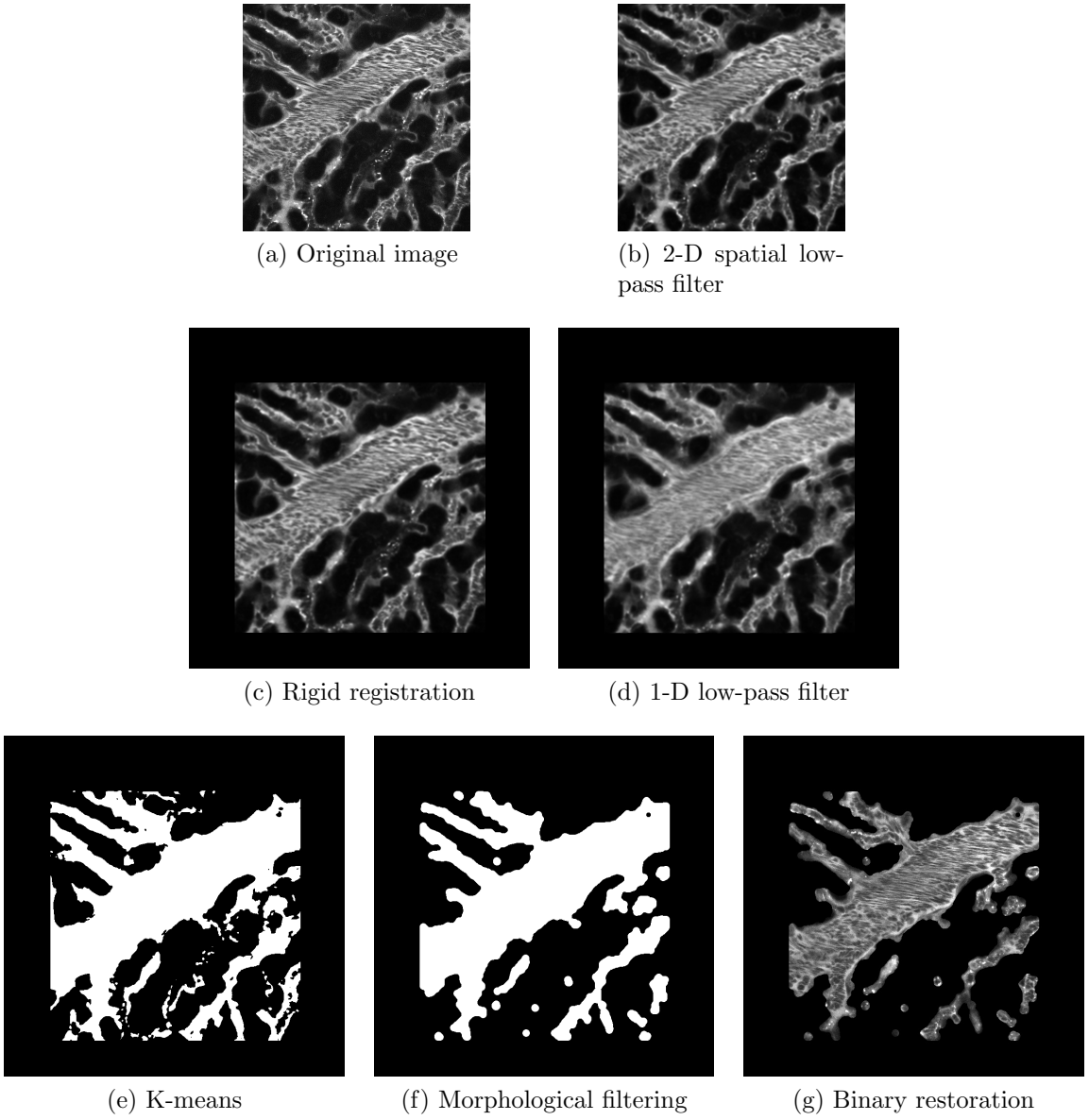

(a) Original image

(b) 2-D spatial low-pass filter

(c) Rigid registration

(d) 1-D low-pass filter

(e) K-means

(f) Morphological filtering

(g) Binary restoration

Fig. 6.7.: Example of intermediate output images

intensity profile of each line is arrayed horizontally and the time sequence arrayed vertically.

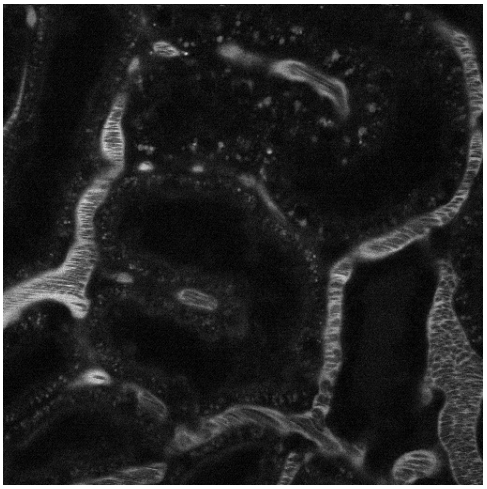

(a) Example image from kidney vascular flow data set

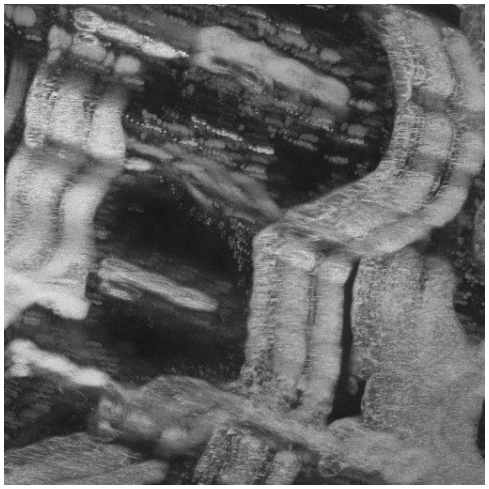

(b) Maximum projection of entire series of images before rigid registration

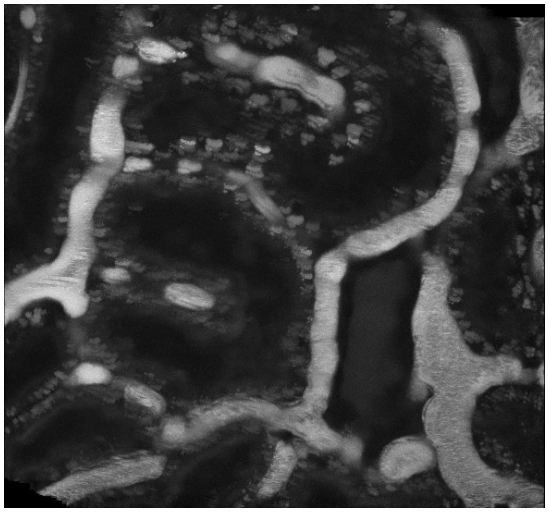

(c) Maximum projection of entire series of images after rigid registration

(d) Line scan projection image before rigid registration

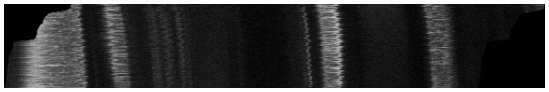

(e) Line scan projection image after rigid registration

Fig. 6.8.: Rigid registration of kidney vasculature. Image field before registration is 205 μm wide. Image field after registration is wider because the field has shifted over the time of collection to include more area. Image sequence contains 200 frames.

6.5 Non-Rigid Registration

However, as previously discussed, intravital microscopy introduces a completely different type of registration problem in which there is intrascene motion resulting

from motion in the sample during collection of an individual image. We will now demonstrate the effectiveness of our non-rigid registration technique on several data sets consisting of images of the lung, kidney, and salivary gland collected in living rodents.

6.5.1 Demons Algorithm

We demonstrate our first non-rigid registration method, the demons algorithm, on a series of images collected from the liver of a living rat, which contains severe non-linear motion artifacts. A representative original image from this data set and the corresponding registered image are shown in Figure 6.9. The motion artifacts are most apparent in the red channel showing the blood flow, and are visible as horizontal banding patterns. These horizontal warping patterns are due to the scan direction of the multiphoton microscope during image acquisition. During one horizontal pass of the scanner, the specimen is in one particular position. During the subsequent horizontal pass of the scanner directly below the previous pass, the specimen has moved and is in a different position, creating the warping distortion. Additionally, the demons algorithm operates on single channel images, not multi-channel images. Therefore, a particular channel must be selected to perform registration on. The predominance of the irregular blood flow within the vascular structures makes the red channel a poor choice to use for registration. The green channel consists mostly of background fluorescence noise with very few structures. Therefore, the green channel is also a poor choice to use for registration. Since the blue channel consists of no crosstalk from the other two channels as described in the introduction, and also consists predominantly of clearly visible nuclei structures, using this channel is a logical choice to perform registration. Thus, the demons registration method was performed on the blue channel of the data set. For each image, a final deformation field was obtained. This deformation field was then used to transform all three channels of the image.

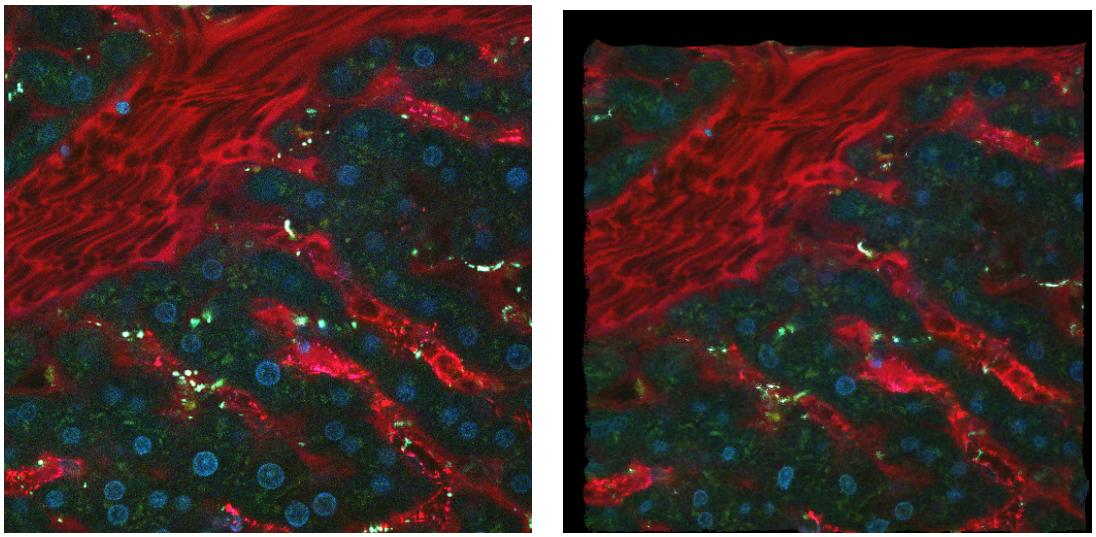

(a) Original image (b) Registered image

Fig. 6.9.: Example image demonstrating the demons registration algorithm

We choose to smooth the deformation field using a Gaussian filter with variance $\sigma^2 = 2.0$. The results from the demons registration method shown in Figure 6.9 need significant improvement. The motion artifacts easily visible within the vascular structures in the red channel are exaggerated rather than corrected. In the blue channel, nuclei are no longer round as expected. Instead, nuclei become oblong and transform into other irregular shapes. These issues persisted across all images registered in the stack. These consistently poor results led to the use of B-splines for non-rigid registration.

6.5.2 Non-Rigid Registration Using B-Splines

We now introduce an example three-channel data set containing severe non-linear motion artifacts. This data set is a three dimensional volume collected from the kidney of a living rat. We have depicted the results from a sequence of two consecutive images from this data set to demonstrate our non-rigid registration method using B-splines. By progressing from one image to the next, significant motion artifacts are

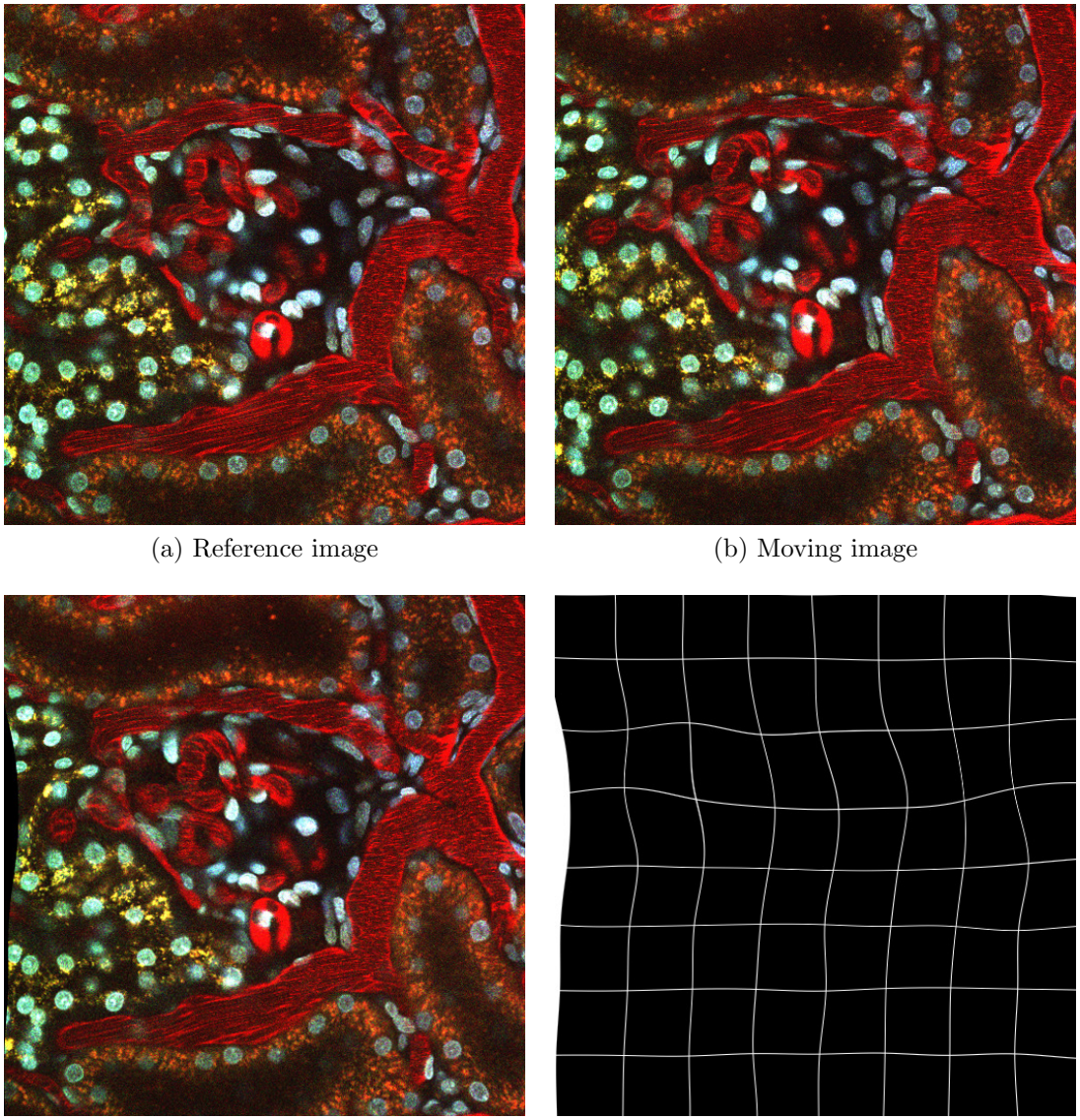

(a) Reference image

(b) Moving image

(c) Registered image

(d) Deformation field

Fig. 6.10.: Non-rigid registration results using B-splines from example data set

visible as horizontally banded regions of the scene are warped to the upper-left. In the subsequent image, the objects are restored to their unwarped original locations.

Figure 6.10 shows the results from B-spline registration along with the deformation grid corresponding to the warping of the moving image to the reference image. These results were obtained by performing registration using $\lambda = 0.01$ and a B-spline control point grid spacing of $\delta_x = \delta_y = 64$ pixels, and using a limited memory Broyden-

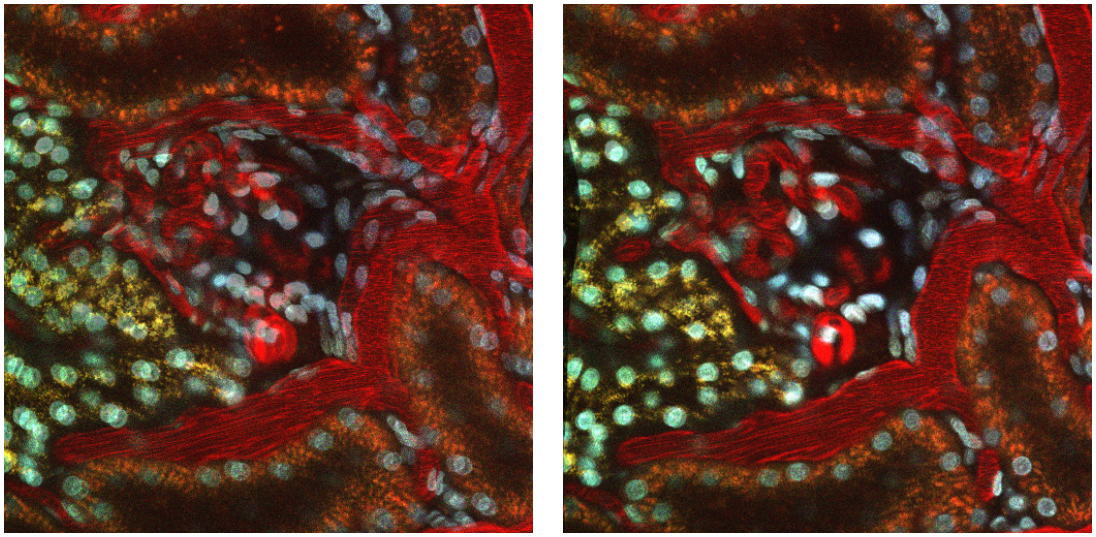

(a) Unregistered images (b) Registered images

Fig. 6.11.: Overlay of consecutive images from example data set

Fletcher-Goldfarb-Shanno (L-BFGS) optimizer to determine the final B-spline control points.

A subjective evaluation of the registration results is performed by overlaying consecutive unregistered images, and comparing this composite overlay image with that for the corresponding consecutive registered images. This comparison is shown in Figure 6.11. Ghosting artifacts are easily visible in the unregistered overlay image, due to significant misalignment of objects. However, this ghosting is vastly reduced in the registered overlay image. Therefore, this visual inspection of the registration results confirms that the motion artifacts have largely been corrected.

As an additional way to evaluate our non-rigid registration results, we compared these results to those from using the demons algorithm. The results from using the demons algorithm for the same representative image are shown in Figure 6.12. As can be seen, these results are vastly unrealistic. From visual inspection and similar to the results in Figure 6.9, motion artifacts within the vascular structures shown in red are exaggerated rather than corrected. Nuclei shown in blue become oblong, irregular, and malformed rather than round as expected. Therefore, we conclude that non-rigid

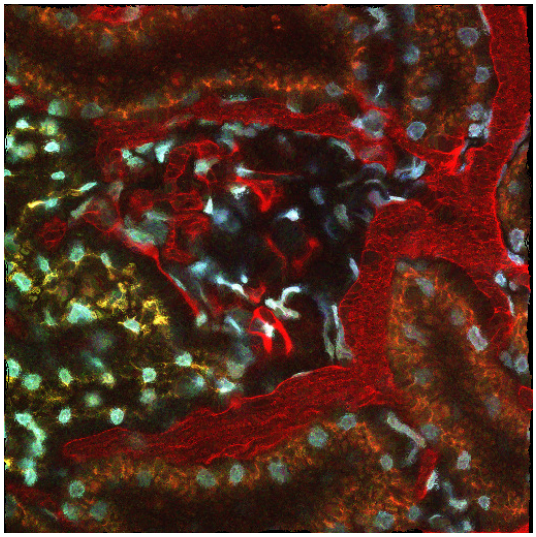

Fig. 6.12.: Comparison of non-rigid registration results using the demons algorithm

B-spline registration improves upon the demons algorithm for intravital microscopy images.

As a more objective evaluation of registration results, computing histograms of angles for motion vectors with non-zero magnitudes attempts to identify any distinct motion patterns within the motion vector field. These histograms, corresponding with the unregistered images, are created with 36 bins. Furthermore, these histograms of motion vector angles are weighted by motion vector magnitude, and are shown in Figure 6.13. As can be seen, the first image (whose histogram is shown in Figure 6.13(a)) has a distinct motion to the upper-left, while the next image (whose histogram is shown in Figure 6.13(b)) has a distinct motion to the lower-right. Likewise, weighted histograms for motion vectors associated with the two corresponding registered images are shown in Figure 6.13(c)-(d), respectively. As can be seen, the distribution of motion vector angles is significantly more uniform for the registered images compared to the unregistered images. This simple comparison indicates that the non-rigid B-spline registration technique has successfully corrected a large portion of the respiratory and cardiac motion artifacts.

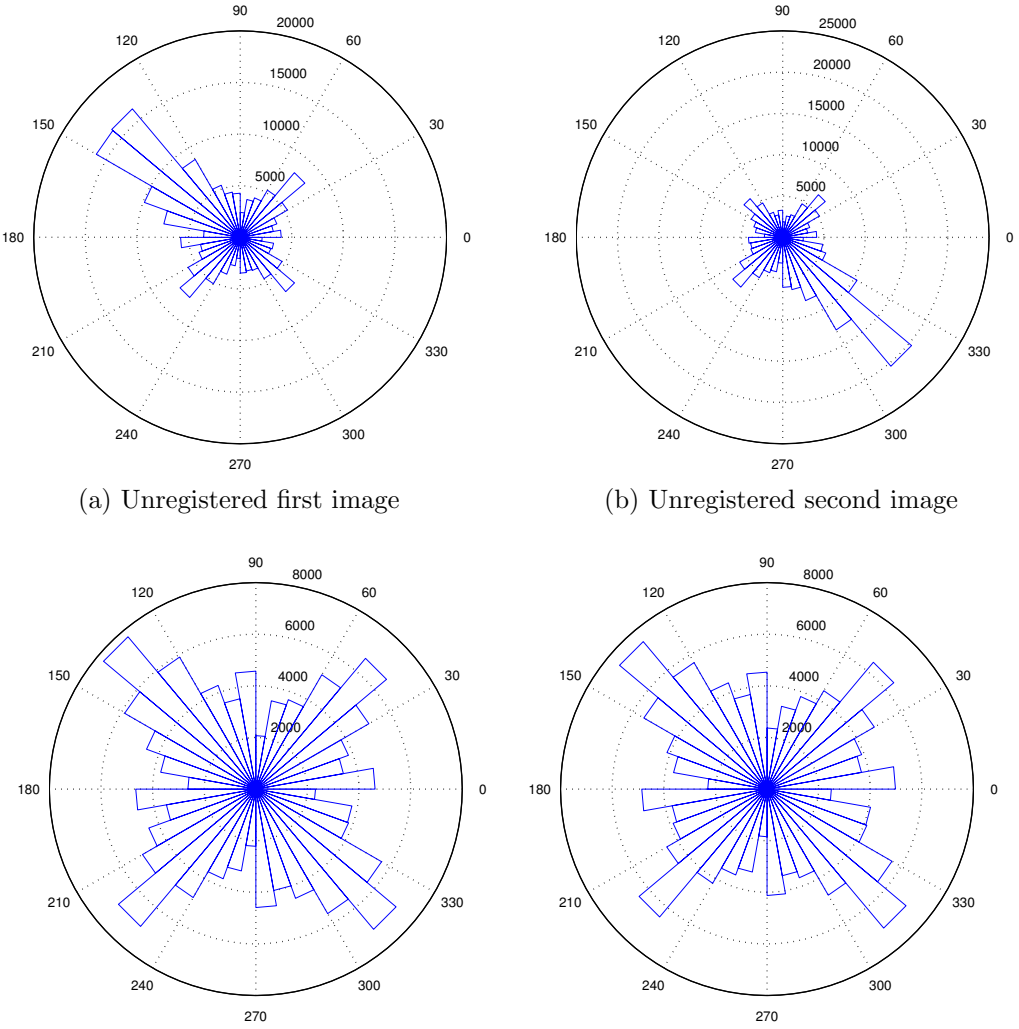

(a) Unregistered first image

(b) Unregistered second image

(c) Registered first image

(d) Registered second image

Fig. 6.13.: Weighted histograms of motion vector angles

We further demonstrate our non-rigid registration technique using B-splines with additional image sets. Figure 6.14(a) shows a single image from a time-series of images collected from the lung of a living rat following injection with fluorescein dextran (which fluoresces green in the vasculature) and Hoechst 33342 (which labels cell nuclei blue). We initially perform the rigid registration method as was performed previously with the sequence of rat kidney images shown in Figure 6.8. By comparing maximum projection and line scan projection images from before and after rigid registration shown in Figure 6.14(b)-(e), these images indicate that rigid registration has barely

corrected the motion artifacts. In fact, one may argue that the registration has even exacerbated the motion artifacts compared to the raw images.

By now utilizing our combined rigid and non-rigid registration method using B-splines, we see in Figure 6.14(f)-(g) that the maximum projection and line scan projection images show extraordinary reduction of the motion artifacts. This clearly illustrates the deficiencies of rigid registration for correction of respiration and heartbeat motion artifacts, while non-rigid registration using B-splines is very promising in this application.

To present a more quantitative measure of registration success, one may consider evaluating a well-established metric such as Target Registration Error (TRE) [137]. However, this registration evaluation metric requires manually identifying fiducial points in corresponding pairs of images. This is quite impractical and labor intensive for image sequences that contain hundreds of images. Therefore, as a more automated quantitative evaluation, we compute an average of sum of squared differences (SSD) of pixel intensities across all images in the sequence. Normalizing this value by the number of pixels in the image is not appropriate because the registered image sequence has a larger field of view. Since each image in the registered sequence contains more matching black pixels, a normalized value would show an improvement in alignment even if no registration had been performed. Results for this image sequence of lung tissue are shown in Table 6.1, which compares SSD values before registration, after rigid registration, and after both rigid and non-rigid registration. Even though Figure 6.14(d) may show a worsening of image alignment, rigid registration has marginally improved image alignment according to the SSD metric. However, non-rigid registration has drastically improved image alignment, according to both a quantitative SSD standpoint and a visual standpoint.

As we have seen, SSD quantitative evaluation does not necessarily match visual evaluation of image alignment. Therefore, in addition to projection images, we also utilize the motion vector analysis described previously as a validation technique. This attempts to identify any distinct motion patterns within the motion vector field prior

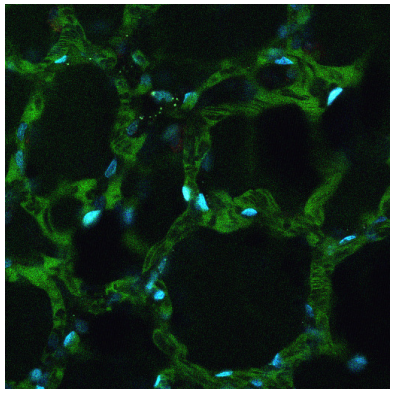

(a) Example image from lung tissue data set

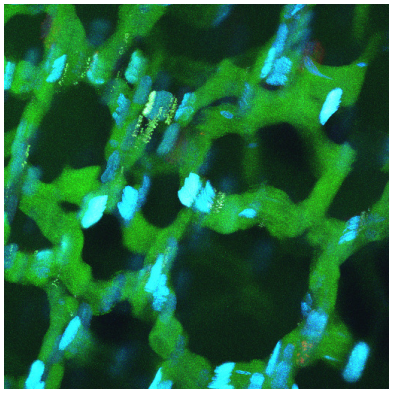

(b) Maximum projection of entire series of images before registration

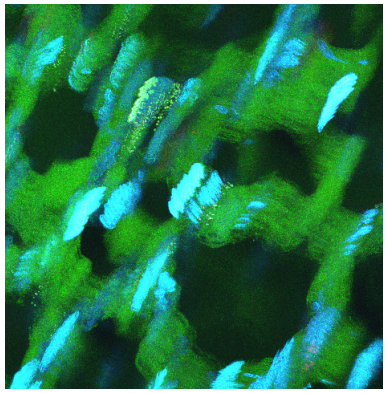

(c) Maximum projection of entire series of images after rigid registration

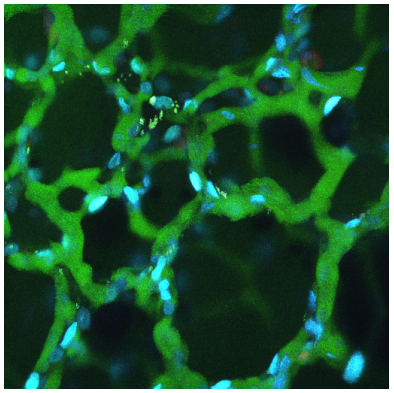

(d) Maximum projection of entire series of images after non-rigid registration

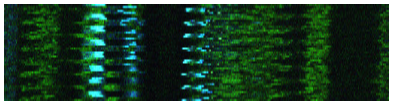

(e) Line scan projection image before registration

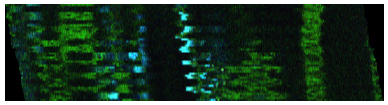

(f) Line scan projection image after rigid registration

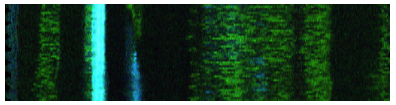

(g) Line scan projection image after non-rigid registration

Fig. 6.14.: Non-rigid registration results using B-splines for lung tissue data set. Image field is 205 μm wide. Image sequence contains 50 frames. Registration was performed using $\lambda = 0.02$ and a control point grid spacing of $\delta_x = \delta_y = 64$ pixels.

Table 6.1: Quantitative registration validation results

Image Sequence	Average SSD per Image	Percent Improvement
Lung without registration	7329.7	—
Lung with rigid registration	7190.5	1.9%
Lung with rigid and non-rigid registration	2739.8	62.6%
Kidney without registration	13208	—
Kidney with rigid registration	12938	2.0%
Kidney with rigid and non-rigid registration	6026	54.4%
Salivary gland without registration	273.0	—
Salivary gland with rigid registration	246.9	9.6%
Salivary gland with rigid and non-rigid registration	124.2	54.5%

to and subsequent to registration. Computation of motion vectors was performed for all images in the sequence, and weighted histograms of motion vector angles with non-zero magnitudes were generated for each image. These histograms are created with 36 bins, and motion vector angles are weighted by motion vector magnitudes. A weighted histogram for one particular image in the lung tissue sequence is shown in Figure 6.15(a). The histogram for the unregistered image is shown in blue, while the histogram for the corresponding registered image is shown in red. As can be seen, the unregistered image has dominant motion to the upper-right and lower-left with respect to its previous image. However, the magnitudes of the motion vectors for the registered image shown in red are significantly reduced compared to the unregistered image. Furthermore, not only are the magnitudes of motion vectors reduced, but the distribution of motion vector angles is significantly more uniform compared to the unregistered image, indicating that motion is not apparent in any particular direction. Comparing magnitude and angle distribution of motion vectors from before and after registration demonstrates that our non-rigid B-spline registration technique has successfully corrected a large portion of the motion artifacts.

Since these weighted histograms omit motion vectors with zero magnitude, we can include these in a 3-D distribution plot of all motion vectors for the same image as shown in Figure 6.15(b)-(c). For the unregistered image, the 3-D distribution plot

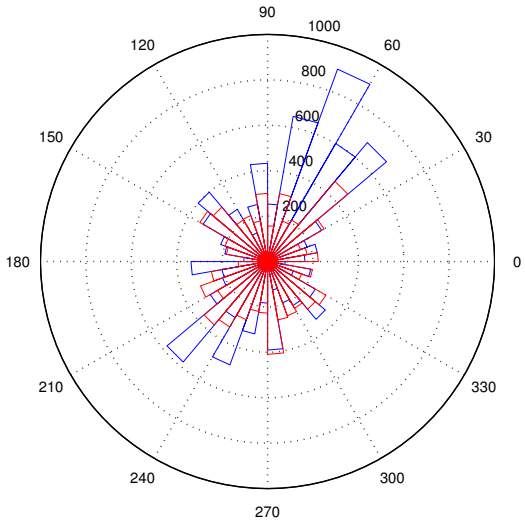

(a) Weighted histogram of motion vector angles for one slice. Histogram for unregistered image is show in blue, while histogram for registered image is shown in red.

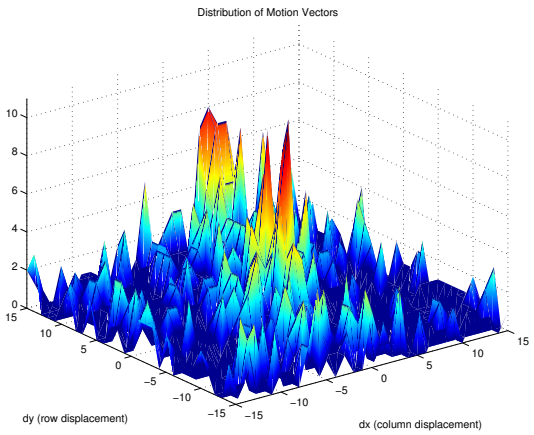

(b) 3-D distribution plot of motion vector displacements before registration

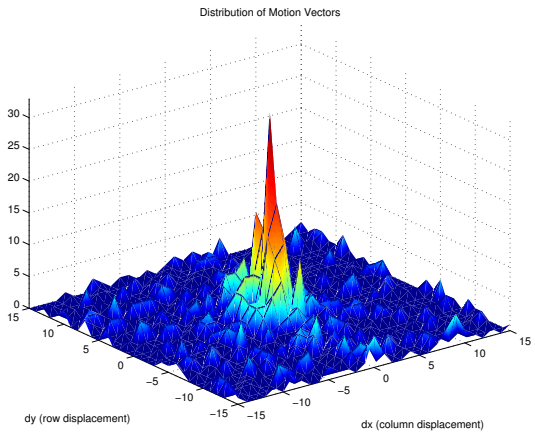

(c) 3-D distribution plot of motion vector displacements after registration

Fig. 6.15.: Motion vector analysis for lung tissue data set shown in Figure 6.14. Motion vector analysis was performed using a 31×31 search window and 16×16 block size.

contains many large peaks across the entire search window, indicating that significant motion has been identified throughout the image. Peaks in the 3-D distribution plot indicate that the image contains many motion vectors with the corresponding magnitude and orientation. In contrast, for the registered image, the vast majority of the

motion vectors are concentrated at the origin, suggesting no motion. Again, this comparison indicates that the non-rigid B-spline registration technique has successfully corrected a large portion of the motion artifacts.

We previously mentioned that our combined rigid and non-rigid registration method is robust and effective on both time-series and three dimensional data. After demonstrating our non-rigid registration technique on images collected in time-series, we will now demonstrate its effectiveness on three dimensional sequences of images. Consecutive images in a three dimensional sequence of images share enough content such that the registration process performs well. Figure 6.16(a) shows a single image from a three dimensional volume collected from the kidney of a living rat injected intravenously with Hoechst 33342 (which labels cell nuclei blue), a large molecular weight dextran that fluoresces red in the vasculature of the glomerulus (center of image), and a small molecular weight dextran that is internalized into endosomes of proximal tubule cells (appearing as fine yellow spots). Specimen motion occurring during collection of this volume is apparent as the smeared appearance in the overlay of two consecutive images shown in Figure 6.16(b).

We illustrate the effectiveness of our combined rigid and non-rigid registration method by showing the overlay of the corresponding two consecutive images after registration shown in Figure 6.16(c). Ghosting artifacts resulting from significant misalignment of objects are obvious in the original volume, but are vastly improved following registration. Therefore, this visual inspection of the registration results confirms that the motion artifacts have largely been corrected.

Again, quantitative SSD values to evaluate registration success are shown in Table 6.1 for this image sequence of kidney tissue. Similar to the lung, rigid registration has marginally improved image alignment according to the SSD metric, while non-rigid registration has drastically improved image alignment. Motion vector analysis was again performed as an additional validation technique. A weighted histogram for one particular image in the kidney tissue sequence is shown in Figure 6.17(a). The histogram for the unregistered image is shown in blue, while the histogram for

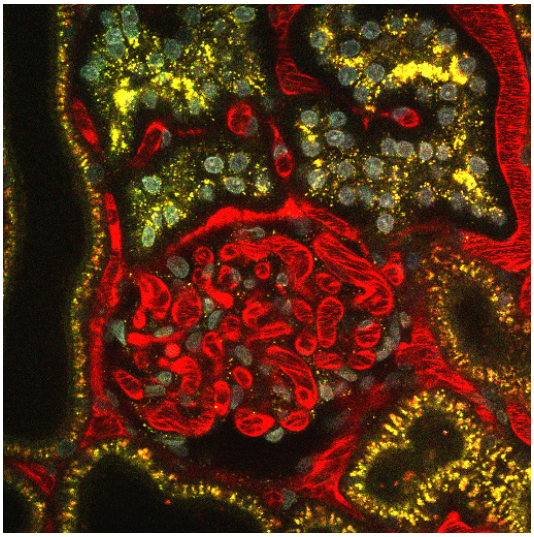

(a) Example image from renal tissue data set

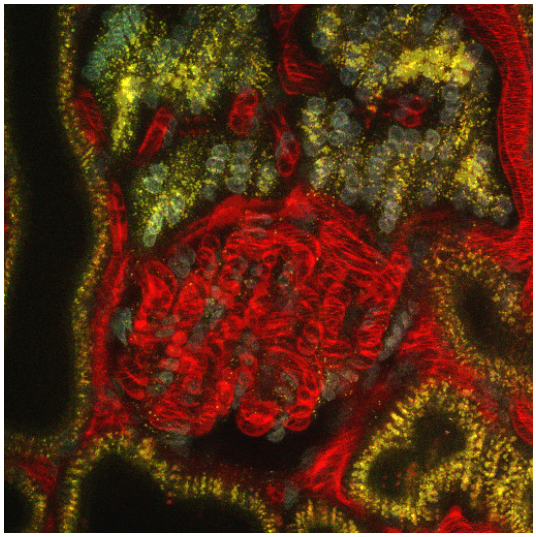

(b) Overlay of consecutive unregistered images

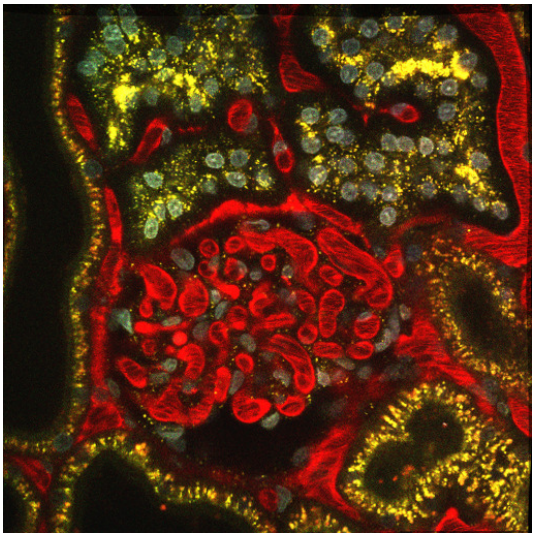

(c) Overlay of consecutive registered images

Fig. 6.16.: Non-rigid registration results using B-splines for kidney tissue data set. Image field is 205 μm wide. Image sequence contains 56 frames. Registration was performed using $\lambda = 0.02$ and a control point grid spacing of $\delta_x = \delta_y = 64$ pixels.

the corresponding registered image is shown in red. As can be seen, the unregistered image has an extremely distinct motion to the upper-right with respect to its previous image. However, the histogram in red shows the near elimination of all motion in the registered image, as all of the histogram bins are near zero and dwarfed by

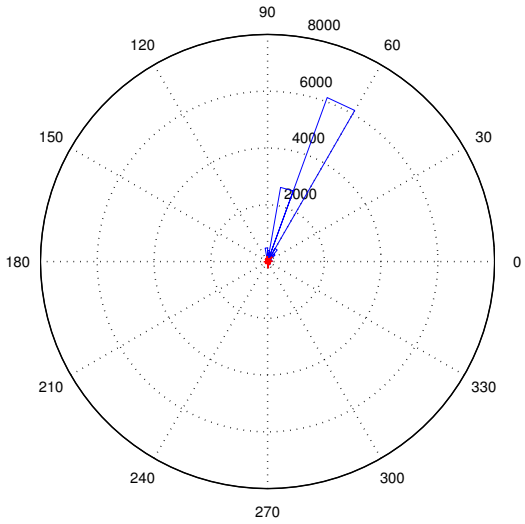

(a) Weighted histogram of motion vector angles for one slice. Histogram for unregistered image is show in blue, while histogram for registered image is shown in red.

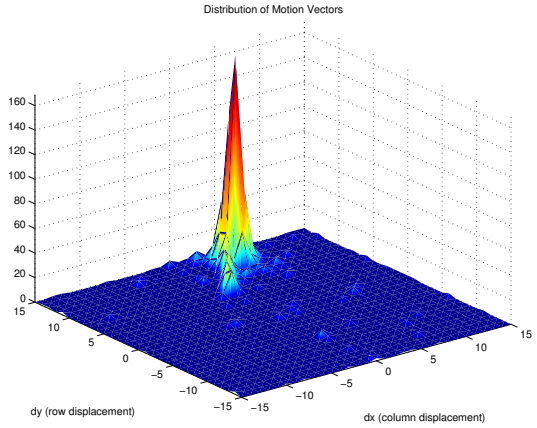

(b) 3-D distribution plot of motion vector displacements before registration

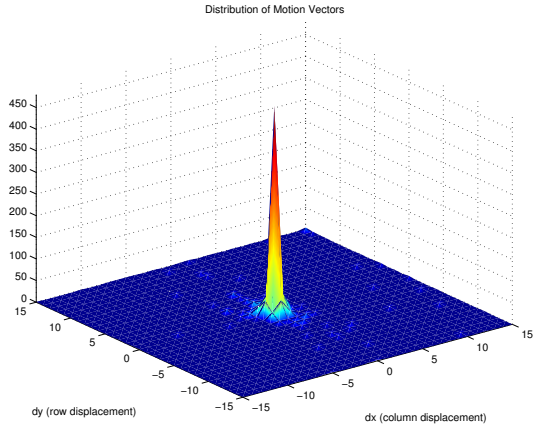

(c) 3-D distribution plot of motion vector displacements after registration

Fig. 6.17.: Motion vector analysis for kidney tissue data set shown in Figure 6.16. Motion vector analysis was performed using a 31×31 search window and 16×16 block size

the histogram bins from the unregistered image. Again, this simple comparison indicates that the non-rigid B-spline registration technique has successfully corrected essentially all of the motion artifacts.

All motion vectors computed across the same image in the sequence are quantified in a 3-D distribution plot and are shown in Figure 6.17(b)-(c). For the unregistered image, the 3-D distribution plot contains one large peak at the edge of the plot, confirming that the majority of the motion vectors suggest upward motion. In contrast, for the registered image, essentially all of the motion vectors are concentrated at the origin, suggesting no motion. Again, this comparison indicates that the non-rigid B-spline registration technique has successfully corrected the vast majority of the motion artifacts.

Our last example shows the effectiveness of motion artifact correction even at the subcellular level. Figure 6.18(a) shows a single image from a time-series of images of a single cell in the salivary gland of a living mouse. The mouse cell is expressing EGFP-clathrin in endosomes and the trans-Golgi network and mCherry-TGN38 in the trans-Golgi network. Since even the slightest motion will compromise the ability to distinguish intracellular organelles, motion artifacts present a serious challenge to intravital microscopy of subcellular processes.

Due to the decreased image resolution and image scale along with more intense motion artifacts compared to the previous image sequences, the smoothness penalty coefficient in the cost function has been reduced by a factor of 4, and the B-spline control point grid spacing has been increased by a factor of 4. A smaller and more dense B-spline control point grid along with a decreased smoothness constraint coefficient allows for more bending and warping in the registration process to correct more intense motion artifacts, both spatially and temporally. Maximum projection images across 15 sequential image planes from before and after registration are shown in Figure 6.18(b)-(c), respectively, demonstrating that registration accomplishes a significant reduction in the motion artifact of the original image series. The correction is somewhat obscured in these images by the fact that the intracellular vesicles actually are in motion. If the full image sequence was available for display, viewers would notice that the registration performs better toward the end of the image sequence where there is more pronounced subcellular motion compared to the beginning of the image

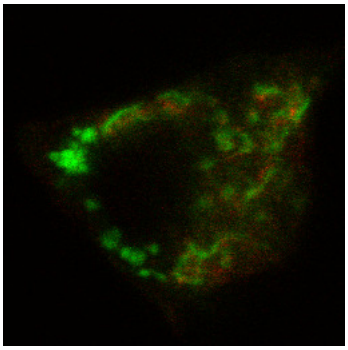

(a) Example image

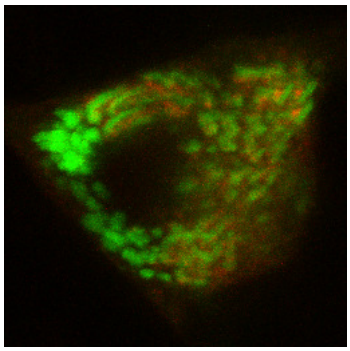

(b) Maximum projection of 15 images before registration

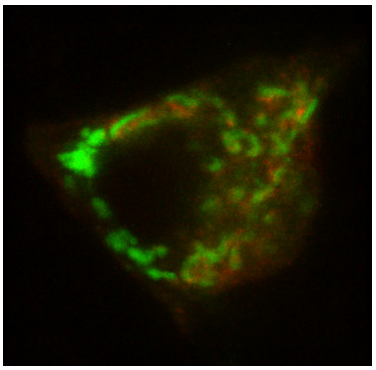

(c) Maximum projection of 15 images after registration

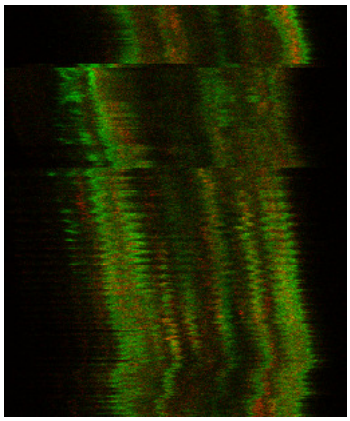

(d) Line scan projection image before registration

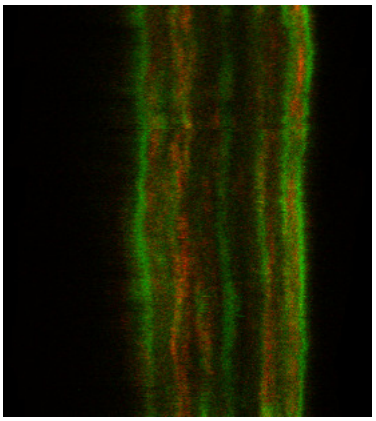

(e) Line scan projection image after registration

Fig. 6.18.: Non-rigid registration results using B-splines for salivary gland data set. Image field before registration is 25 μm wide. Image field after registration is wider because the field has shifted over the time of collection to include more area. Image sequence contains 310 frames. Registration was performed using $\lambda = 0.005$ and a control point grid spacing of $\delta_x = \delta_y = 16$ pixels.

sequence. Perhaps contrary to intuition, the non-rigid registration method will more closely register a pair of images that contains a greater misalignment—up to a certain threshold. If two images are too similar, the smoothness constraint term in the cost function will overpower the similarity metric term. Therefore, for the beginning of the image sequence, where consecutive images are already much more closely aligned, tiny misalignments are allowed to propagate through the registration process. The correction is also apparent in comparison of line scan images from before and after registration shown in Figure 6.18(d)-(e), in which the disjointed subcellular objects of the original image series have been properly aligned into solid, continuous objects through the time-series.

Lastly, quantitative SSD values to evaluate registration success are again shown in Table 6.1 for this image sequence of salivary gland tissue. Similar to both the lung and kidney, rigid registration has marginally improved image alignment, while non-rigid registration has drastically improved image alignment. Motion vector analysis is performed to validate the subcellular non-rigid registration results as well. A weighted histogram for one particular image in the salivary gland tissue sequence is shown in Figure 6.19(a). The histogram for the unregistered image is shown in blue, while the histogram for the corresponding registered image is shown in red. The histogram bins for the registered and unregistered images show little distinction between each other. However, the comparison of the 3-D distribution plots for both unregistered and registered images shown in Figure 6.19(b)-(c) is much more convincing. Motion vectors for the registered sequence are much more concentrated at the origin compared to those for the unregistered image. This comparison indicates that the non-rigid B-spline registration technique has successfully corrected a large portion of the motion artifacts at the subcellular level as well.

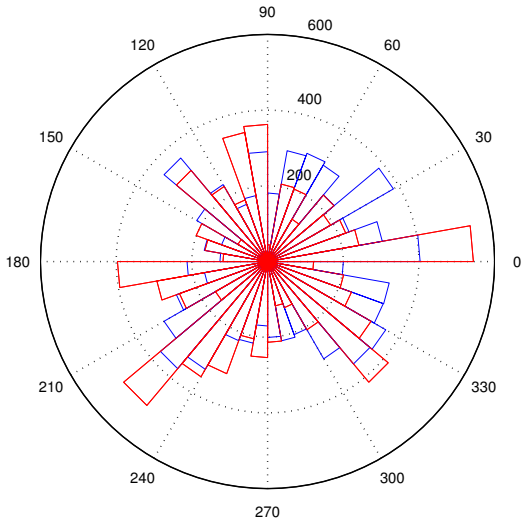

(a) Weighted histogram of motion vector angles for one slice. Histogram for unregistered image is show in blue, while histogram for registered image is shown in red.

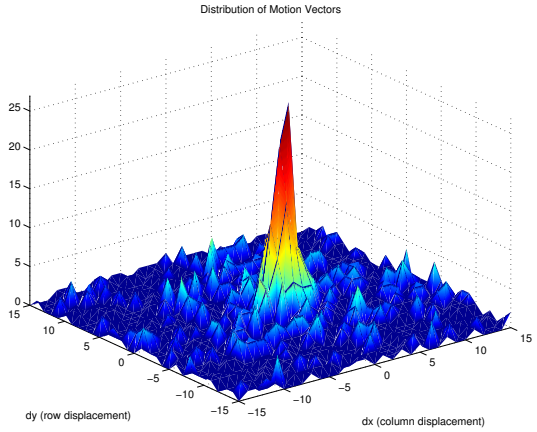

(b) 3-D distribution plot of motion vector displacements before registration

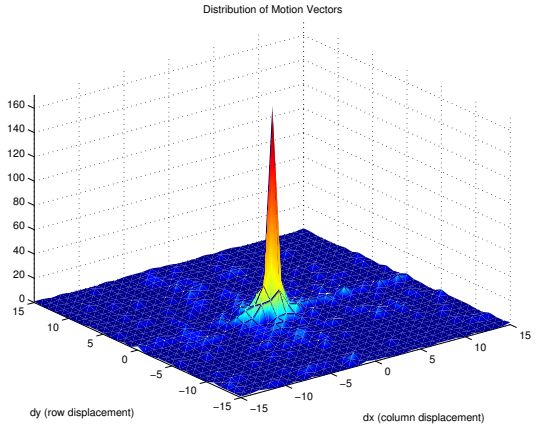

(c) 3-D distribution plot of motion vector displacements after registration

Fig. 6.19.: Motion vector analysis for salivary gland data set shown in Figure 6.18. Motion vector analysis was performed using a 31×31 search window and 8×8 block size.

6.5.3 Multi-Resolution Approach to Non-Rigid Registration

To further improve our registration results, we demonstrate our multi-resolution non-rigid registration method on a stack of approximately 150 images collected in time-series from the lung of a living rat. The data were provided by Dr. Irina Petra-

Table 6.2: Single-stage non-rigid registration results

Registration Parameters	Percent Improvement using SSD	Percent Improvement using GC
$\delta_x = \delta_y = 128$	55.8%	197.7%
$\delta_x = \delta_y = 64$	61.5%	258.9%
$\delta_x = \delta_y = 32$	64.3%	299.3%
$\delta_x = \delta_y = 16$	64.9%	304.6%

che, Indiana University School of Medicine, as part of the collaboration that resulted in [138]. Motion artifacts present an enormous challenge for intravital microscopy. In order to reconstruct a three dimensional volume from a series of images collected over a range of depths in a tissue, or to quantify dynamic changes in fluorescence in a series of images collected from the same structure over time, motion-induced artifacts resulting from respiratory and cardiac function must be eliminated. Figure 6.20(a) shows a single image from this stack.

We first use non-rigid registration using a single-stage process, where only one control point spacing is used. We use this method for multiple trials with a variety of spacings, including 128, 64, 32, and 16 pixels between control points. After registration, we determine the average of both sum of squared differences (SSD) of pixel intensities and sum of gradient correlation (GC) across all images in the sequence as quantitative measures of registration performance [89, 139]. We choose metrics that are unrelated to the similarity metric used in the cost function. Results for this image sequence are shown in Table 6.2 which compares the SSD and GC before and after single-stage registration. For all of these trials, we empirically choose $\lambda = 0.01$, as it demonstrated the best results over a wide range of possible values. We see that non-rigid registration has significantly improved image alignment. Note that using a densely spaced grid of control points, which permits increased bending and warping to correct more intense motion artifacts, slightly improves image alignment. However, this is not necessarily true for all data sets. With the transformation able to deform

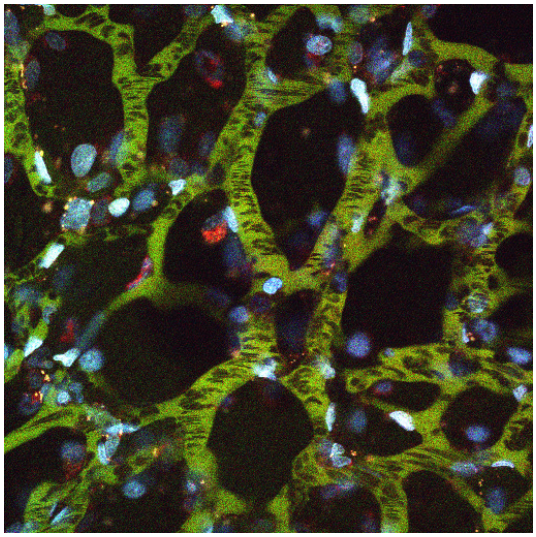

(a) Single example image from lung data set

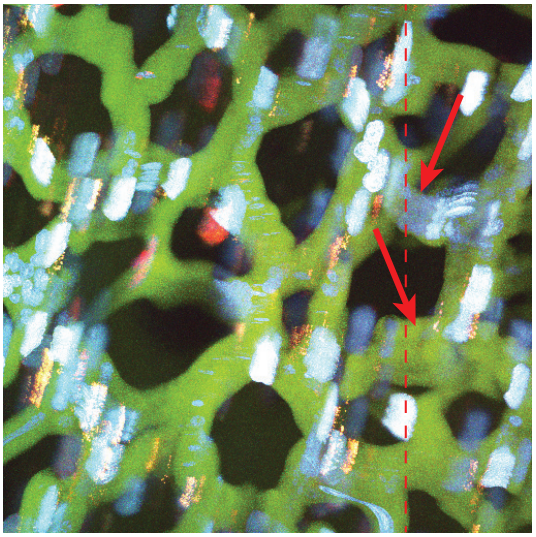

(b) Maximum projection before registration

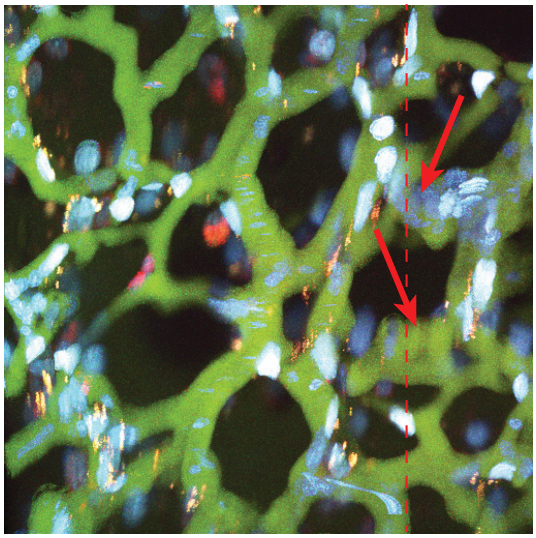

(c) Maximum projection after single-stage registration

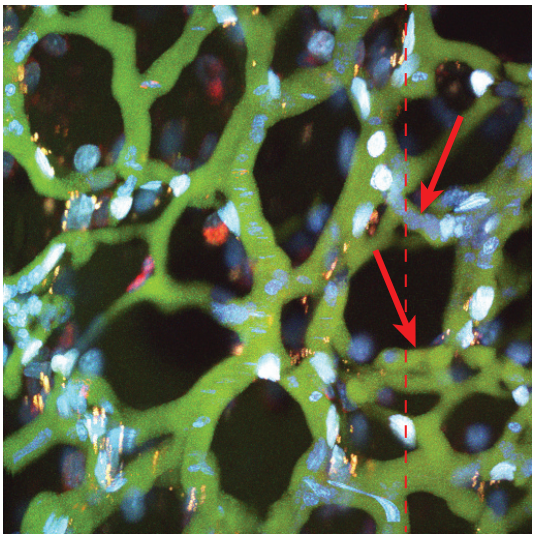

(d) Maximum projection after two-stage registration

Fig. 6.20.: Maximum projection images of multi-resolution registration results. Image field is 205 μm wide.

more rapidly, particular control points during the optimization may be more likely to become attracted to local minima rather than global minima.

Next, we use the proposed multi-resolution approach and execute non-rigid registration in multiple stages, using multiple grid spacings in a coarse-to-fine manner. For an arbitrary number of stages in the multi-resolution process, the grid spacings for the

Table 6.3: Two-stage non-rigid registration results

Registration Parameters	Percent Improvement using SSD	Percent Improvement using GC
$\delta_x^{(1)} = \delta_y^{(1)} = 128$ $\delta_x^{(2)} = \delta_y^{(2)} = 64$	67.6%	293.1%
$\delta_x^{(1)} = \delta_y^{(1)} = 64$ $\delta_x^{(2)} = \delta_y^{(2)} = 32$	71.5%	341.4%
$\delta_x^{(1)} = \delta_y^{(1)} = 32$ $\delta_x^{(2)} = \delta_y^{(2)} = 16$	73.7%	364.1%
$\delta_x^{(1)} = \delta_y^{(1)} = 16$ $\delta_x^{(2)} = \delta_y^{(2)} = 8$	74.0%	365.8%

Table 6.4: Three-stage non-rigid registration results

Registration Parameters	Percent Improvement using SSD	Percent Improvement using GC
$\delta_x^{(1)} = \delta_y^{(1)} = 128$ $\delta_x^{(2)} = \delta_y^{(2)} = 64$ $\delta_x^{(3)} = \delta_y^{(3)} = 32$	74.2%	368.8%
$\delta_x^{(1)} = \delta_y^{(1)} = 64$ $\delta_x^{(2)} = \delta_y^{(2)} = 32$ $\delta_x^{(3)} = \delta_y^{(3)} = 16$	76.4%	393.4%
$\delta_x^{(1)} = \delta_y^{(1)} = 32$ $\delta_x^{(2)} = \delta_y^{(2)} = 16$ $\delta_x^{(3)} = \delta_y^{(3)} = 8$	77.8%	407.2%

horizontal and vertical directions for the n-th stage are denoted $\delta_x^{(n)}$ and $\delta_y^{(n)}$, respectively. We begin with a two-stage registration, with $\delta_x^{(2)} = \delta_x^{(1)}/2$ and $\delta_y^{(2)} = \delta_y^{(1)}/2$. Again, we choose a variety of spacings, including 128, 64, 32, and 16 pixels between control points for $\delta_x^{(1)}, \delta_y^{(1)}$. Results comparing the SSD and GC for this two-stage process are shown in Table 6.3. We notice that the percent improvements in average SSD and GC per image have increased substantially when comparing similar grid spacings for single-stage registration. A multi-resolution approach has improved image alignment with minimal computational cost.

To further improve image alignment, we investigate three-stage registration, with $\delta_x^{(3)} = \delta_x^{(2)}/2 = \delta_x^{(1)}/4 =$ and $\delta_y^{(3)} = \delta_y^{(2)}/2 = \delta_y^{(1)}/4$. As before, we choose a variety of spacings, including 128, 64, and 32 pixels between control points for $\delta_x^{(1)}, \delta_y^{(1)}$. Results comparing the SSD and GC for this three-stage process are shown in Table 6.4. Note that the percent improvements in average SSD and GC per image have increased, but not as much compared with the two-stage registration process. One drawback of using an additional stage in the registration is that the registered images undergo an additional interpolation stage, possibly blurring and obscuring important cellular structures. One may argue that the percent improvements in SSD and GC are not beneficial enough to offset the loss in image sharpness. Two-stage registration appears to be a moderate compromise between registration accuracy and image quality.

To obtain a more qualitative and visual evaluation of registration accuracy, we compare maximum projection images from before registration, after single-stage registration, and after two-stage registration. Maximum projection images are assembled by pixel-wise comparison of the intensities of each of the images in the stack and retaining the largest value. For ideally registered images, structures will have perfectly sharp edges with no ghosting or smearing in the maximum projection images. In contrast, before registration, we see in Figure 6.20(b) that the maximum projection image exhibits distinct blurring of object edges, indicating severe misalignment of objects. Particular areas of interest that exhibit large amounts of smearing are indicated by the two arrows. Figure 6.20(c) shows that single-stage registration has improved the alignment of cellular structures as the smeared appearance has been reduced. Comparing the same areas of interest indicated by the two arrows, we see that the vasculature is narrower and has more sharply defined edges, indicating improved image alignment. However, in Figure 6.20(d), after two-stage registration, the maximum projection image shows incredible and vast improvement of object alignment compared to Figure 6.20(b), indicating extraordinary reduction of the motion artifacts in the original image series. The two areas of interest confirm this by showing

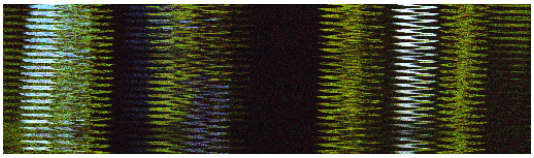

(a) Before registration

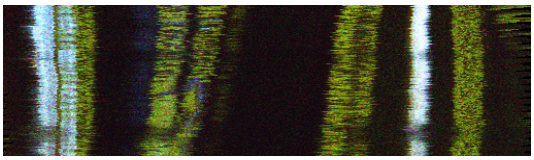

(b) After single-stage registration

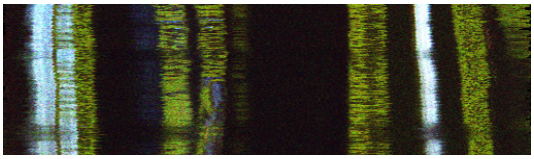

(c) After two-stage registration

Fig. 6.21.: Line projection images of multi-resolution registration results. Image field is 205 μm wide.

further improvement in image alignment with significantly increased edge sharpness and increased narrowness of the vasculature.

As an additional visual comparison, line scan projection images are created from before registration, after single-stage registration, and after two-stage registration. Line scan projection images are assembled by selecting a single line of pixels as one axis and plotting this against time/depth on the other axis. These images are shown in Figure 6.21, with the line selected to create the projection image shown as a dashed line in Figure 6.20. For ideally registered images, we should see perfectly aligned, solid, continuous, vertical structures in the line projection images. In contrast, before registration, we see in Figure 6.21(a) that the line scan projection exhibits disjointed cellular structures as there is distinct back-and-forth motion. In Figure 6.21(b), after single-stage registration, the two nuclei labeled in blue on both the left and right side of the image show much improved vertical continuity. However, the vasculature labeled in green in the middle of the projection image exhibit drifting. In Figure 6.21(c), after two-stage registration, both the nuclei and vasculature show continuity and no

drifting and are vastly improved compared to Figure 6.21(a) and Figure 6.21(b). We have used both the SSD metric for quantitative evaluation, and maximum projection and line scan projection images for qualitative evaluation in our previous work [125].

6.5.4 Correction for Three Dimensional Volumetric Data

Our non-rigid registration method using B-splines performs well, especially for time-series image sets. It also performs well for three dimensional image sets, as sufficient image content is shared between two consecutive images for the registration similarity metric to successfully match the images. However, one particular issue remains that only affects three dimensional data sets. Since the registration technique deforms the image so that it most closely matches the preceding image (given the smoothness constraint), three dimensional objects such as spherical nuclei are deformed into cylindrical shapes. To show that we can maintain the three dimensional topology and structure of cellular objects, we demonstrate our three dimensional correction on a new image volume of a hepatocyte in the liver of a living rat expressing GFP-actin.

An example image from this volume is shown in Figure 6.22(a). A maximum projection of the entire image series before any non-rigid registration is shown in Figure 6.22(b). Severe misalignment and motion is noticed along the boundary of the hepatocyte. We first perform non-rigid registration as we have done previously, and compare these results to those using the method that includes the new correction for three dimensional data. Maximum projection images without and with the correction are shown in Figure 6.22(c) and (d), respectively. These projection images show only very subtle differences between the two results, while both are vast improvements over the maximum projection of the original volume. A more convincing improvement of results with the addition of the three dimensional correction is shown in Figure 6.22(e)-(f). Here, we overlay the single slice shown in Figure 6.22(a) with the corresponding single slice from the registered sequence of images, both without

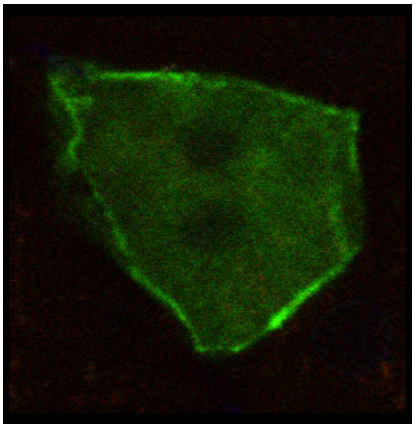

(a) Example image

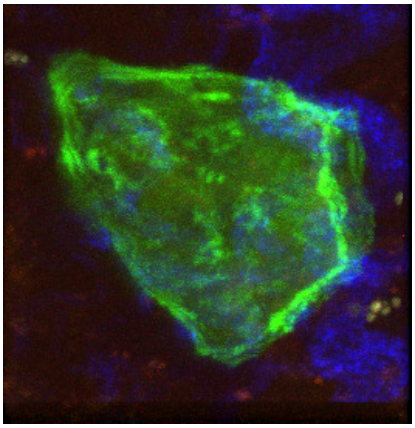

(b) Maximum projection of original sequence

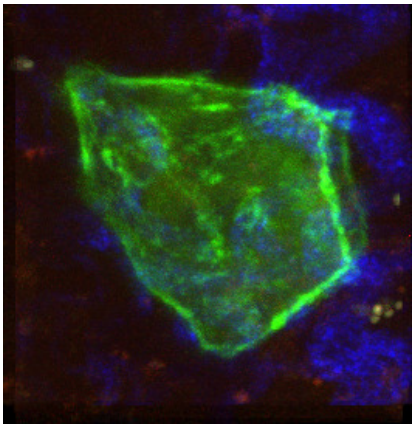

(c) Maximum projection without 3-D correction

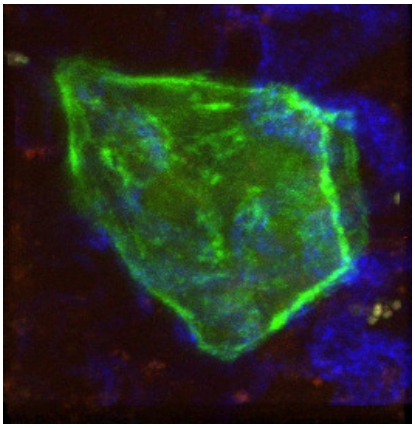

(d) Maximum projection with 3-D correction

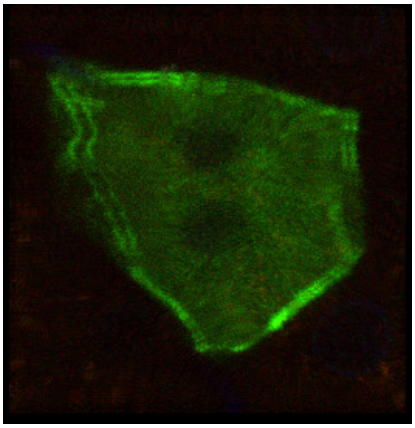

(e) Overlay without 3-D correction

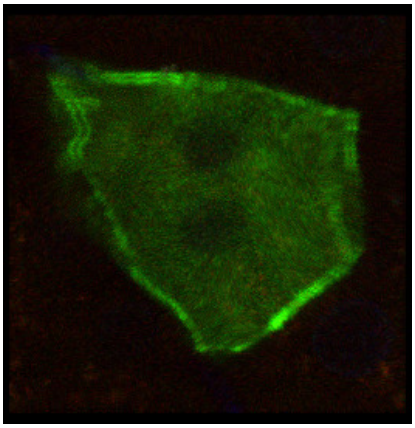

(f) Overlay with 3-D correction

Fig. 6.22.: Non-rigid registration results with 3-D correction

and with the three dimensional correction, respectively. In Chapter 5, we argue that the size and shape of any object is "true" in a single image, and we aim to reduce the change in size and shape from image to image. We see in Figure 6.22(e) that the image has been deformed more without the three dimensional correction. By including the three dimensional correction, the image is more similar to the original slice, as shown in Figure 6.22(f) since the boundaries of the hepatocyte are closer to each other. Therefore, even though the maximum projection images are very similar with both showing incredible reduction of motion artifacts, by including the three dimensional correction, images are minimally deformed, preserving the "true" size and shape of structures.

6.6 3-D Active Surfaces

We now divert away from registration and revert back to segmentation and the method described in Chapter 4. We demonstrate our three dimensional active surface segmentation method on a volume containing approximately one hundred images of nuclei acquired from the kidney of a rat. This is the same volume that was initially introduced in the first section of this chapter. The images in this data set have been corrupted with noise from a variety of sources, including photon shot noise and detector noise. This is due to fluorescence microscopy images characteristically having a low signal-to-noise ratio, reflecting the limited number of photons collected. The objective is to identify and segment individual nuclei from the three dimensional volume for future quantification.

We choose $\Delta t = 1$, $\lambda_{in} = \lambda_{out} = 1$, and $\alpha = 1$. For our pre-processing step, we choose $r = 3$ as the radius of our morphological structuring element. We choose an initial contour/surface ϕ^0 as a cube encompassing the entire volume. Since it is difficult to render our three dimensional volume so that nuclei do not occlude each other while simultaneously demonstrating proper segmentation, we instead show example slices in the xy, yz, and xz planes. Segmentation results shown as slices from

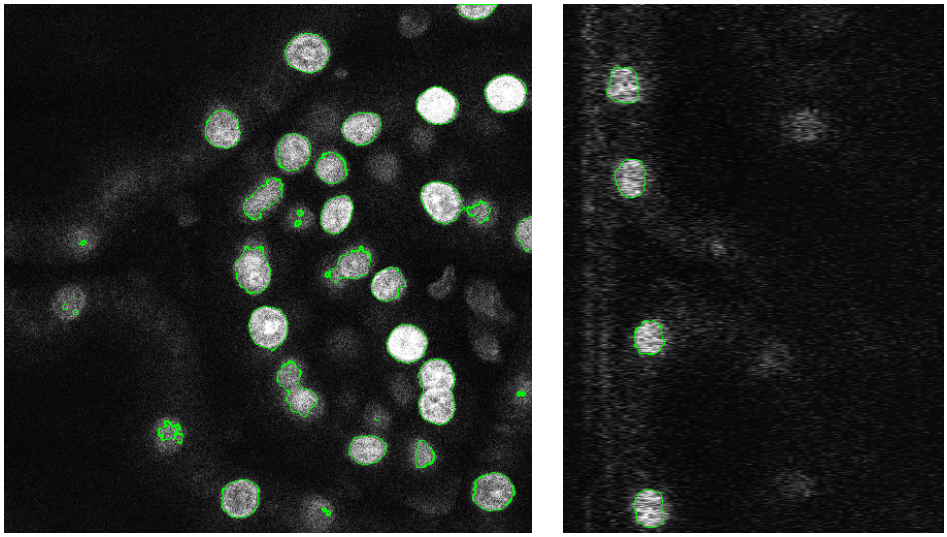

(a) xy plane

(b) yz plane

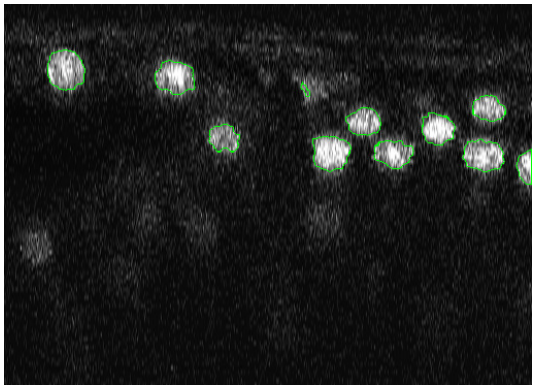

(c) xz plane

Fig. 6.23.: Active surface segmentation results

each of the three orthogonal planes are shown in Figure 6.23, with the final active surface segmenting the nuclei shown in green.

We see in all three orthogonal planes that nuclei are segmented generally with a circular shape, indicating that the active surfaces in three dimensions are generally spherical, as expected. These three slices are representative of the segmentation results for each of the three planes throughout the entire volume.

We compare these results from our current active surfaces method with those from our proposed segmentation method described in Chapter 2 [68]. This method was a pseudo-three dimensional segmentation method tasked with the same objective.

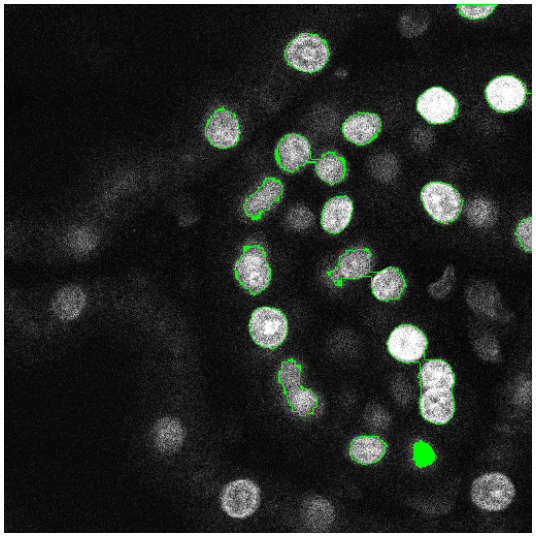

(a) xy plane

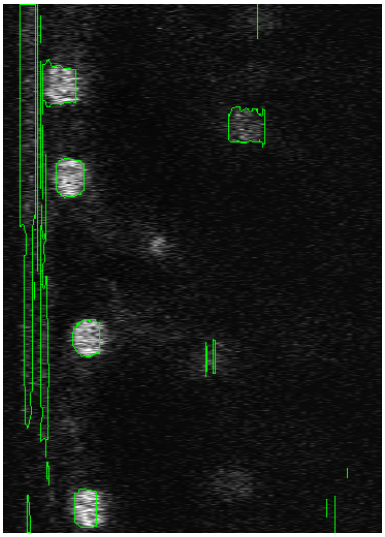

(b) yz plane

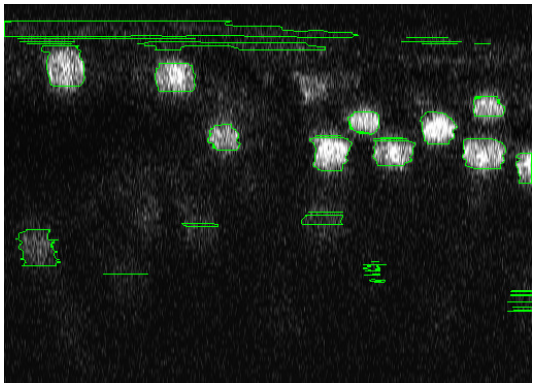

(c) xz plane

Fig. 6.24.: Segmentation results from prior work

Even though the entire series of images forms a three dimensional volume, the images are acquired slice-by-slice in the xy plane. Similarly, our previous analysis segmented each slice individually. The series of segmentation results from our previous method can then be concatenated along the z-axis to form a three dimensional volume.

The corresponding same three slices from the xy, yz, and xz planes shown in Figure 6.23 are also shown in Figure 6.24 for our previous segmentation method. When viewed from the xy plane, segmentation results for the two methods are very similar. However, segmentation results differ significantly for the xz and yz planes between the two methods. Since our previous method performed segmentation on a

slice-by-slice basis, it does not simultaneously utilize knowledge about the entire three dimensional topology of the image volume. Therefore, even though segmentation results may appear reasonable and acceptable in the xy plane, when concatenated along the z-axis, the results may be unrealistic in the xz and yz planes.

For example, on the left side of Figure 6.24(b) and at the top of Figure 6.24(c), corresponding to the top of the image volume, there are many irregularities in the final segmentation. This is due to the increased background signals arising in the tissue at the beginning of the image stack, which interferes with the final segmentation. Additionally, at the lower-right corner of Figure 6.24(a), there is a nucleus that is fully occluded by the segmentation. This occlusion is due to it being an edge curve, indicating that this nucleus was not segmented in the xy planes above and below the displayed xy plane. Obviously, it is unrealistic for a nucleus to appear in a single frame and not appear in the immediately preceding and superseding planes. The results shown in Figure 6.23 exhibit none of the aforementioned abnormalities. The active surfaces method is a native three dimensional segmentation method that utilizes the entire three dimensional topology at every iteration.

7. CONCLUSIONS AND FUTURE WORK

Intravital microscopy is a powerful technique for studying physiological processes in the most relevant context—in the living animal. However, developing assays of physiological function will require developing novel methods of digital image analysis that will support quantitative analysis. Insofar as accurate image registration is prerequisite to quantitative analysis of time-series and volumetric image data, the development of effective methods of image registration is fundamentally important to realizing the potential of intravital microscopy as a tool for understanding and treating human diseases. The techniques described in this thesis will enable new studies that were previously impossible.

This thesis has described a streamlined and integrated approach to both segment and register sets of multiphoton microscopy images. In particular, we have investigated multiple approaches to both segmentation and registration, and integrated them together into a single workflow.

7.1 Conclusion

This thesis described a comprehensive approach to segment and register multiphoton microscopy image data sets, overcoming many of the challenges associated with optical microscopy. Experimental results indicated that this method is promising in segmenting objects in time-series data sets as well as data sets comprised of images acquired at increasing tissue depths. Specifically, the main contributions in the area of segmentation are:

- We combined well-established image analysis techniques in a novel and unique way to create integrated segmentation and registration methods for microscopy images. In particular, we utilize a Bayesian estimation technique for denoising,

low-pass filtering to provide blurring, adaptive thresholding to produce binary images, and morphological filtering for post-processing.

- User interaction may be introduced to modify certain parameters of the analysis and aid in the segmentation process. These parameters may be adjusted depending on specific input data sets to produce more desirable results.

- We modify a three dimensional active surface segmentation method to better handle the characteristics of microscopy volumes. In particular, we reduce and simplify terms contained within the cost function to reduce the interference caused by the image noise. Combined with pre- and post-processing techniques, this segmentation method overcomes many of the challenges associated with microscopy image volumes including low edge detail, decreasing image contrast with increasing tissue depth, and increased image noise.

While intravital microscopy has made it possible to apply many of the same techniques that have been productively used in microscopic studies of cultured cells to studies of single cells *in vivo*, quantitative analysis is frequently limited by motion artifacts, which—with the notable exception of the brain—are ubiquitous to intravital microscopy. Motion artifacts, resulting from respiration and heartbeat, limit resolution and preclude segmentation, which is prerequisite to image quantification. In addition, many other well-known challenges complicate quantitative analysis of fluorescence images collected from living animals. Microscopy volumes are inherently anisotropic, with aberrations and distortions that vary in different axes. At a larger scale, contrast decreases with depth in biological tissues. This contrast decrease aggravates a general problem of fluorescence images, which characteristically have low signal levels. Signal levels are further decreased by the need for high image capture rates necessary to image dynamic biological structures. It has been demonstrated that image registration can significantly improve image segmentation performance, especially with volumetric data [47]. However, images with poor contrast and low resolution generally preclude registration methods involving landmarks, and decrease

the ability of intensity-based registration methods to properly identify corresponding objects across images. Furthermore, biological structures often consist of many different kinds of irregular and complicated structures that are frequently incompletely delineated with fluorescent probes. With edges of biological structures sparse and poorly defined, gradient- and edge-based error metrics used in registration methods will perform poorly. Low contrast and small intensity gradients in multiphoton image volumes cause image analysis and rendering results to be very sensitive to small changes in parameters, resulting in the failure of typical image registration methods.

Despite all of the challenges discussed, we have described an image registration method that will aid in future segmentation and other image analysis techniques, supporting both reconstruction of three dimensional images and quantitative analyses of images collected in time-series. Specifically, the main contributions in the area of registration are:

- We demonstrated that a combination of rigid and non-rigid registration techniques is capable of significantly improving the quality of microscope images collected in time-series or in three dimensions from living animals.

- We extend registration methods to handle challenges imposed by multiphoton microscopy. Microscopy images are often collected as entire data sets of images. While typical image registration methods may operate with just a single pair of images, we extend the methods and utilize registration with an entire data set often consisting of hundreds of images. Furthermore, these data sets often contain multi-channel color images. Traditional registration often assumes grayscale images. Therefore, we develop a metric for color images so that registration may be used to analyze both single- and multi-channel microscopy images.

- We have developed and extended a non-rigid registration method that improves the quality of images collected in intravital microscopy. In particular, we effectively correct for motion artifacts in sequences of intravital microscopy images

collected in time-series (a series of images acquired sequentially from a single focal plane in the specimen) or in three dimensional volumes (a progression of images corresponding to sequential and evenly spaced focal planes looking deeper in the tissue), based upon a non-rigid registration technique using B-splines.

- User interaction may be introduced to modify certain parameters of the analysis, including control point grid spacing and the similarity cost coefficient.

- We extend our non-rigid registration in a multi-resolution fashion to reduce motion artifacts and improve image alignment, according to both quantitative SSD and GC metrics and visual evaluation. A two-stage registration process provides significant improvement to registration accuracy over a single-stage process. A three-stage registration process allows further improvement in registration accuracy, but may degrade image quality.

We demonstrate that this registration technique is sufficiently robust to overcome many of the challenges outlined above, and is paramount to any image analysis to follow. Experimental results indicated that this method is effective for correcting motion artifacts in image sequences collected in time-series or in three dimensions, and is effective for a wide range of tissues including image volumes collected from the kidney, lung, liver, and salivary gland of living rodents, exemplifying the versatility of our registration method. With the one exception of the subcellular salivary gland images, all image sequences utilized identical sets of registration parameters, including grid point spacing and smoothness penalty cost coefficient. This demonstrates that a default set of parameters can be chosen to perform reasonably well to register a wide variety of image sequences. Furthermore, the rigid registration section of our method has a wide capture radius and has a strong ability to correct large displacements. The non-rigid registration section of our method is able to correct small to medium discontinuities. As a result, with the combination of the two, we are able to correct

a wide range of discontinuities. Therefore, this registration method demonstrates profound versatility and robustness.

Objective and quantitative evaluation of our results proves to be difficult due to the lack of ground truth data. The main contributions in the area of segmentation and registration validation are:

- Evaluation of segmentation results has been initially addressed by imaging the same specimen from bottom to top and top to bottom, producing flipped volumes.

- We borrow techniques from video compression, specifically motion estimation and compensation, and use this as a validation tool for our registration methods. Evaluation of registration results has been initially addressed subjectively by visually evaluating overlay images, maximum projection images, and line scan projection images, and objectively by using using block motion estimation vectors.

Even with the lack of ground truth, the results from these images all contribute to demonstrating the efficacy of our non-rigid registration method using B-splines. However, with regard to both segmentation and registration, evaluation of accuracy in contrast to precision remains difficult as judgments are significantly more subjective and less objective.

7.2 Future Work

Channel crosstalk and saturation were described as some of the many challenges imposed by intravital microscopy. We described a technique we termed as *green component clamping* as an attempt to address these issues. However, additional work may be conducted to attempt to reconstruct the true or ideal channels from the imperfectly isolated channels. For example, the red channel has been described to often contain structures from all three channels. Therefore, the contributions from

the green and blue channels must be removed to successfully reconstruct the "true red" channel.

Reconstruction of these "true" channels may aid with both segmentation and registration by isolating and separating the individual tissue types and cellular structures within the image sequences. Segmentation and registration for a specific image may also be performed on different channels. For example, one channel may contain objects that should observe no motion, but may not contain the same objects desired to be segmented. Therefore, this channel is ideal for registration, but the segmentation process may use a different channel.

Isolation and separation by reconstruction of the "true" channels may also aid in the segmentation of overlapping objects within the scene. Regarding our three dimensional active surface segmentation method, one drawback includes having nuclei that are overlapping each other being segmented as a single object. Future work will involve identifying these objects as multiple separate nuclei, perhaps by including *a priori* shape information.

One drawback of our current non-rigid registration method using B-splines is that a handful of parameters must be chosen by the user before execution. For example, the choice of grid spacing and smoothness penalty coefficient must be manually selected. The method may be improved by possibly including these manually selected parameters into the optimization process, reducing necessary user input and interaction. Furthermore, one may examine automated approaches to determine the appropriate/optimal number of stages in a multi-resolution approach.

It is known that motion artifacts are induced by respiration and heartbeat. Since these two biological processes are rhythmic and cyclical, the motion artifacts present in the image sequences also exhibit rhythmic and cyclical patterns. Assuming that it is possible for these biological processes to be recorded during the image acquisition process, it may be possible to correlate respiration and heartbeat waveforms with the registration process. For example, if it is known when the specimen will respire or exhibit heartbeat contractions, the registration process may know when to specifically

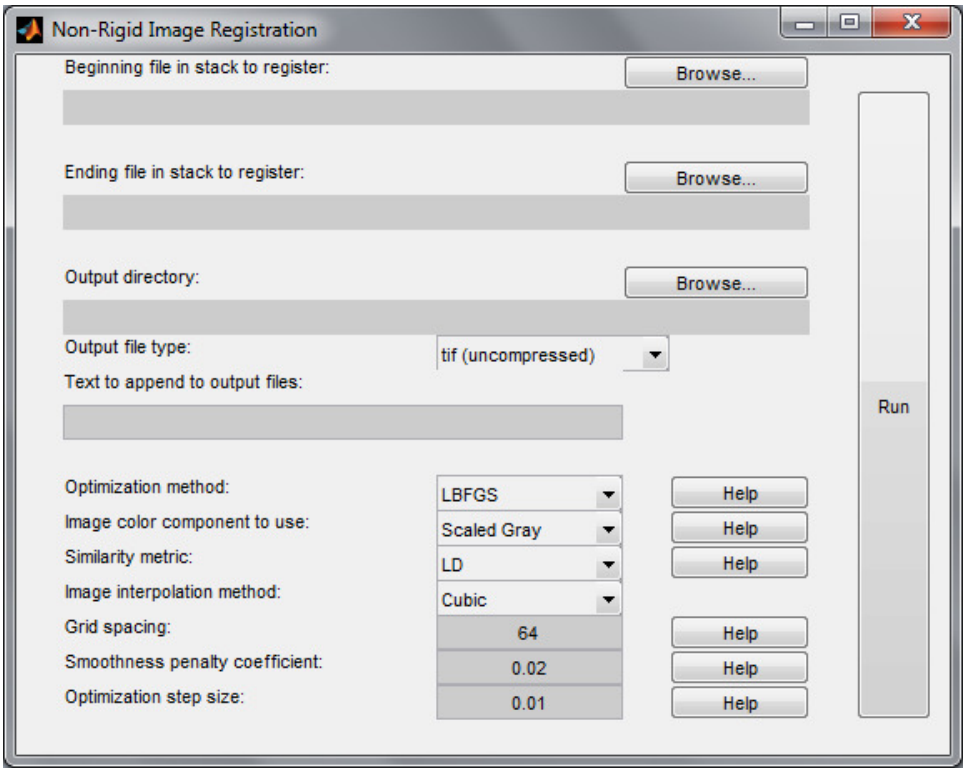

Fig. 7.1.: Graphical user interface screen shot

expect motion artifacts to occur within the image series and correct these artifacts accordingly. Additionally, the degree of correction may also be correlated with the strength or amplitude of the respiration and heartbeat waveforms.

We can further the ambition of this project by implementing our analysis system as a real-time system. Currently, analysis is performed on image sequences only after acquisition is completed. Cases can be imagined where the technician performing the data acquisition may benefit from real-time feedback from the segmentation and registration analysis. For example, if the analysis is performing poorly, the technician may be able to alter parameters of the acquisition process in real-time, avoiding the time and financial costs of possibly requiring additional and repeated data acquisitions in the future.

All methods have been implemented either in MATLAB, or in C++ using ITK[1]. At the time of development, computational runtime was a secondary concern compared to segmentation and registration performance and accuracy. The future goal of a real-time implementation corresponds with improving the implementation details of our system. Biologists are particularly interested in an easy-to-use tool to interact with our implementation. A graphical user interface (GUI) is currently being developed as a way for individuals to interact with our segmentation and registration methods. Thus far, a GUI for the non-rigid registration aspect of our method has been developed, where a screen shot is shown in Figure 7.1. Future work will include further developing this graphical user interface to include our segmentation and rigid registration methods.

7.3 Publications Resulting from This Work

Journal Publications

- **K. S. Lorenz**, P. Salama, K. W. Dunn, E. J. Delp, "Digital Correction of Motion Artefacts in Microscopy Image Sequences Collected from Living Animals Using Rigid and Non-Rigid Registration," *Journal of Microscopy*, vol. 245, no. 2, pp. 148-160, February 2012.

- R. G. Presson Jr., M. B. Brown, A. J. Fisher, R. M. Sandoval, K. W. Dunn, **K. S. Lorenz**, E. J. Delp, P. Salama, B. A. Molitoris, I. Petrache, "Two-Photon Imaging within the Murine Thorax without Respiratory and Cardiac Motion Artifact," *The American Journal of Pathology*, vol. 179, no. 1, pp. 75-82, July 2011.

Conference Publications

- **K. S. Lorenz**, P. Salama, K. W. Dunn, E. J. Delp, "A Multi-Resolution Approach to Non-Rigid Registration of Microscopy Images," *Proceedings of the*

[1]National Library of Medicine Insight Segmentation and Registration Toolkit (http://www.itk.org)

IEEE International Symposium on Biomedical Imaging, Barcelona, Spain, 2-5 May 2012.

- **K. S. Lorenz**, P. Salama, K. W. Dunn, E. J. Delp, "Non-rigid registration of multiphoton microscopy images using B-splines," *Proceedings of SPIE Medical Imaging 2011: Image Processing*, Lake Buena Vista, FL, 12-17 February 2011.

- **K. S. Lorenz**, F. Serrano, P. Salama, E. J. Delp, "Segmentation and Registration Based Analysis of Microscopy Images," *Proceedings of the IEEE International Conference on Image Processing*, Cairo, Egypt, 7-11 November 2009.

- **K. S. Lorenz**, F. Serrano, P. Salama, E. J. Delp, "Analysis of Multiphoton Renal and Liver Microscopy Images: Preliminary Approaches to Segmentation and Registration," *Proceedings of the Workshop on Microscopic Image Analysis with Applications in Biology*, Bethesda, MD, 3-4 September 2009.

LIST OF REFERENCES

LIST OF REFERENCES

[1] R. K. P. Benninger, M. Hao, and D. W. Piston, "Multi-photon excitation imaging of dynamic processes in living cells and tissues," *Reviews of Physiology Biochemistry and Pharmacology*, ser. Reviews of Physiology, Biochemistry and Pharmacology. Springer Berlin Heidelberg, 2008, vol. 160, pp. 71–92.

[2] D. W. Piston, "Imaging living cells and tissues by two-photon excitation microscopy," *Trends in Cell Biology*, vol. 9, no. 2, pp. 66–69, 1999.

[3] W. R. Zipfel, R. M. Williams, and W. W. Webb, "Nonlinear magic: multiphoton microscopy in the biosciences," *Nature Biotechnology*, vol. 21, pp. 1369–1377, October 2003.

[4] W. Denk and K. Svoboda, "Photon upmanship: Why multiphoton imaging is more than a gimmick," *Neuron*, vol. 18, no. 3, pp. 351–357, 1997.

[5] P. T. C. So, C. Y. Dong, B. R. Masters, and K. M. Berland, "Two-photon excitation fluorescence microscopy," *Annual Review of Biomedical Engineering*, vol. 2, no. 1, pp. 399–429, 2000.

[6] D. W. Piston, "The coming of age of two-photon excitation imaging for intravital microscopy," *Advanced Drug Delivery Reviews*, vol. 58, no. 7, pp. 770–772, 2006.

[7] A. Dufour, V. Shinin, S. Tajbakhsh, N. Guillen-Aghion, J.-C. Olivo-Marin, and C. Zimmer, "Segmenting and tracking fluorescent cells in dynamic 3-D microscopy with coupled active surfaces," *IEEE Transactions on Image Processing*, vol. 14, no. 9, pp. 1396–1410, September 2005.

[8] M. J. Kyan, L. Guan, M. R. Arnison, and C. J. Cogswell, "Feature extraction of chromosomes from 3-D confocal microscope images," *IEEE Transactions on Biomedical Engineering*, vol. 48, no. 11, pp. 1306–1318, November 2001.

[9] K. W. Dunn, R. M. Sandoval, K. J. Kelly, P. C. Dagher, G. A. Tanner, S. J. Atkinson, R. L. Bacallao, and B. A. Molitoris, "Functional studies of the kidney of living animals using multicolor two-photon microscopy," *American Journal of Physiology - Cell Physiology*, vol. 283, no. 3, pp. C905–C916, 2002.

[10] W. Denk, J. H. Strickler, and W. W. Webb, "Two-photon laser scanning fluorescence microscopy," *Science*, vol. 248, no. 4951, pp. 73–76, 1990.

[11] L. G. Brown, "A survey of image registration techniques," *ACM Computing Surveys*, vol. 24, no. 4, pp. 325–376, 1992.

[12] B. Zitová and J. Flusser, "Image registration methods: A survey," *Image and Vision Computing*, vol. 21, no. 11, pp. 977–1000, October 2003.

[13] L. M. Russo, R. M. Sandoval, M. McKee, T. M. Osicka, A. B. Collins, D. Brown, B. A. Molitoris, and W. D. Comper, "The normal kidney filters nephrotic levels of albumin retrieved by proximal tubule cells: Retrieval is disrupted in nephrotic states," *Kidney International*, vol. 71, no. 6, pp. 504–513, 2007.

[14] J. Peti-Peterdi, I. Toma, A. Sipos, and S. L. Vargas, "Multiphoton Imaging of Renal Regulatory Mechanisms," *Physiology*, vol. 24, no. 2, pp. 88–96, 2009.

[15] F.-C. Li, Y. Liu, G.-T. Huang, L.-L. Chiou, J.-H. Liang, T.-L. Sun, C.-Y. Dong, and H.-S. Lee, "In vivo dynamic metabolic imaging of obstructive cholestasis in mice," *American Journal of Physiology - Gastrointestinal and Liver Physiology*, vol. 296, no. 5, pp. G1091–G1097, May 2009.

[16] T. P. Theruvath, M. C. Snoddy, Z. Zhong, and J. J. Lemasters, "Mitochondrial permeability transition in liver ischemia and reperfusion: Role of c-Jun N-Terminal Kinase 2," *Transplantation*, vol. 85, no. 10, pp. 1500–1504, May 2008.

[17] D. Kreisel, R. G. Nava, W. Li, B. H. Zinselmeyer, B. Wang, J. Lai, R. Pless, A. E. Gelman, A. S. Krupnick, and M. J. Miller, "In vivo two-photon imaging reveals monocyte-dependent neutrophil extravasation during pulmonary inflammation," *Proceedings of the National Academy of Sciences*, vol. 107, no. 42, pp. 18 073–18 078, 2010.

[18] R. L. Bacallao, W. Yu, K. W. Dunn, and C. L. Phillips, "Novel light microscopy imaging techniques in nephrology," *Current Opinion in Nephrology and Hypertension*, vol. 12, no. 1, pp. 455–481, 2003.

[19] K. Svoboda and R. Yasuda, "Principles of two-photon excitation microscopy and its applications to neuroscience," *Neuron*, vol. 50, no. 6, pp. 823–839, 2006.

[20] J. Skoch, G. A. Hickey, S. T. Kajdasz, B. T. Hyman, and B. J. Bacskai, "In vivo imaging of amyloid-beta deposits in mouse brain with multiphoton microscopy," *Amyloid Proteins*, ser. Methods in Molecular Biology, E. M. Sigurdsson and J. M. Walker, Eds. Humana Press, 2005, vol. 299, pp. 349–363.

[21] A. Zarbock and K. Ley, "New insights into leukocyte recruitment by intravital microscopy," *Visualizing Immunity*, ser. Current Topics in Microbiology and Immunology, M. Dustin and D. McGavern, Eds. Springer Berlin Heidelberg, 2009, vol. 334, pp. 129–152.

[22] C. Sumen, T. R. Mempel, I. B. Mazo, and U. H. von Andrian, "Intravital microscopy: Visualizing immunity in context," *Immunity*, vol. 21, no. 3, pp. 315–329, 2004.

[23] M. J. Hickey and P. Kubes, "Intravascular immunity: The host-pathogen encounter in blood vessels," *Nature Reviews - Immunology*, vol. 9, no. 5, pp. 364–375, May 2009.

[24] S. J. Lunt, C. Gray, C. C. Reyes-Aldasoro, S. J. Matcher, and G. M. Tozer, "Application of intravital microscopy in studies of tumor microcirculation," *Journal of Biomedical Optics*, vol. 15, no. 1, 2010.

[25] J. Condeelis and J. E. Segall, "Intravital imaging of cell movement in tumours," *Nature Reviews - Cancer*, vol. 3, pp. 921–930, December 2003.

[26] D. Fukumura, D. G. Duda, L. L. Munn, and R. K. Jain, "Tumor microvasculature and microenvironment: Novel insights through intravital imaging in pre-clinical models," *Microcirculation*, vol. 17, no. 3, pp. 206–225, 2003.

[27] J. W. Irwin and J. MacDonald, "Microscopic observations of the intrahepatic circulation of living guinea pigs," *The Anatomical Record*, vol. 117, no. 1, pp. 1–15, 1953.

[28] M. G. Clemens, P. F. McDonagh, I. H. Chaudry, and A. E. Baue, "Hepatic microcirculatory failure after ischemia and reperfusion: Improvement with ATP-MgCl2 treatment," *American Journal of Physiology - Heart and Circulatory Physiology*, vol. 248, no. 6, pp. H804–H811, 1985.

[29] M. Ghiron, "Ueber eine neue Methode mikroskopischer Untersuchung am lebenden organismus," *Zbl. Physiol.*, vol. 26, pp. 613–617, 1912.

[30] M. Steinhausen and G. A. Tanner, *Microcirculation and Tubular Urine Flow in the Mammalian Kidney Cortex (in vivo Microscopy)*, ser. Lecture Notes in Computer Science. Springer-Verlag, 1976.

[31] P. Sarder and A. Nehorai, "Deconvolution methods for 3-D fluorescence microscopy images," *IEEE Signal Processing Magazine*, vol. 23, no. 3, pp. 32–45, May 2006.

[32] E. Meijering, I. Smal, O. Dzyubachyk, and J. Olivo-Marin, "Time-lapse imaging," *Microscope Image Processing*, Q. Wu, F. Merchant, and K. Castleman, Eds. Burlington, MA: Elsevier Academic Press, 2008, ch. 15, pp. 401–440.

[33] X. Zhou and S. T. C. Wong, "Informatics challenges of high-throughput microscopy," *IEEE Signal Processing Magazine*, vol. 23, no. 3, pp. 63–72, May 2006.

[34] K. Nandy, P. R. Gudla, and S. J. Lockett, "Automatic segmentation of cell nuclei in 2D using dynamic programming," *Proceedings of the Workshop on Microsopic Image Analysis with Applications in Biology*, Piscataway, NJ, 21 September 2007.

[35] G. Srinivasa, M. C. Fickus, Y. Guo, A. D. Linstedt, and J. Kovacevic, "Active mask segmentation of fluorescence microscope images," *IEEE Transactions on Image Processing*, vol. 18, no. 8, pp. 1817–1829, August 2009.

[36] X. Chen, X. Zhou, and S. T. C. Wong, "Automated segmentation, classification, and tracking of cancer cell nuclei in time-lapse microscopy," *IEEE Transactions on Biomedical Engineering*, vol. 53, no. 4, pp. 762–766, April 2006.

[37] X. Zhou, F. Li, J. Yan, and S. T. C. Wong, "A novel cell segmentation method and cell phase identification using markov model," *IEEE Transactions on Information Technology in Biomedicine*, vol. 13, no. 2, pp. 152–157, March 2009.

[38] A. Dima, M. Scholz, and K. Obermayer, "Automatic segmentation and skeletonization of neurons from confocal microscopy images based on the 3-D wavelet transform," *IEEE Transactions on Image Processing*, vol. 11, no. 7, pp. 790–801, July 2002.

[39] S. Mallat and S. Zhong, "Characterization of signals from multiscale edges," *IEEE Transactions on Pattern Analysis and Machine Intelligence*, vol. 14, no. 7, pp. 710–732, July 1992.

[40] B. L. Luck, K. D. Carlson, A. C. Bovik, and R. R. Richards-Kortum, "An image model and segmentation algorithm for reflectance confocal images of in vivo cervical tissue," *IEEE Transactions on Image Processing*, vol. 14, no. 9, pp. 1265–1276, September 2005.

[41] A. Calapez and A. Rosa, "A statistical pixel intensity model for segmentation of confocal laser scanning microscopy images," *IEEE Transactions on Image Processing*, vol. 19, no. 9, pp. 2408–2418, September 2010.

[42] O. Dzyubachyk, W. A. van Cappellen, J. Essers, W. J. Niessen, and E. Meijering, "Advanced level-set-based cell tracking in time-lapse fluorescence microscopy," *IEEE Transactions on Medical Imaging*, vol. 29, no. 3, pp. 852–867, March 2010.

[43] Y. Al-Kofahi, W. Lassoued, W. Lee, and B. Roysam, "Improved automatic detection and segmentation of cell nuclei in histopathology images," *IEEE Transactions on Biomedical Engineering*, vol. 57, no. 4, pp. 841–852, April 2010.

[44] X. Yang, H. Li, and X. Zhou, "Nuclei segmentation using marker-controlled watershed, tracking using mean-shift, and kalman filter in time-lapse microscopy," *IEEE Transactions on Circuits and Systems*, vol. 53, no. 11, pp. 2405–2414, November 2006.

[45] G. Li, T. Liu, A. Tarokh, J. Nie, L. Guo, A. Mara, S. Holley, and S. T. C. Wong, "3D cell nuclei segmentation based on gradient flow tracking," *BMC Cell Biology*, vol. 8, no. 1, p. 40, 2007.

[46] X. Liu, A. F. Setiadi, M. S. Alber, P. P. Lee, and D. Z. Chen, "Identification and classification of cells in multispectral microscopy images of lymph nodes," *Proceedings of SPIE Medical Imaging 2011: Image Processing*, Lake Buena Vista, FL, 12-17 February 2011.

[47] K. Pohl, J. Fisher, J. Levitt, M. Shenton, R. Kikinis, W. Grimson, and W. Wells, "A unifying approach to registration, segmentation, and intensity correction," *Proceedings of the International Conference on Medical Image Computing and Computer Assisted Intervention*, Palm Springs, CA, 26-30 October 2005.

[48] S. Marsland and R. McLachlan, "A hamiltonian particle method for diffeomorphic image registration," *Information Processing in Medical Imaging*, ser. Lecture Notes in Computer Science, N. Karssemeijer and B. Lelieveldt, Eds. Springer Berlin / Heidelberg, 2007, vol. 4584, pp. 396–407.

[49] C. R. Maurer Jr. and J. M. Fitzpatrick, "A review of medical image registration," *Interactive Image-Guided Neurosurgery*, R. J. Maciunas, Ed. Thieme for the American Association of Neurological Surgeons, 1993, pp. 17–44.

[50] J. Y. Chiang and B. J. Sullivan, "Coincident bit counting—A new criterion for image registration," *IEEE Transactions on Medical Imaging*, vol. 12, no. 1, pp. 30–38, Narch 1993.

[51] S. Jonić, C. O. S. Sorzano, P. Thévenaz, C. El-Bez, S. De Carlo, and M. Unser, "Spline-based image-to-volume registration for three-dimensional electron microscopy," *Ultramicroscopy*, vol. 103, no. 4, pp. 303–317, 2005.

[52] A. P. Goobic, J. Tang, and S. T. Acton, "Image stabilization and registration for tracking cells in the microvasculature," *IEEE Transactions on Biomedical Engineering*, vol. 52, no. 2, pp. 287–299, February 2005.

[53] I.-H. Kim, Y.-C. M. Chen, D. L. Spector, R. Eils, and K. Rohr, "Nonrigid registration of 2-D and 3-D dynamic cell nuclei images for improved classification of subcellular particle motion," *IEEE Transactions on Image Processing*, vol. 20, no. 4, pp. 1011–1022, April 2011.

[54] A. Akselrod-Ballin, D. Bock, R. C. Reid, and S. K. Warfield, "Accelerating image registration with the Johnson–Lindenstrauss lemma: Application to imaging 3-D neural ultrastructure with electron microscopy," *IEEE Transactions on Medical Imaging*, vol. 30, no. 7, pp. 1427–1438, July 2011.

[55] D. P. McCullough, P. R. Gudla, B. S. Harris, J. A. Collins, K. J. Meaburn, M.-A. Nakaya, T. P. Yamaguchi, T. Misteli, and S. J. Lockett, "Segmentation of whole cells and cell nuclei from 3-D optical microscope images using dynamic programming," *IEEE Transactions on Medical Imaging*, vol. 27, no. 5, pp. 723–734, May 2008.

[56] A. M. Bazen and S. H. Gerez, "Fingerprint matching by thin-plate spline modelling of elastic deformations," *Pattern Recognition*, vol. 36, no. 8, pp. 1859–1867, 2003.

[57] K. Rohr, H. S. Stiehl, R. Sprengel, T. M. Buzug, W. J., and M. H. Kuhn, "Landmark-based elastic registration using approximating thin-plate splines," *IEEE Transactions on Medical Imaging*, vol. 20, no. 6, pp. 526–534, June 2001.

[58] J. Pánek and J. Vohradský, "Point pattern matching in the analysis of two-dimensional gel electropherograms," *Electrophoresics*, vol. 20, no. 18, pp. 3483–3491, 1999.

[59] T. Akutsu, K. Kanaya, A. Ohyama, and A. Fujiyama, "Point matching under non-uniform distortions," *Discrete Applied Mathematics*, vol. 127, no. 1, pp. 5–21, 2003.

[60] X. Huang, N. Paragios, and D. N. Metaxas, "Shape registration in implicit spaces using information theory and free form deformations," *IEEE Transactions on Pattern Analysis and Machine Intelligence*, vol. 28, no. 8, pp. 1303–1318, August 2006.

[61] S. Ram, J. J. Rodriguez, and G. Bosco, "Size-invariant cell nucleus segmentation in 3-D microscopy," *Proceedings of the IEEE Southwest Symposium on Image Analysis and Interpretation*, Santa Fe, NM, 22-24 April 2012, pp. 37–40.

[62] E. B. van de Kraats, G. P. Penney, D. Tomazevic, T. van Walsum, and W. J. Niessen, "Standardized evaluation methodology for 2-D-3-D registration," *IEEE Transactions on Medical Imaging*, vol. 24, no. 9, pp. 1177–1189, September 2005.

[63] D. Škerl, B. Likar, and F. Pernuš, "A protocol for evaluation of similarity measures for rigid registration," *Medical Imaging, IEEE Transactions on*, vol. 25, no. 6, pp. 779–791, June 2006.

[64] A. Gholipour, N. Kehtarnavaz, R. W. Briggs, K. S. Gopinath, W. Ringe, A. Whittemore, S. Cheshkov, and K. Bakhadirov, "Validation of non-rigid registration between functional and anatomical magnetic resonance brain images," *IEEE Transactions on Biomedical Engineering*, vol. 55, no. 2, pp. 563–571, February 2008.

[65] A. Klein, J. Andersson, B. A. Ardekani, J. Ashburner, B. Avants, M.-C. Chiang, G. E. Christensen, D. L. Collins, J. Gee, P. Hellier, J. H. Song, M. Jenkinson, C. Lepage, D. Rueckert, P. Thompson, T. Vercauteren, R. P. Woods, J. J. Mann, and R. V. Parsey, "Evaluation of 14 nonlinear deformation algorithms applied to human brain MRI registration," *NeuroImage*, vol. 46, no. 3, pp. 786–802, 2009.

[66] J. B. A. Maintz and M. A. Viergever, "A survey of medical image registration," *Medical Image Analysis*, vol. 2, no. 1, pp. 1–36, 1998.

[67] M. M. Kamocka, J. Mu, X. Liu, N. Chen, A. Zollman, B. Sturonas-Brown, K. Dunn, Z. Xu, D. Z. Chen, M. S. Alber, and E. D. Rosen, "Two-photon intravital imaging of thrombus development," *Journal of Biomedical Optics*, vol. 15, no. 1, p. 016020, February 2010.

[68] K. S. Lorenz, F. Serrano, P. Salama, and E. J. Delp, "Segmentation and registration based analysis of microscopy images," *Proceedings of the IEEE International Conference on Image Processing*, Cairo, Egypt, 7-10 November 2009, pp. 4213–4216.

[69] P. Salama, "A least squares approach to estimating the probability distribution of unobserved data in multiphoton microscopy," *Proceedings of the SPIE Conference on Computational Imaging VI*, San Jose, CA, 28-29 January 2008.

[70] J. B. Pawley, *Handbook Of Biological Confocal Microscopy*. Springer, 2006.

[71] J. A. Rosado-Toro and J. J. Rodriguez, "Cell splitting using dynamic programming," *Proceedings of the IEEE Southwest Symposium on Image Analysis and Interpretation*, Santa Fe, NM, 22-24 April 2012, pp. 33–36.

[72] C. L. Phillips, L. J. Arend, A. J. Filson, D. J. Kojetin, J. L. Clendenon, S. Fang, and K. W. Dunn, "Three-dimensional imaging of embryonic mouse kidney by two-photon microscopy," *The American Journal of Pathology*, vol. 158, no. 1, pp. 49–55, 2001.

[73] T. W. Ridler and S. Calvard, "Picture thresholding using an iterative selection method," *IEEE Transactions on Systems, Man, and Cybernetics*, vol. 8, no. 8, pp. 630–632, August 1978.

[74] R. M. Haralick, S. R. Sternberg, and X. Zhuang, "Image analysis using mathematical morphology," *IEEE Transactions on Pattern Analysis and Machine Intelligence*, vol. 9, no. 4, pp. 532–550, July 1987.

[75] C. Wählby, I.-M. Sintorn, F. Erlandsson, G. Borgefors, and E. Bergtsson, "Combining intensity, edge and shape information for 2D and 3D segmentation of cell nuclei in tissue sections," *Journal of Microscopy*, vol. 215, no. 1, pp. 67–76, July 2004.

[76] N. Otsu, "A threshold selection method from gray-level histograms," *IEEE Transactions on Systems, Man, and Cybernetics*, vol. 9, no. 1, pp. 62–66, January 1979.

[77] M. Sezgin and B. Sankur, "Survey over image thresholding techniques and quantitative performance evaluation," *Journal of Electronic Imaging*, vol. 13, no. 1, pp. 146–168, January 2004.

[78] J. V. Hajnal, D. L. G. Hill, and D. J. Hawkes, *Medical Image Registration*. CRC Press, Boca Raton, FL, 2001.

[79] W. Lu, M.-L. Chen, G. H. Olivera, K. J. Ruchala, and T. R. Mackie, "Fast free-form deformable registration via calculus of variations," *Physics in Medicine and Biology*, vol. 49, no. 14, pp. 3067–3087, 2004.

[80] S. Yang, D. Köhler, K. Teller, T. Cremer, P. Le Baccon, E. Heard, R. Eils, and K. Rohr, "Nonrigid registration of 3-D multichannel microscopy images of cell nuclei," *IEEE Transactions on Image Processing*, vol. 17, no. 4, pp. 493–499, April 2008.

[81] P. Thévenaz, U. E. Ruttimann, and M. Unser, "A pyramid approach to subpixel registration based on intensity," *IEEE Transactions on Image Processing*, vol. 7, no. 1, pp. 27–41, January 1998.

[82] A. Gholipour, N. Kehtarnavaz, R. Briggs, M. Devous, and K. Gopinath, "Brain functional localization: A survey of image registration techniques," *IEEE Transactions on Medical Imaging*, vol. 26, no. 4, pp. 427–451, April 2007.

[83] S. K. Balci, P. Goll, M. Shenton, and W. M. Wells, "Free-form b-spline deformation model for groupwise registration," *Proceedings of the International Conference on Medical Image Computing and Computer-Assisted Intervention*, Brisbane, Australia, 29 October - 2 November 2007, pp. 23–30.

[84] M. Holden, "A review of geometric transformations for nonrigid body registration," *IEEE Transactions on Medical Imaging*, vol. 27, no. 1, pp. 111–128, January 2008.

[85] L. Ibáñez, W. Schroeder, L. Ng, and J. Cates, *The ITK Software Guide*. Kitware, Inc., 2005.

[86] L. Ibáñez, L. Ng, J. Gee, and S. Aylward, "Registration patterns: The generic framework for image registration of the Insight Toolkit," *Proceedings of the IEEE International Symposium on Biomedical Imaging*, Washington, DC, 7-10 June 2002, pp. 345–348.

[87] M. Arnold, S. J. Fink, D. Grove, M. Hind, and P. F. Sweeney, "A survey of adaptive optimization in virtual machines," *Proceedings of the IEEE*, vol. 93, no. 2, pp. 449–466, February 2005.

[88] J. R. Swisher, P. D. Hyden, S. H. Jacobson, and L. W. Schruben, "A survey of simulation optimization techniques and procedures," *Proceedings of the Winter Simulation Conference*, Orlando, FL, 10-13 December 2000, pp. 119–128.

[89] G. P. Penney, J. Weese, J. A. Little, P. Desmedt, D. L. G. Hill, and D. J. Hawkes, "A comparison of similarity measures for use in 2-D-3-D medical image registration," *IEEE Transactions on Medical Imaging*, vol. 17, no. 4, pp. 586–595, August 1998.

[90] I. Kim, S. Yang, P. Le Baccon, E. Heard, Y.-C. Chen, D. Spector, C. Kappel, R. Eils, and K. Rohr, "Non-rigid temporal registration of 2D and 3D multi-channel microscopy image sequences of human cells," *Proceedings of the IEEE International Symposium on Biomedical Imaging: From Nano to Macro*, Washington, DC, 12-15 April 2007, pp. 1328–1331.

[91] J. P. W. Pluim, J. B. A. Maintz, and M. A. Viergever, "Mutual-information-based registration of medical images: A survey," *IEEE Transactions on Medical Imaging*, vol. 22, no. 8, pp. 986–1004, August 2003.

[92] T. M. Cover and J. A. Thomas, *Elements of Information Theory*, 2nd ed. Wiley-Interscience, Hoboken, NJ, July 2006.

[93] D. Mattes, D. R. Haynor, H. Vesselle, T. K. Lewellen, and W. Eubank, "Non-rigid multimodality image registration," *Proceedings of SPIE Medical Imaging 2001: Image Processing*, San Diego, CA, 17-22 February 2001, pp. 1609–1620.

[94] P. Thévenaz, U. E. Ruttimann, and M. Unser, "Iterative multi-scale registration without landmarks," *Proceedings of the IEEE International Conference on Image Processing*, vol. 3, Washington, DC, 23-26 October 1995, pp. 228–231.

[95] C. O. S. Sorzano, P. Thévenaz, and M. Unser, "Elastic registration of biological images using vector-spline regularization," *IEEE Transactions on Biomedical Engineering*, vol. 52, no. 4, pp. 652–663, April 2005.

[96] J.-P. Thirion, "Non-rigid matching using demons," *Proceedings of the IEEE Conference on Computer Vision and Pattern Recognition*, San Francisco, CA, 18-20 June 1996, pp. 245–251.

[97] ——, "Image matching as a diffusion process: An analogy with Maxwell's demons," *Medical Image Analysis*, vol. 2, no. 3, pp. 243–260, 1998.

[98] H. Wang, L. Dong, J. O'Daniel, R. Mohan, A. S. Garden, K. K. Ang, D. A. Kuban, M. Bonnen, J. Y. Chang, and R. Cheung, "Validation of an accelerated 'demons' algorithm for deformable image registration in radiation therapy," *Physics in Medicine and Biology*, vol. 50, pp. 2887–2905, 2005.

[99] X. Pennec, P. Cachier, and N. Ayache, "Understanding the "Demon's Algorithm": 3D non-rigid registration by gradient descent," *Proceedings of the International Conference on Medical Image Computing and Computer-Assisted Intervention*, Cambridge, UK, 19-22 September 1999, pp. 597–605.

[100] J.-K. Shen, B. J. Matuszewski, L.-K. Shark, A. Skalski, T. Zielinski, and C. J. Moore, "Deformable image registration - A critical evaluation: Demons, b-spline FFD and spring mass system," *Proceedings of the International Conference on BioMedical Visualization*, London, UK, 9-11 July 2008, pp. 77–82.

[101] P. Thévenaz, T. Blu, and M. Unser, "Interpolation revisited," *IEEE Transactions on Medical Imaging*, vol. 19, no. 7, pp. 739–758, July 2000.

[102] M. Unser, "Splines: A perfect fit for signal and image processing," *IEEE Signal Processing Magazine*, vol. 16, no. 6, pp. 22–38, November 1999.

[103] D. Rueckert, L. I. Sonoda, C. Hayes, D. L. G. Hill, M. O. Leach, and D. J. Hawkes, "Nonrigid registration using free-form deformations: Application to breast MR images," *IEEE Transactions on Medical Imaging*, vol. 18, no. 8, pp. 712–721, August 1999.

[104] Y. Mazaheri, L. Bokacheva, D.-J. Kroon, O. Akin, H. Hricak, D. Chamudot, S. Fine, and J. A. Koutcher, "Semi-automatic deformable registration of prostate MR images to pathological slices," *Journal of Magnetic Resonance Imaging*, vol. 32, no. 5, pp. 1149–1157, April 2010.

[105] S. Lee, G. Wolberg, and S. Y. Shin, "Scattered data interpolation with multilevel b-splines," *IEEE Transactions on Visualization and Computer Graphics*, vol. 3, no. 3, pp. 228–244, July-September 1997.

[106] T. Rohlfing, C. R. Maurer Jr., D. A. Bluemke, and M. A. Jacobs, "Volume-preserving nonrigid registration of MR breast images using free-form deformation with an incompressibility constraint," *IEEE Transactions on Medical Imaging*, vol. 22, no. 6, pp. 730–741, June 2003.

[107] D. Rueckert, L. I. Sonoda, E. Denton, S. Rankin, C. Hayes, M. O. Leach, D. Hill, and D. J. Hawkes, "Comparison and evaluation of rigid and non-rigid registration of breast MR images," *Proceedings of SPIE Medical Imaging: Image Processing*, San Diego, CA, 22 February 1999.

[108] J. Kybic and M. Unser, "Fast parametric elastic image registration," *IEEE Transactions on Image Processing*, vol. 12, no. 11, pp. 1427–1442, November 2003.

[109] P. Cachier, E. Bardinet, D. Dormont, X. Pennec, and N. Ayache, "Iconic feature based nonrigid registration: The PASHA algorithm," *Computer Vision and Image Understanding*, vol. 89, no. 23, pp. 272–298, 2003.

[110] K. S. Lorenz, P. Salama, K. W. Dunn, and E. J. Delp, "A multi-resolution approach to non-rigid registration of microscopy images," *Proceedings of the IEEE International Symposium on Biomedical Imaging*, Barcelona, Spain, 2-5 May 2011.

[111] V. Caselles, F. Catté, T. Coll, and F. Dibos, "A geometric model for active contours in image processing," *Numerische Mathematik*, vol. 66, pp. 1–31, 1993.

[112] M. Kass, A. Witkin, and D. Terzopoulos, "Snakes: Active contour models," *International Journal of Computer Vision*, vol. 1, pp. 321–331, 1988.

[113] V. Caselles, R. Kimmel, and G. Sapiro, "Geodesic active contours," *International Journal of Computer Vision*, vol. 22, pp. 61–79, 1997.

[114] T. F. Chan and L. A. Vese, "Active contours without edges," *IEEE Transactions on Image Processing*, vol. 10, no. 2, pp. 266–277, February 2001.

[115] Y. Zhang, B. J. Matuszewski, L.-K. Shark, and C. J. Moore, "Medical image segmentation using new hybrid level-set method," *Proceedings of the International Conference on BioMedical Visualization*, London, UK, 9-11 July 2008, pp. 71–76.

[116] T. F. Chan, B. Y. Sandberg, and L. A. Vese, "Active contours without edges for vector-valued images," *Journal of Visual Communication and Image Representation*, vol. 11, no. 2, pp. 130–141, 2000.

[117] A. du Chéné, C. Min, and F. Gibou, "Second-order accurate computation of curvatures in a level set framework using novel high-order reinitialization schemes," *Journal of Scientific Computing*, vol. 35, pp. 114–131, 2008.

[118] B. Li and S. T. Acton, "Active contour external force using vector field convolution for image segmentation," *IEEE Transactions on Image Processing*, vol. 16, no. 8, pp. 2096–2106, August 2007.

[119] ——, "Automatic active model initialization via poisson inverse gradient," *IEEE Transactions on Image Processing*, vol. 17, no. 8, pp. 1406–1420, August 2008.

[120] C. Xu and J. L. Prince, "Generalized gradient vector flow external forces for active contours," *Signal Processing*, vol. 71, no. 2, pp. 131–139, 1998.

[121] A. Yezzi Jr., A. Tsai, and A. Willsky, "A fully global approach to image segmentation via coupled curve evolution equations," *Journal of Visual Communication and Image Representation*, vol. 13, no. 12, pp. 195–216, 2002.

[122] S. Lankton, D. Nain, A. Yezzi, and A. R. Tannenbaum, "Hybrid geodesic region-based curve evolutions for image segmentation," *Proceedings of SPIE Medical Imaging 2007: Physics of Medical Imaging*, San Diego, CA, 17-22 February 2007.

[123] S. Lankton and A. Tannenbaum, "Localizing region-based active contours," *IEEE Transactions on Image Processing*, vol. 17, no. 11, pp. 2029–2039, November 2008.

[124] L. A. Vese and T. F. Chan, "A multiphase level set framework for image segmentation using the Mumford and Shah model," *International Journal of Computer Vision*, vol. 50, pp. 271–293, 2002.

[125] K. S. Lorenz, P. Salama, K. W. Dunn, and E. J. Delp, "Digital correction of motion artefacts in microscopy image sequences collected from living animals using rigid and nonrigid registration," *Journal of Microscopy*, vol. 245, no. 2, pp. 148–160, February 2012.

[126] J. L. Clendenon, C. L. Phillips, R. M. Sandoval, S. Fang, and K. W. Dunn, "Voxx: a PC-based, near real-time volume rendering system for biological microscopy," *American Journal of Physiology-Cell Physiology*, vol. 282, no. 1, pp. C213–C218, 2002.

[127] M. Urschler, S. Kluckner, and H. Bischof, "A framework for comparison and evaluation of nonlinear intra-subject image registration algorithms," *The Insight Journal*, October 2007.

[128] J. Ashburner, "A fast diffeomorphic image registration algorithm," *NeuroImage*, vol. 38, no. 1, pp. 95–113, 2007.

[129] J. A. Schnabel, C. Tanner, A. D. Castellano-Smith, A. Degenhard, M. O. Leach, D. R. Hose, D. L. G. Hill, and D. J. Hawkes, "Validation of nonrigid image registration using finite-element methods: pplication to breast MR images," *IEEE Transactions on Medical Imaging*, vol. 22, no. 2, pp. 238–247, February 2003.

[130] D. Rueckert and P. Aljabar, "Nonrigid registration of medical images: Theory, methods, and applications," *IEEE Signal Processing Magazine*, vol. 27, no. 4, pp. 113–119, July 2010.

[131] K. S. Lorenz, P. Salama, K. W. Dunn, and E. J. Delp, "Non-rigid registration of multiphoton microscopy images using b-splines," *Proceedings of SPIE Medical Imaging 2011: Image Processing*, Lake Buena Vista, FL, 12-17 February 2011.

[132] J. Jain and A. Jain, "Displacement measurement and its application in interframe image coding," *IEEE Transactions on Communications*, vol. 29, no. 12, pp. 1799–1808, December 1981.

[133] F. Maes, A. Collignon, D. Vandermeulen, G. Marchal, and P. Suetens, "Multimodality image registration by maximization of mutual information," *IEEE Transactions on Medical Imaging*, vol. 16, no. 2, pp. 187–198, April 1997.

[134] P. Viola and W. M. Wells, "Alignment by maximization of mutual information," *Proceedings of the International Conference on Computer Vision*, Cambridge, MA, 20-23 June 1995, pp. 16–23.

[135] A. Collignon, F. Maes, D. Delaere, D. Vandermeulen, P. Suetens, and G. Marchal, "Automated multi-modality image registration based on information theory," *Proceedings of the International Conference on Information Processing in Medical Imaging*, Ile de Berder, France, 26-30 June 1995, pp. 263–274.

[136] K. S. Lorenz, F. Serrano, P. Salama, and E. J. Delp, "Analysis of multiphoton renal and liver microscopy images: Preliminary approaches to segmentation and registration," *Proceedings of the Workshop on Microsopic Image Analysis with Applications in Biology*, Bethesda, MD, 3-4 September 2009.

[137] J. M. Fitzpatrick, J. B. West, and C. R. Maurer Jr., "Predicting error in rigid-body point-based registration," *IEEE Transactions on Medical Imaging*, vol. 17, no. 5, pp. 694–702, October 1998.

[138] R. G. Presson Jr., M. B. Brown, A. J. Fisher, R. M. Sandoval, K. W. Dunn, K. S. Lorenz, E. J. Delp, P. Salama, B. A. Molitoris, and I. Petrache, "Two-photon imaging within the murine thorax without respiratory and cardiac motion artifact," *The American Journal of Pathology*, vol. 179, no. 1, pp. 75–82, 2011.

[139] J. Wu, M. Kim, J. Peters, H. Chung, and S. Samant, "Evaluation of similarity measures for use in the intensity-based rigid 2D-3D registration for patient positioning in radiotherapy," *Medical Physics*, vol. 36, no. 12, p. 5391, 2009.

[140] The MathWorks, Inc., "Morphological Reconstruction, Image Processing Toolbox."

APPENDIX

A. INITIAL SEGMENTATION APPROACH BASED ON MORPHOLOGICAL MULTI-SCALE ANALYSIS

In this appendix, we describe an earlier method we developed for segmentation of multiphoton microscopy images. This approach was abandoned in favor of the method described in Chapter 2. This initial approach discussed here only addresses image segmentation as motion artifacts were not addressed. Therefore, the results would not reflect the true motion of just the internal biological structures. However, the proposed method in Chapter 2 considers both image segmentation and registration.

A.1 Maximum a Posteriori Filtering

The first step in this method is identical to the first step in our proposed segmentation method as described in Section 2.1. This is a Bayesian denoising filter to reduce noise and enhance edge detail.

A.2 Morphological Filtering and Segmentation

With respect to image segmentation, the initial approach was to consider a grayscale morphological multi-scale analysis [74], as shown in Figure A.1. Original data images are provided as the input to the system, shown at the bottom of the figure as x_i, indicating a single image within the data set. Each operator F_k represents a morphological opening followed by a morphological reconstruction, both using the same structuring element. Morphological reconstruction is a series of repeated dilations of an image, known as the marker image, until the profile of the marker image is entirely less than the profile of a second image, known as the mask image. This process causes the peaks in the marker image to dilate [140]. The marker image is given as the mor-

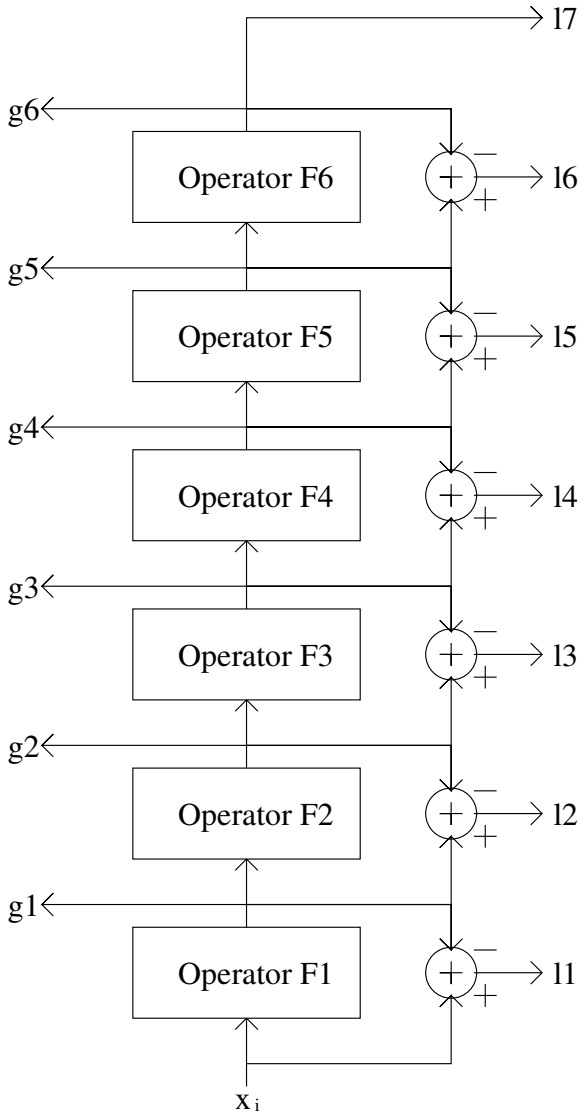

Fig. A.1.: Block diagram of morphological multi-scale analysis

phologically opened image, while the mask image is given as the original input image. Each operator F_k uses a flat, square structuring element of size $2k+1 \times 2k+1$. Due to the multi-scale structure, subsequent images, l_k, extract increasingly larger objects from the previous g_{k-1} images. The g_k images contain the remaining objects after objects segmented in l_k have been removed.

In selecting which filter outputs should appear in the final output, the analysis was subjective (leading to this approach later being abandoned). Compositions such as

$l_4+l_5+l_6+g_6$ and g_4 appeared to produce acceptable results. However, the segmented objects in these composition images often contained small holes. To eliminate these holes, a single morphological closing operation with a flat, square structuring element of size 5×5 was used. The size of this structuring element was selected empirically. The resulting image now contained large, undesired dark artifacts. Only the cells with the greatest intensity are desired. Therefore, a binary image was created by using a simple thresholding technique, where the threshold was chosen subjectively to eliminate the dark artifacts and retain the desired cellular objects. From this binary image, the final output image was created. For black pixels in the binary image, the corresponding pixels in the output image remain black. For white pixels in the binary image, the corresponding pixels in the output image are restored to the corresponding pixels in the original image. Denoting an original image by O, its corresponding mask by B, then the segmented image F is given by:

$$F(m,n) = B(m,n)O(m,n) \tag{A.1}$$

just as was performed in the last step of our proposed segmentation method as described in Section 2.7.

It should be noted that this approach is both a causal and memoryless system. The current output image only depends on the current input image. No dependencies on previous or future images are created. However, a drawback with this approach became apparent due to the nature of the data sets being analyzed. In the majority of the images, individual cells are composed of individual pixels that are not very contiguous. Images of the cells do not appear as solid objects and often contain many black pixels interspersed between white pixels. This is due to characteristics of the image acquisition system. For extreme cases, the morphological opening operations eliminated all of these cells, and the corresponding images turned out to be essentially completely black, particularly for beginning and ending images in the sequence.

A.3 Experimental Results

We demonstrate our morphological multi-scale analysis using the same two data sets of multiphoton fluorescent microscopy images we initially introduced to demonstrate our proposed approach in Section 6.1. For these two data sets, one consists of nuclei from kidney tissue and the second consists of vasculature from the kidney of a living rat. The decompositions of example images from each of the two data sets are shown in Figure A.2 and Figure A.3 respectively. Example images displaying the final segmentation results for both of these two data sets are shown in Figure A.4.

Despite satisfactory segmentation results and sufficient performance for many image sets, results using this approach from other image sets were poor. This is because the output of this approach—a static composition of several multi-scale layers chosen empirically—was inconsistent as image intensity varied with tissue depth. Tissue is not homogeneous, and traditional segmentation techniques have given poor results. Therefore, due to the lack of ability to dynamically adapt the output according to image intensity, this approach was abandoned in favor of the approach described in Chapter 2.

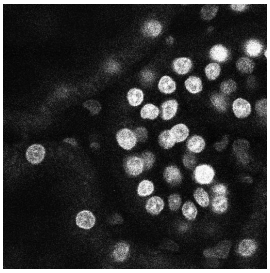

(a) Original image

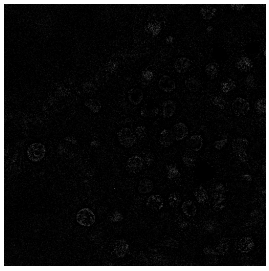

(b) Image $l1$

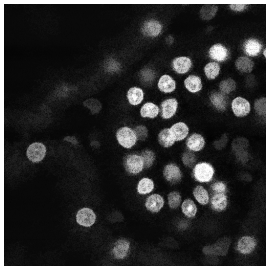

(c) Image $g1$

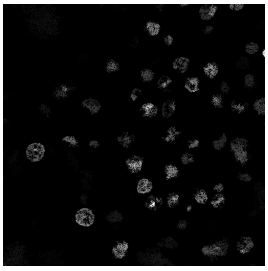

(d) Image $l2$

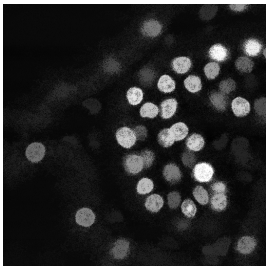

(e) Image $g2$

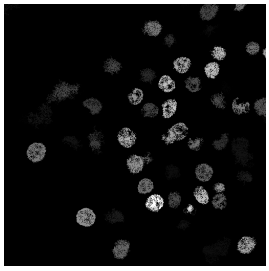

(f) Image $l3$

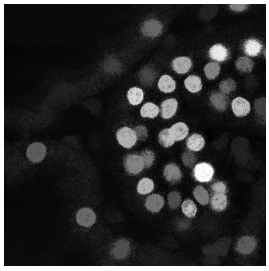

(g) Image $g3$

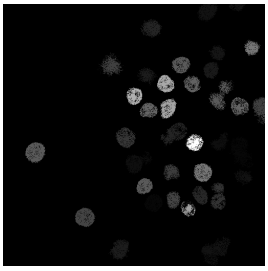

(h) Image $l4$

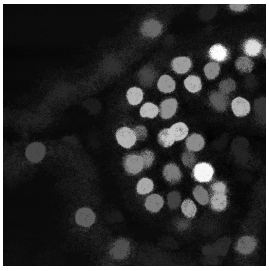

(i) Image $g4$

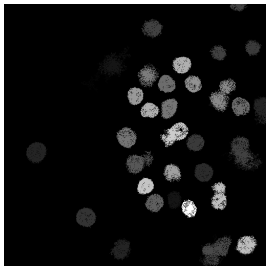

(j) Image $l5$

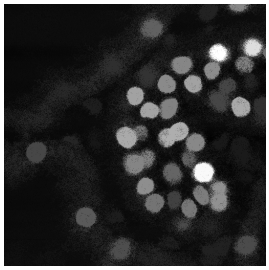

(k) Image $g5$

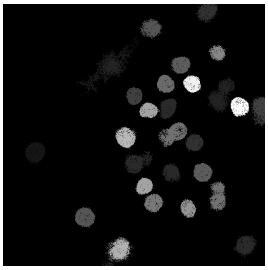

(l) Image $l6$

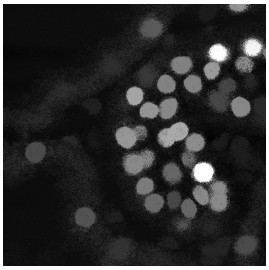

(m) Image $g6$

Fig. A.2.: Multi-scale decomposition of example image from rat kidney nuclei

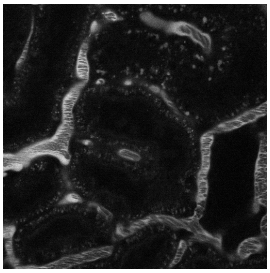

(a) Original image

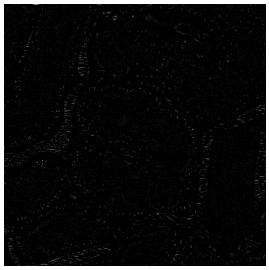

(b) Image $l1$

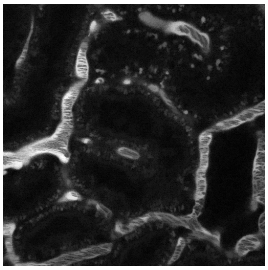

(c) Image $g1$

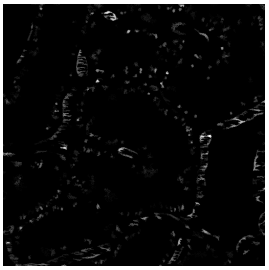

(d) Image $l2$

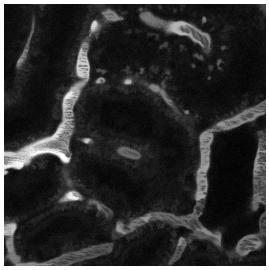

(e) Image $g2$

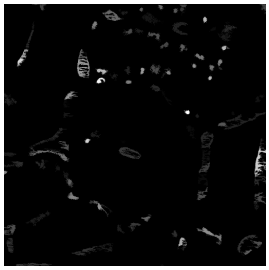

(f) Image $l3$

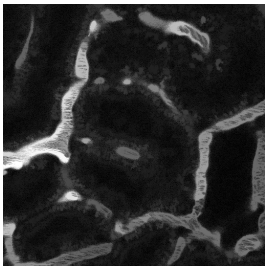

(g) Image $g3$

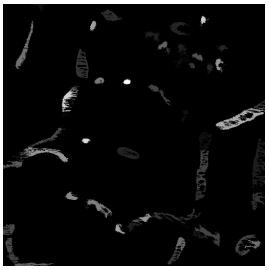

(h) Image $l4$

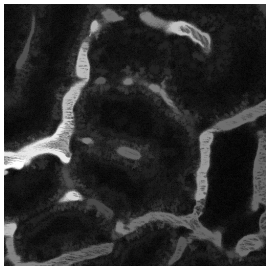

(i) Image $g4$

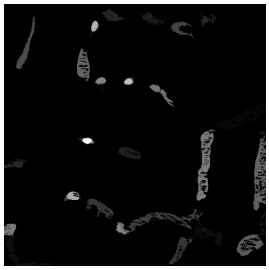

(j) Image $l5$

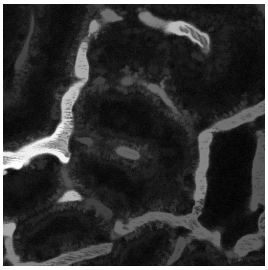

(k) Image $g5$

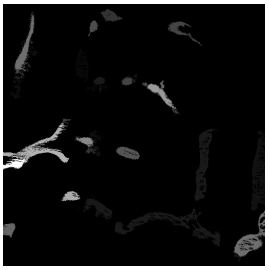

(l) Image $l6$

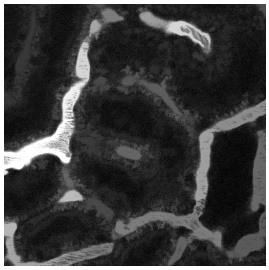

(m) Image $g6$

Fig. A.3.: Multi-scale decomposition of example image from rat kidney vasculature

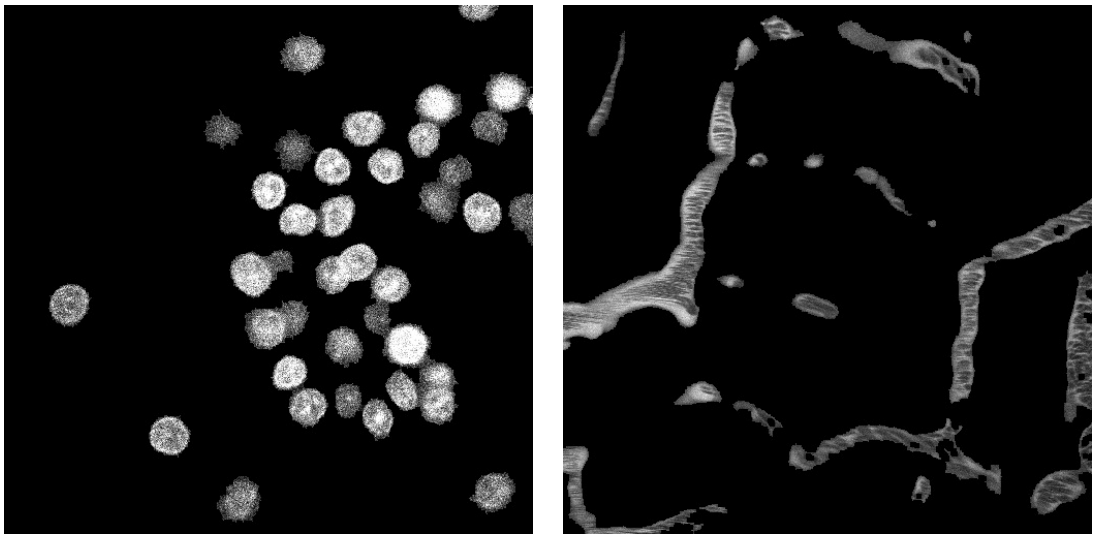

(a) Rat kidney nuclei data set (b) Rat kidney vasculature data set

Fig. A.4.: Multi-scale decomposition segmentation results

VITA

VITA

Kevin Lorenz received his Bachelor of Science degrees in Electrical Engineering and Computer Engineering from Michigan State University, East Lansing, Michigan in 2007. He received his Master of Science in Electrical and Computer Engineering degree from Purdue University, West Lafayette, Indiana in 2009.

Kevin joined the Ph.D. program at Purdue University, West Lafayette, Indiana in 2007. Since 2008, he has served as a Research Assistant in the Video and Image Processing Laboratory (VIPER). His major adviser, Professor Edward J. Delp, is the Charles William Harrison Distinguished Professor of Electrical and Computer Engineering and Professor of Biomedical Engineering. While under his supervision in the graduate program, Kevin has worked on projects sponsored by grants from the National Institutes of Health.

Kevin's current research interests include image and video processing, image analysis, image segmentation, and image registration.